UNIVERSIDADE FEDERAL DO PARANÁ

ABD. RASHID BIN MOHD YUSOFF

# MAGNETIC FIELD EFFECT IN ORGANIC SEMICONDUCTING MATERIALS AND DEVICES

CURITIBA

2011

**ABD. RASHID BIN MOHD YUSOFF**

# MAGNETIC FIELD EFFECT IN ORGANIC SEMICONDUCTING MATERIALS AND DEVICES

Tese apresentada ao Curso de Pós-Graduação em Física do Setor de Ciências Exatas da Universidade Federal do Paraná, como requisito parcial para a obtenção do grau de Doutor em Ciências.

Orientador:
Prof. Dr. Ivo Alexandre Hümmelgen

CURITIBA

2011

# ABSTRACT

The present work consists of the fabrication and characterization of hybrid organic/inorganic permeable base transistors using sulfonated polyaniline as a base terminal. Four different emitters were used in this work: $Alq_3$, $Alq_3/C_{60}$, $C_{60}/Alq_3$, and $C_{60}/Alq_3/C_{60}$. It was observed a strong influence of base/emitter heterostructure on the electrical and magnetic characteristics on the transistor. Two different charge injection layers were used in this work: Ca and $V_2O_5$. The studied transistors present electrons as majority charge carriers. The electrical characterization was performed through two and three terminal measurements. The three terminal measurements consist in its two distinct operation modes: common-base and common-emitter. Additionally, magnetic characterization of the transistors were sequentially made for two times (a) without applied external magnetic field (0 mT); and (b) with applied external magnetic field (100 mT). Images of the surface of sulfonated polyaniline films over silicon were made by atomic force microscope and optical microscopy in order to verify the base morphology. The influences of the base thickness and opening voids on the transistors electrical and magnetic characteristics were studied.

Keywords: hybrid transistor, permeable base transistor, organic emitter, sulfonated polyaniline

# RESUMO

O presente trabalho consiste transistores híbridos orgânicos/inorgânicos transistores de base permeável usando polianilina sulfonada como um terminal de base. Quatro emissores diferentes foram utilizados neste trabalho: $Alq_3$, $Alq_3/C_{60}$, $C_{60}/Alq_3$ e $C_{60}/Alq_3/C_{60}$. Foi observada uma forte influência de heteroestruturas da base/emissor sobre as características elétricas e magnéticas do transistor. Duas camadas de injecção diferentes foram utilizadas neste trabalho: Ca e $V_2O_5$. Os transistores estudados apresentam elétrons como portadores de carga majoritário. A caracterização elétrica foi realizada através medidas de dois e três terminais. A medida de três terminais consiste em dois modos de operação distintos: base comum e emissor comum. Além disso, as características dos transistores magnéticos foram medidas sequencialmente sob duas condições: (a) sem campo magnético externo aplicado (0 mT), e (b) com campo magnético externo aplicado (100 mT). Imagnes da superfície de filmes de polianilina sulfonada sobre silício foram feitas por microscopia de força atômica e microscopia óptica, a fim de verificar a morfologia da base. As influências da espessura da base e de vazios sobre as características de transistores elétricos e magnéticos foram estudadas.

Palavras-chave: transistor híbrido, transistor de base permeável, emissor orgânico, polianilina sulfonada

# Resumo Estendido em Português

O presente trabalho consiste na fabricação e caracterização de transistores híbridos orgânico/inorgânico de base permeável, usando polianilina sulfonada como termina de base. Os objetivos principais do presente estudo são a determinação da origem dos efeitos de campo magnético em materiais semicondutores e dispositivos orgânicos e também determinar se há necessidade de haver portadores de carga positivos e negativos, ou somente de um tipo.

Nesta tese, iniciamos com as propriedades básicas de semicondutores orgânicos e teoria de transistores. No segundo capítulo, desenvolvemos as propriedades básicas de semicondutores orgânicos tais como semicondutores n e p, materiais conjugados e estrutura eletrônica de semicondutores orgânicos. A parte seguinte nesse capítulo é a teoria fundamental de transistores de base permeável onde discutimos sobre configurações base comum, emissor comum, e coletor comum juntamente com as características de diodo Schottky. Fechando o capítulo, colocamos uma breve discussão sobre efeitos de campo magnético em materiais semicondutores orgânicos e alguns modelos propostos, que são bipôlaron, éxciton, interação éxciton-pôlaron e também o último modelo proposto, de acoplamento éxciton-pôlaron.

O capítulo 3 é basicamente devotado a detalhes experimentais. Iniciamos o capítulo com uma explicação detalhada da preparação de amostras iniciada com o processo de limpeza do substrato de silício e seguida do procedimento de síntese da polianilina

sulfonada. O produto final é então caracterizado fisicamente e quimicamente. Para a caracterização física são usadas microscopia de força atômica e microscopia ótica, para estudar a topografia superficial de nossa polianilina sulfonada. Dessa caracterização, encontramos a existência de orifícios na superfície da polianilina sulfonada. Entretanto, os orifícios diminuem a medida que aumentamos a espessura da polianilina sulfonada. Uma discussão detalhada da relação de orifícios ganho no modo base comum e emissor comum é apresentada no capítulo 4. Para a caracterização química, empregamos Espectroscopia por Transformada Rápida de Fourier (FTIR), Espectroscopia MicroRaman, Espectroscopia Ultravioleta-Visível-Infravermelho próximo (UV-Vis) e também análise termogravimétrica (TGA). Para a caracterização por FTIR, Raman e TGA, foi usada polianilina sulfonada depositada sobre silício enquanto que para medidas UV-Vis foi utilizado substrato de vidro e todos os espectros foram obtidos a temperatura ambiente. Dos dados obtidos, os picos em 617 e 1024 confirmara que a polianilina foi dopada com grupo ácido sulfônico. Do espectro FTIR pudemos estimar o grau de sulfonação como de aproximadamente 27 %. No espectro Raman pudemos observar três regiões distintas atribuídas à polianilina sulfonada. Estes três intervalos vão de (i) 1100 – 1210 $cm^{-1}$, (ii) 1216 – 1221 $cm^{-1}$, and (iii) 1504 – 1514 $cm^{-1}$. A primeira região corresponde à torção no plano de anéis benzênicos ou quinona, a segunda região corresponde ao alongamento de grupos C-N, C=N e C~N, e a última corresponde ao alongamento de anéis benzeno ou quinona. Nesse sentido, o espectro UV-Vis revelou que existem três picos importantes localizados em 320, 440, e 850 nm referentes à polianilina sulfonada. O pico em 320 nm é devido à transição $\pi$-$\pi^*$ do anel da anilina, o segundo pico em 440 nm foi atribuído ao cátion radical localizado e o último pico largo a 850 nm corresponde ao pôlaron metálico. De medidas de TGA, concluímos que a estabilidade

térmica da polianilina sulfonada é devida à presença de grupos ácido sulfônico no polímero derivado de anilina.

O capítulo 4 é basicamente voltado à caracterização magnética e elétrica. Todas as medidas foram realizadas a temperatura ambiente no escuro, sob duas condições: (i) sem e (ii) com campo magnético. Propusemos e desenvolvemos quatro dispositivos distintos com diferentes materiais e espessuras de emissor. Para a caracterização elétrica, medidas a dois e três terminais foram investigadas sob diferentes condições, quais sejam: sem a presença de campo magnético (0 mT) e na presença de campo magnético (100 mT). Quatro diferentes emissores foram usados neste trabalho: (i) $Alq_3$, (ii) $Alq_3/C_{60}$, (iii) $C_{60}/Alq_3$, e (iv) $C_{60}/Alq_3/C_{60}$. Foi observada uma forte influência da heteroestrutura base/emissor sobre as características elétricas e magnéticas do transistor. Duas diferentes camadas injetoras foram usadas neste trabalho: Ca e $V_2O_5$. Os transistores estudados apresentaram elétrons como portadores majoritários. As medidas a três terminais consistem de dois distintos modos de operação: base comum e emissor comum. Das medidas a dois terminais, os resultados obtidos revelaram que o transporte de elétrons do emissor para o coletor é significativamente mais fácil se comparado ao transporte do emissor para a base. Isto geralmente sugere a existência de barreira na junção emissor-base e canais condutores conectando o emissor e o coletor que permitam contornar a existência da base, o que suporta a existência de orifícios como os observados em medidas de microscopia ótica. Também determinamos a altura da barreira Schottky usando método corrente-voltagem sob duas condições diferentes: (i) sem tratamento térmico, e (ii) com tratamento térmico. No caso sem tratamento térmico, a barreira Schottky cresce com o aumento da espessura da polianilina sulfonada. Entretanto, introduzindo o tratamento térmico da camada de

polianilina sulfonada a barreira Schottky decresce à medida que aumenta a temperatura. No primeiro dispositivo, que apresenta $Alq_3$ como emissor, efeitos de campo magnético não podem ser observados nas medidas no modo base comum. Mas nas medidas no modo emissor comum, há uma influência significativa do campo magnético sobre o dispositivo. A corrente de coletor cresce abruptamente ao se introduzir o campo magnético. Outra maneira de se observar o efeito do campo magnético é pelo ganho em modo emissor comum. O ganho em modo emissor comum sob influência do campo magnético atingiu o valor 8 a tensão de coletor de 2 V e corrente de base de aproximadamente 0.86 μA. Um ganho em modo emissor comum ruim de aproximadamente 2 pode ser observado no dispositivo sem a presença de campo magnético. Resultados obtidos a partir de medidas a dois terminais e emissor comum nos levam a concluir que a presença de alterações do campo magnético afetam a mobilidade dos portadores de carga e isto está de acordo com o modelo de interação polaron-exciton. Este modelo sugere que a corrente no dispositivo e a mobilidade do portador de carga devem ser aumentados devido à presença do campo magnético. Seguindo estas argumentações, o aumento de corrente neste dispositivo é devido às mudanças na mobilidade do portador de carga e, ao mesmo tempo, mudanças na concentração de portadores de carga.

No segundo dispositivo (com emissor $Alq_3/C_{60}$), também não há efeito de campo magnético observável de medidas no modo base-comum. Mas no modo emissor comum podem ser observadas pequenas mudanças na corrente de coletor quando se aplica o campo magnético. O ganho em modo emissor comum calculado sem a aplicação de campo magnético foi em torno de 37 a tensão de coletor de 3 V e corrente de base de 0.86 μA. Entretanto, um incremento significativo ocorreu no mesmo dispositivo quando foi

introduzido o campo magnético e o ganho de corrente atingiu 50 a tensão de coletor de 2.85 V e corrente de base 0.86 μA. Da caracterização elétrica, magnética e de morfologia superficial, encontramos que com o aumento da espessura da base, ocorre a redução dos orifício da base resultando o decréscimo do ganho em modo base comum. Adicionalmente, o aumento da espessura de base resulta em incremento no ganho em modo emissor comum. Sob influência do campo magnético, o ganho em modo emissor comum atingiu valor máximo com base de espessura de 153 nm. Mas ganho em modo emissor comum decresceu com o aumento da espessura da base, mesmo na presença de campo magnético.

No terceiro dispositivo com camada emissora $C_{60}/Alq_3$, ocorre também uma mudança na corrente de coletor quando se introduz o campo magnético. O ganho em modo emissor comum extraído é adicionalmente incrementado em 200 % com a presença do campo magnético a tensão de coletor de 5 V e corrente de base de 0.86 μA. Neste terceiro dispositivo, também não foi possível observar qualquer influência do campo magnético sobre o ganho de corrente no modo base-comum.

No dispositivo de camada emissora tripla($C_{60}/Alq_3/C_{60}$), novamente não há efeito de campo magnético observável no ganho em modo base-comum mas ao introduzir o campo magnético, o ganho em modo emissor comum apresentou alterações que correspondem a um incremento de 10 para 23 a tensão de emissor de 5 V e corrente de base de 0.86 μA.

Da caracterização elétrica (modo emissor comum) concluímos que o transporte eletrônico do emissor é significativamente influenciado pelo campo magnético. Isto pode sugerir que a eficiência de injeção de elétrons do terminal emissor é aumentada na presença

do campo magnético. Em todos os dispositivos deste estudo, não pôde ser observada influência do campo magnético sobre as características em modo base-comum.

Para confirmar que dois portadores são importantes em efeitos de campo magnético, foram desenvolvidos dispositivos somente-elétron e somente-buraco verdadeiros. A discussão relativa a estes dois dispositivos é apresentada na última parte da tese (apêndice). Em dispositivos somente-elétron verdadeiros, a injeção de elétrons da camada de Ca ocorre no nível LUMO do $Alq_3$, enquanto que em dispositivos somente buraco buracos são injetados no nivel HOMO do $Alq_3$ a partir da camada de Au. Destes dispositivos de portador único concluímos que nenhum efeito de campo magnético pode ser observado, pois todas as curves obtidas se sobrepõe, sem qualquer indicação clara de efeito do campo magnético.

# Acknowledgement

When you start thanking people, you are always in danger of forgetting someone. For safety reason, I would like to say that I am very grateful and fortunate to everybody who helped and supported me in any way during the research that I will describe in this short acknowledgement, during projects that did not make it to this thesis and during my daily life as "estrangeiros". A special thank goes to :-

- **TWAS-CNPq**: For sponsoring my Doctor of Science study in Universidade Federal do Paraná, Brasil.

- **Prof. Ivo A. Hümmelgen**: A wonderful thanks must go to a wonderful person, mentor, banker, and also advisor. He has been a terrific human. From the day he fetched me up at the Curitiba Alfonso Pena Airport (it was already midnight because the TAM flight from Sao Paulo was delayed) till the day I shook his hands after my thesis defends. I have strongly benefited from his creative ideas, his support, and his guidance. Above all, Ivo's energy, enthusiasm, and positivity are awe-inspiring. Even on his busiest days, I have never seen Ivo turn away his group member needing answers, advice, or a sounding board. I will remember his frequent quote "Just a moment please". I'm not sure how he has remained interested, alert, and intelligent in the midst of so many commitments especially when we were about to move to a new building, but Ivo has been a tremendous role model for me.

- **Prof. Dra. Michelle Meruvia**: Many thanks to her who opened the doors to the lab for me without hesitation when I approached her during my earliest days. In addition to helping me keep a foot in the world of organic transistor, Michelle has always been willing to help me out with research feedback, laboratory assistant, and career advice and especially for my device fabrication.

- **Prof. Dr. Jose Freire and Prof. Dr. Marlus Koehler**: Thank you so much to come across to my side of room for agreeing to be a referee for my recommendation letter, to discuss my Solid State Physics exercises, and to provide me with excellent feedback.

- **Dr. Wilson Jose da Silva**: I owe a huge thank you to him, with whom I have been working very closely for the past years. I really appreciate his dedication and work ethic; without his push, "our collaboration" on SPAN would never have been so fruitful. I thank Wilson not only for the knowledge and deep thinking that he has brought to our discussions, but also for his patience, which must have been tired

while working side by side with me for hours until the end and giving me SPAN whenever I asked.

- **Wagner**: Thanks also go to him who is among the smartest people I have ever met. Wagner is a wonderful experimentalist and never complained about spending hours helping me setting up electrical experiments, writing LabView programming, repairing glove box, and taking me to the Mercado Municipal.

- **Fareed**: Thanks also for him, who joined the group two years with an explosion of energy. Thanks for accompanying me to go to Mercadorama for "shopping" ever Friday.

- **Patrick, Keli, Lucielli, Caser, Marcia, Marcelo, Natasha, Luciana, and Christiano.**

- **Prof. Dr. Aldo Zarbin, Grazie, and his groupmates**: Thanks for allowing me to do FTIR, Micro-Raman, and TGA. In particular, thanks to Grazie for very patiently teaching me to use the FTIR, Micro Raman, and TGA, as well as for being a tireless wealth of information on "peaks".

- **Prof. Regina M. Q. Mello**: Muito obrigado! Many thanks must also go to Regina who always remains calm when it comes to SPAN.

- Good luck to the people who are just starting as I am about to leave: **Bruno, and Christiane**.

- Thanks also to a cheerful chemist **Massai** and a Mexican guy **Jose** for a wonderful chatting.

- Thanks to the secretary, **Tania**, from Departamento de Fisica, for all their help with the administrative work.

- Not to forget, thanks to the coordinator of post-graduate **Prof. Dr. Wilson Junior**.

- "**My parents and also to my in laws**": They have been so supportive from afar. They have all done their best to figure out the appropriate times to celebrate or to sympathize with me as I have struggled through a world so foreign to them.

- **SHARIFAH NURILYANA BINTI SYED FESAL**: Thank you so much to my wife, my partner, and my true love. For the past four years, I have had the joy and privilege to share all of my successes and all of my fears with this wonderful woman, and without her support, nothing would have ever been possible.

# List of Tables

# List of Abbreviations

| Name | Acronym |
|---|---|
| Aluminum tris(8-hydroxyquinoline) | $Alq_3$ |
| Calcium | Ca |
| Vanadium pentoxide | $V_2O_5$ |
| Poly(methyl methacrylate) | PMMA |
| Indium-Gallium | In-Ga |
| Electron volts | eV |
| Organic magnetoresistance | OMAR |
| Organic magnetocurrent | OMAC |
| Magnetic field effect | MFE |
| Nonmagnetic bipolar transistors | NMBTs |
| Nonmagnetic field effect transistors | NMFETs |
| Nonmagnetic organic light emitting diodes | NOLED |
| Nonmagnetic organic solar cells | NOSCs |
| Sulfonated polyaniline | SPAN |
| Permeable-base-transistor | PBT |
| Buckminsterfullerene | $C_{60}$ |
| Organic semiconductors | OSCs |
| Poly(3-hexylthiophene) | P3HT |
| Highest occupied state (molecular orbital) | HOMO |
| Lowest unoccupied state (molecular orbital) | LUMO |
| Emitter | E |
| Base | B |
| Collector | C |
| Common-base | CB |
| Common-emitter | CE |
| Common-collector | CC |
| Ammonium peroxodisulfate | $(NH_4)_2S_2O_8$ |
| Aniline | $C_6H_7N$ |
| Metanilic acid | $C_6H_7NO_3S$ |
| Hydrofluoric acid | HF |
| Fourier transforms infrared | FTIR |
| Ultraviolet visible near infrared | UV-VIS-NIR |
| Thermogravimetric analysis | TGA |
| Atomic force microscopy | AFM |
| Attenuated total reflection | ATR |
| Root mean square | RMS |
| Static induction transistors | SITs |
| Direct current | DC |

# List of Figures

# CONTENTS

# CHAPTER 1
# Introduction

## 1.1 Magnetic-Field-Effect a Reality ?

The effect of magnetic field has been studied in many organic devices since the magnetic field can influence the concentrations of singlet and triplet and also the interactions with free or trapped charge carriers. Avakian et al. studied the effects of magnetic field on the hyperfine interactions which allow interconversion between singlet and triplet [1,2]. The study on magnetic field was further developed by Ern and Merrifield [3] who conducted the study of the role of magnetic effect on the interaction between triplets and paramagnetic centers in anthracene. As reported in their article, the presence of magnetic field would suppress the quenching of triplet exciton and it can be seen with the increment of triplet lifetime. Recently in 2003, a Polish scientific group leaded by Kalinowski et. al [4] performed a study of magnetic field on aluminum tris(8-hydroxyquinoline)-($Alq_3$)-based devices. They found that with the presence of moderate magnetic fields (~ 500 mT), the electroluminescence quantum efficiency increased by ~ 3 %. This increment is accompanied by the changes in the current through the device by almost 2.5 %. The enhancement of electroluminescence quantum efficiency was attributed to the hyperfine mixing of singlet and triplet states while the change in the current was attributed to increment of electron injection in the device. Mermer et. al [5,6] extended the work on the current through organic devices and they introduced the term organic magnetoresistance (OMAR). Since then, an enormous scientific research work has been done, articles have been published, patents have been filed, and a number of novel pure nonmagnetic microelectronic devices have come into the picture. However, the real mechanisms behind these effects are still missing with uncertainties and hotly debated. In relation with this discovery, the two most attractive and promising fields have attracted a significant attention from the scientific communities around the globe. There are namely; (i) molecular electronics, and (ii) magnetic field effect

(MFE). Molecular electronics is determined at substituting our long established semiconductors by organic materials namely; polymer [7], organic single crystal [8] or even single molecule [9], which will make a nice and wonderful paved the way to cheap, easy, low-weight, mechanically flexible, chemically interactive, and bottom-up fabricated electronics. Magnetic field manipulates electronic spins as the information carriers while consumes less power than manipulating electronic charge [10]. MFE basically adds new functionality and economy to available electronic devices by not only applying the electron's charge, but also taking various advantages of the electron's spin and spin degrees of freedom [11]. Given that the spin-dependent transport properties are directly connected to electronic device applications, MFE on nonmagnetic electronic devices with organic semiconducting materials have been seriously explored, studied, investigated and analyzed [5,6,12-33].

To date, several kinds of MFE devices have been proposed and designed such as nonmagnetic molecules sandwiched between two nonmagnetic electrodes; nonmagnetic bipolar transistors (NMBTs) [12], nonmagnetic field effect transistors (NMFETs) [13-15], nonmagnetic organic light emitting diodes (NOLED) [16-32], and nonmagnetic organic solar cells (NOSCs) [33] with the introduction of external magnetic field in-plane with the current flow in the device. Nevertheless, before we can take another step further, especially into any industrial application of magnetically tunable device and novel technologies, we are actually still facing a mountain of challenges in designing, measuring, controlling, and discussing MFE, deep understanding of the influence of magnetic field towards any nonmagnetic devices and interfaces; in particular at metal/semiconductor interfaces. The capability to control this MFE value either positive or negative will permit vast panoply of new possibilities particularly in the area of computing: higher speed storage, lower power

consumption devices, instant start computing, reconfigurable logic, and potentially quantum computation. However until this thesis was written, the MFE effects on molecular devices were unclear, unexplained and seemed to be influenced by many unwanted contributions. To make things more complex, many reported articles on working devices demonstrated a wide spread of performances for similar device architecture but stressing their concern about reproducibility issue. This unidentified issue needs a clear and comprehensive study to find the relation between the spin behavior and processing. Thus, one possible key to solve this issue is to control the interface properties. The realization of these issues still requires significant advancement in our understanding. Solving all these issues requires not only money, time, and patience but it also a development of new experimental tools in order to widen and strengthen our theoretical understanding of MFE. At the end of the tunnel, there will always be a shed of light. Finally, if we are able to accomplish all these issues, the payoff and the benefits will be awesome.

## 1.2 Outline

The scope of this thesis is to improve the understanding of the mechanisms that are responsible for MFE. In order to achieve this ultimate goal, an experimental characterization of MFE in nonmagnetic sulfonated polyaniline (SPAN)-based hybrid vertical permeable-base-transistor (PBT) will be presented. Finally, methods will be demonstrated which can be used to actively control the size of the MFE in a given device structure.

In order to give a systematic presentation, this thesis is organized in the following manner:

• Chapter 2 contains an overview of relevant basics on specific organic semiconductors and introduces the device structure and the working principle of organic transistor. In this chapter the influence of a magnetic field on electron injection in organic transistor devices will be addressed. Previous experimental and theoretical studies of magnetic field in general and of the MFE in particular will be briefly reviewed.

• Chapter 3 starts with synthesis and experimental characterization (physical and chemistry) of used core material – SPAN. Results from physical and chemical properties under different chemical deposition conditions will be presented.

• Chapter 4 starts with an experimental description of the organic transistor fabrication process and discussion about the measurement techniques that were used to

characterize all devices in this thesis. In this chapter, we discuss the experimental results for four different heterostructures namely; (i) SPAN/$Alq_3$; (ii) SPAN/$Alq_3$/$C_{60}$; (iii) SPAN/$C_{60}$/$Alq_3$; and (iv) SPAN/$C_{60}$/$Alq_3$/$C_{60}$. It will be demonstrated that the electron transport and injection in all devices can be influenced by the magnetic field. Using different base electrode thickness, it will furthermore be shown that the common-emitter current gain and common-base current gain can also be affected by external magnetic field. Based on these results an optimal thickness for obtaining large MFE value and high common-emitter current gain value will be suggested.

• Finally, the thesis concludes with a summary of the obtained results and provides an outlook regarding issues that need further investigations in the future.

# CHAPTER 2
# Theoretical background

## 2.1 Basic properties of organic semiconductors

Most electronics devices are fabricated from materials known as semiconductors. This section covers brief fundamentals of conduction in semiconductors. We will discuss about n- and p-type semiconductors.

### 2.1.1 n-type semiconductor

The n-type semiconductor can be produced simply by adding a donor impurity such as arsenic, antimony, or phosphorus to an intrinsic semiconductor. Each donor atom has five valence electrons. When a donor atom replaces an atom in the crystal lattice, only four valence electrons are shared with the surrounding atoms. As displayed in Figure 1, the fifth valence electron (unshared electron) becomes a free electron. The number of free electrons donated by the donor atoms is much greater than the number of free electrons and holes in the intrinsic semiconductor. As a result, the conductivity of the n-type semiconductor is higher that of the intrinsic semiconductor. Because the number of free electrons is greater than the number of holes, the free electrons are the majority carriers. It is called n-type semiconductor because the majority carriers have a negative charge. Hole-electron pairs are continually formed by thermal agitation of the lattice in an n-type semiconductor. Because of the large number of donor electrons, there are many more free electrons available for recombination with the holes. This will decrease the mean lifetime for the holes which decreases the number of holes in the n-type semiconductor compared to the intrinsic semiconductor. For this reason, the current due to the flow of holes in an n-type semiconductor is often neglected in calculations. It is important to understand that a donor atom is electrically neutral if its fifth valence electron does not become a free electron in the lattice. If the fifth electron becomes a free electron, the number of protons in the atom is

greater than the number of electrons by one. In this case, the donor atom becomes a bound positively charged ion.

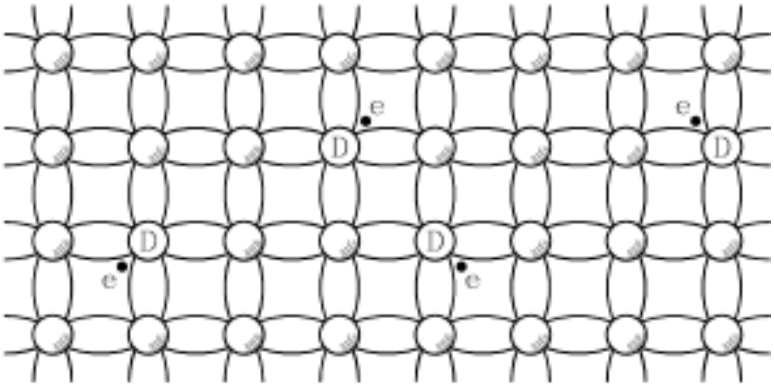


Figure 2.1 2-D illustration of an n-type semiconductor [34]

### 2.1.2 p-type semiconductor

A p-type semiconductor is produced by adding an acceptor impurity such as aluminum, gallium, or boron to an intrinsic semiconductor. Each acceptor atom has three valence electrons. When an acceptor atom replaces an atom in the crystal lattice, there are only three valence electrons shared with the surrounding atoms. This leaves a hole as illustrated in Figure 2. The number of holes created by the acceptor atoms is much greater than the number of free electrons and holes in the intrinsic semiconductor. This makes the conductivity of the p-type semiconductor higher that of the intrinsic semiconductor. Because the number of holes is far greater than the number of electrons, the holes are the majority carriers. The semiconductor is called p-type because the majority carriers have a positive charge. Hole-electron pairs are continually formed by thermal agitation of the lattice in a p-type semiconductor. Because of the large number of holes, there are many more holes available for recombination with the free electrons. This decreases the mean lifetime for the

free electrons which decreases the number of electrons in the p-type semiconductor compared to the intrinsic semiconductor. For this reason, the current due to the flow of free electrons in a p-type semiconductor is often neglected in calculations. It is important to understand that an acceptor atom is electrically neutral if the hole created by the absence of its fourth valence electron is not filled by an electron from an adjacent silicon atom. Once an electron fills the hole, the number of electrons in that atom is greater than the number of protons by one. In this case, the acceptor atom becomes a bound negatively charged ion.

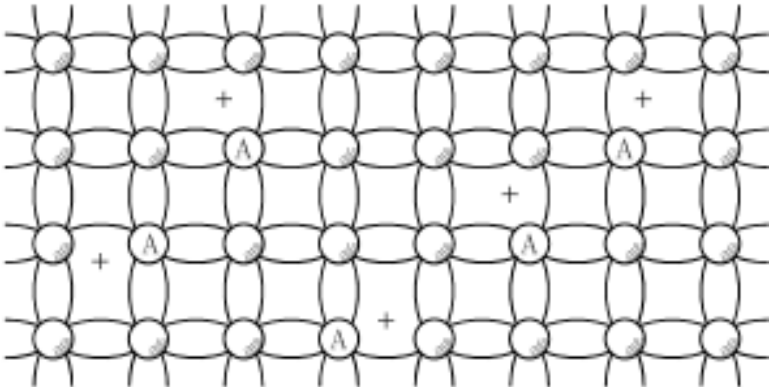

Figure 2.2 2-D illustration of a p-type semiconductor [34]

### 2.1.3 Conjugated Materials

Today, conjugated materials are the most important class of organic semiconductors [35] and can be categorized into two main groups [36] of conjugated polymers and small molecular weight molecules. Polymers, such as polythiophenes consist of many identical units bonded together in a long chain, and are macromolecular in nature, whereas oligomers like oligothiophenes consist of only a few units. In these materials, carbon $p_z$ orbitals overlap and the π-electrons become delocalized on the molecule, forming the so-called π-conjugated system [35,37]. The alternating single and double bonds in polymer drawings

represent these π-electrons. There are other classes of π-conjugated organic semiconductors, OSCs, such as pentacene, fullerenes and etc. which have demonstrated good semiconducting properties. Figure 2.3 shows some important organic semiconductors.

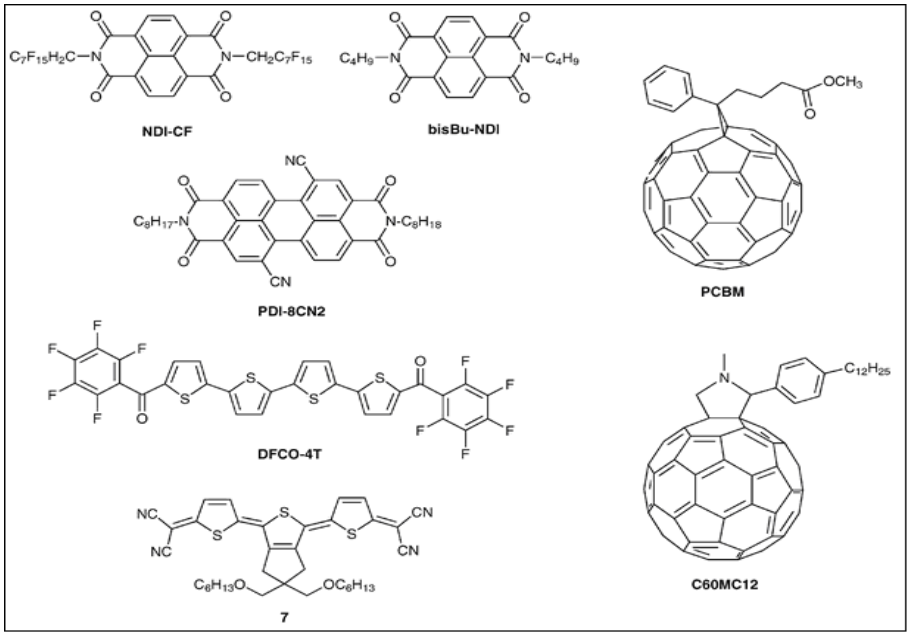


Figure 2.3 Some important organic semiconductors [38]

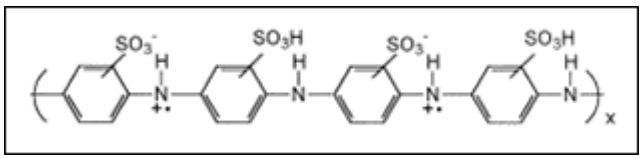

Figure 2.4 Chemical structure of SPAN [39]

An important conjugated polymer, which has been our material of choice for all the experiments and analysis presented in this thesis, is sulfonated polyaniline, SPAN. Figure 2.4 shows a sketch of this molecule.

A variety of techniques have been employed to deposit organic semiconductors onto the active area of the device. One approach is to vacuum-deposit the molecule by thermal evaporation onto the substrate. Pentacene is a prime example of a small-molecule OSCs which has confirmed high mobility and poly or mono-crystalline structure upon proper deposition conditions [37]. Another scheme to deposit OSCs is by processing from solution using printing, spin-coating or drop-casting. Poly(3-hexylthiophene), P3HT is an example of a polymer that can be dissolved in a solvent such as chloroform and be deposited onto a pre-patterned array of electrodes. After the solvent is allowed to evaporate, a film of the polymer is left behind in the active area of the device. The films that are especially drop-cast from solution have been shown [40] to form microcrystalline lamellar structures of 2-D conjugated layers allowing for effective charge transport parallel to the plane leading to high mobilities. One of the most efficient techniques that have been used through out this thesis is chemical deposition.

### 2.1.4 Electronic structure of organic semiconductors

As in traditional inorganic semiconductors, the band gap between the highest occupied state (molecular orbital), HOMO, and the lowest unoccupied state (molecular orbital), LUMO, is relatively small, typically between 1 to 4 eV [37]. Therefore, thermal excitation of electrons from HOMO to LUMO states is possible. However, due to weak Van der Waals forces between OSCs molecules, the self-organization and band formation in these materials are poor. The existence of narrow bands and high degree of electron-phonon interaction and presence of disorder cause charges within the material to become confined in localized polaronic states shrouded by regions of molecular distortion [40].

## 2.2 Fundamentals of hybrid vertical permeable base transistor

The bipolar transistor is a semiconductor device with two p-n junctions intended to amplify and generate electric signals. The terms bipolar transistor reflects the fact that the device depends for its operation on both type of charge carrier, electrons and holes. Structurally, the bipolar transistor is based on a silicon or germanium wafer with three regions of different types of conduction. The two extreme regions are always of the same type of conduction and the medium region is of the opposite type of conduction. The n-type regions separated by a thin p-type layer form an npn transistor structure (Figure 2.5a), and the p-type regions with an n-type layer sandwiched in between form a pnp transistor (Figure 2.5b).

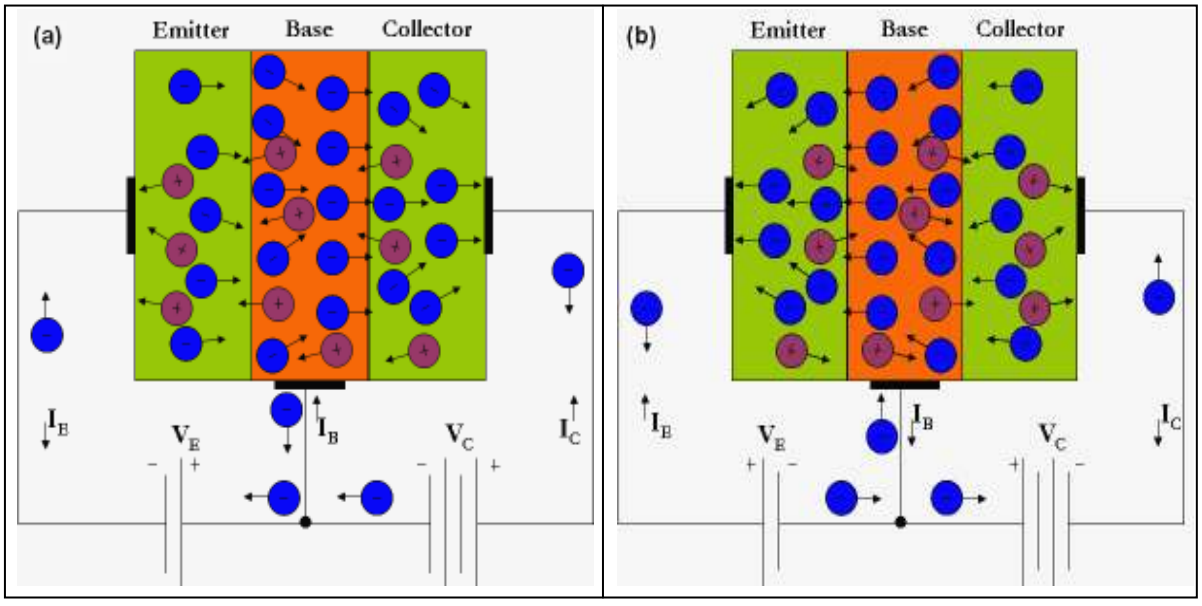


Figure 2.5 (a) npn bipolar transistor in forward biased (b) pnp bipolar transistor in forward biased [41]

The physical process occurring in pnp and npn transistors are analogous, except that the polarities of the bias voltages for those two types are opposite and, hence, the charge carriers are also of the opposite polarities, namely, the majority carriers in the npn transistor are electrons and those in the pnp transistor are holes. The regions separated from each other by p-n junctions are known as the emitter *E*, base *B*, and collector *C*. The emitter emits electrons in the npn transistor and holes in the pnp transistor. The collector collects charge carriers. The base between the emitter and collector acts as a control grid of an electron tube.

In the operating conditions of the transistor, the $V_{EB}$ applied to the left p-n junctions biases this junction in the forward direction and the $V_{BC}$ applied to the right p-n junctions' biases, the latter junction in the reverse direction (See Figure 2.6).

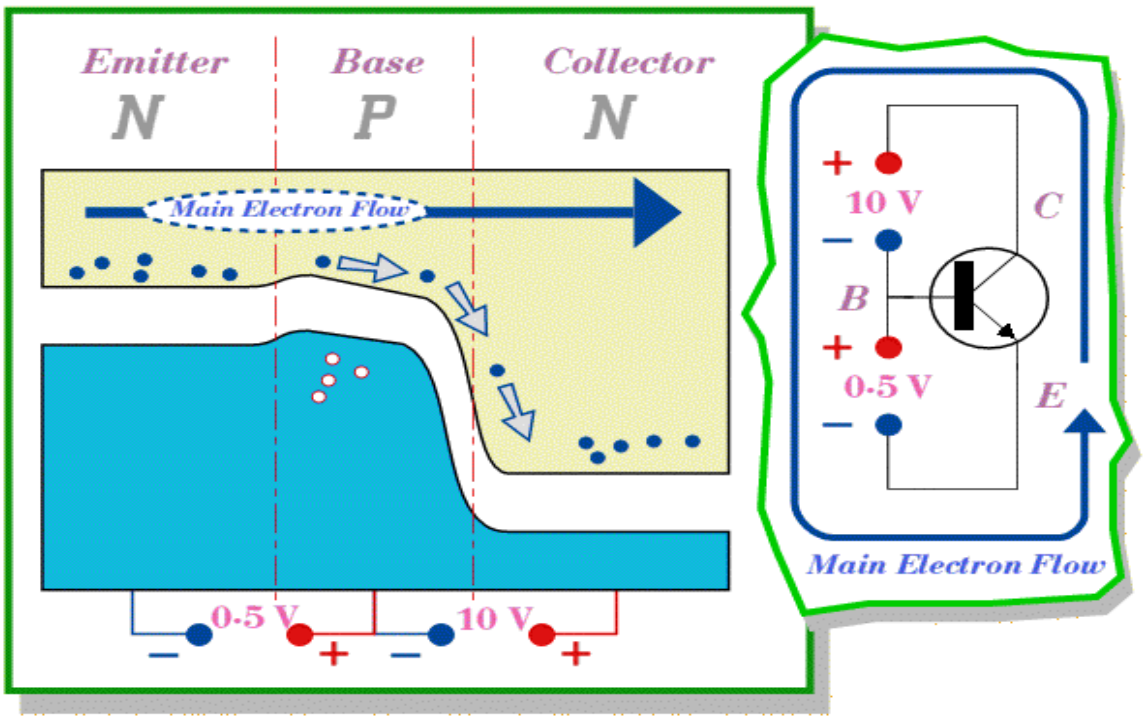


Figure 2.6 Forward-biased emitter-base junction [42]

The electric field causes most of the carriers to flow from the emitter across the p-n junctions into the base, which is a narrow region. A major portion of carriers continue to move toward the second junction, and as they approach it, the electrons get into the electric field produced by an external voltage source, $V_{EC}$. This field sweeps the carriers into the collector, thus increasing the current in the circuit of the voltage source, $V_{EC}$. With an increase in $V_{EB}$, more carriers diffuse from the emitter into the base, i.e. the $I_E$ increases by $\delta I_{EB}$, and so does the $I_C$ by $\delta I_{BC}$.

A small number of charge carriers diffused into the base from the emitter recombine there with the carriers of the opposite charge, but the external circuit supplies new carriers that establish the $I_B$ and compensate for the loss. The $I_C = I_E - I_B$ thus proves insignificantly lower than the $I_E$. The ratio $\alpha = \delta I_C / \delta I_E$ at the constant $V_{CB}$, is known as the current gain, which commonly ranges from 0.990 to 0.995. Strictly speaking, this is the static common-base forward transfer ratio, often designated $h_{FB}$.

If the EB circuit is open and the $I_E$ is zero, while the voltage impressed across the collector and base is $V_{CB}$, the collector circuit will carry a weak reverse (thermal) current, $I_{Cr}$ due to minority carriers. The current heavily depends on temperature and determines the performance of the transistor – the lower this current, the better the parameters of the transistor.

The forward-biased BE junction has low impedance, while reverse-biased CB junction has high impedance. Therefore, the voltage impressed on the emitter is rather low,

tenths of a volt, whereas the voltage applied to the collector can be rather high, up to tens of volts. A change in the $I_E$ caused by a low voltage $V_C$, brings about approximately the same change of current in the collector circuit where the $V_C$ is appreciable. As a result, the transistor provides a power gain between the input and output. When the transistor acts as an amplifier of electric signals, the source of the input ac voltage, $V_I$, i.e. the ac signal subject to amplification, is placed in series with the dc bias source, $V_B$ between the emitter and base, and the output voltage, $V_O$, i.e. the amplified signal, is taken off the load resistance, $R_l$.

Since the transistor is a three-terminal device, it is possible to connect the npn transistor in three configurations, as shown in Figure 2.7. These are the common-base (CB), common-emitter (CE), and common-collector (CC) configurations. The name of the circuit connection reveals which of the terminals is common to both input and output circuits. The transistors connected in various circuit configurations differ in characteristics, but the principle of signal amplification remains the same.

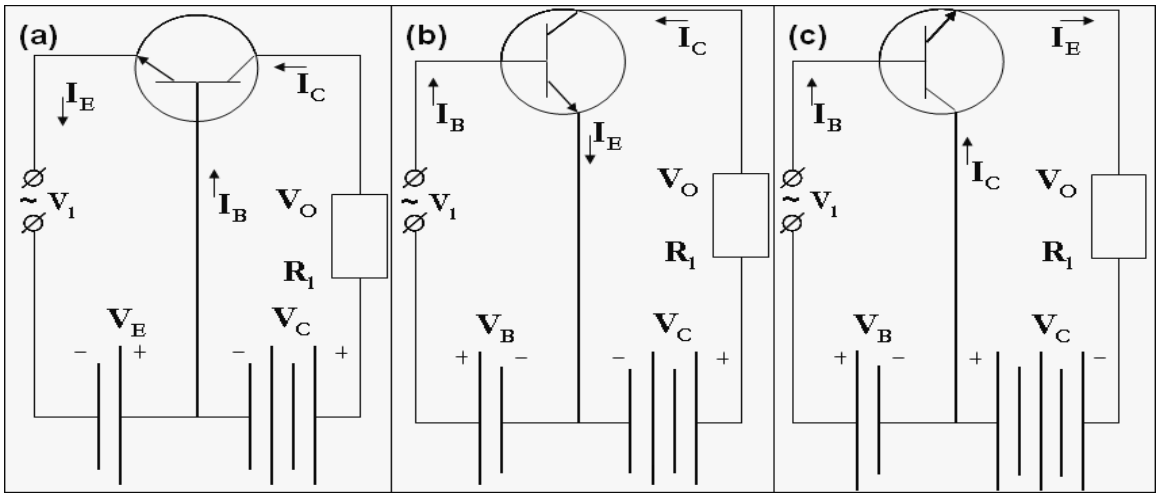


Figure 2.7 Three main npn bipolar transistor configuration; (a) common-base; (b) common-emitter and (c) common-collector characteristics [41]

### 2.2.1 Common-base configuration

In the CB configuration, the incremental change in the input voltage, $\delta V_I$, increases the $I_E$ with the result that both, $I_C$ and output $\delta V_O$ grow, in which case $\delta V_O$ is much higher than $\delta V_I$. In the CB transistor, the input voltage source connects to the BE circuit, while the load and the supply source to the CB circuit. The input resistance of the CB configuration is low, a few ohms or tens of ohms, because the BE junction is under forward bias. But the output resistance is high, hundreds of ohms, because the CB junction is held at reverse bias. A small input resistance of the transistor in CB configuration is a substantial disadvantage, which limits its uses in amplifiers. All of the $I_E$ passes through the input circuit and the transistor does not amplify the current ($a$<1). But the voltage gain and power gain can range into the few hundreds.

### 2.2.2 Common-emitter configuration

In the CE configuration, the input is the BE circuit and the output is the CE circuit with the $R_l$ and supply source. The emitter is thus common to both input and output circuits. The input resistance of the CE circuit is higher than that of the CB circuit because the input current here is the $I_{B,}$ which is much lower than the $I_E$ and $I_C$. The resistance reaches hundreds of ohms. The output resistance of the CE circuit is high and can come up to a hundreds k**Ω**. In this circuit configuration, the current gain $\beta$, or the static CE forward transfer ratio, often designated $h_{FE}$, is the ratio of the incremental change in the collector current $\delta I_C$ to the incremental change in base current, $\delta I_B$, at the constant $V_C$:

$$A_i = \delta I_E \big/ (\delta I_B) = \delta I_E \big/ (\delta I_E - \delta I_C) = 1 \big/ (1-\alpha) \tag{1}$$

$$\beta = \delta I_C \big/ \delta I_B \tag{2}$$

Because the $I_B$, is small in comparison with the $I_C$, the value of $\beta$ can range from 10 to 200 for different transistor. The transistor thus forms a current amplifier. Considering that

$$I_E = I_C + I_B \qquad \text{and} \qquad \alpha = \delta I_C \big/ \delta I_E , \tag{3}$$

we get

$$\beta = \delta I_C \big/ (\delta I_E - \delta I_C) = \left( \delta I_C \big/ \delta I_E \right) \Big/ \left( 1 - \delta I_C \big/ \delta I_E \right) = \alpha \big/ (1-\alpha) \tag{4}$$

The voltage gain $A_v$ of the CE configuration is of the same order of magnitude as for the CB circuit. The power gain $A_p = \beta A_v$ is many times higher than that for the CB circuit.

In the CE circuit, the output voltage is opposite in phase with respect to the input voltage, the positive incremental change in the input voltage causes the negative incremental change in the output, vice versa.

### 2.2.3 Common-collector configuration

In the CC configuration, the input voltage source is connected to the base circuit and the supply source with the load resistance to the emitter circuit. The input current is the $I_B$

and the output current is the $I_E$. The current gain, $A_i$, often referred to as the CC forward current transfer ratio and designated $h_{FC}$, is given by

$$A_i = \delta I_E \Big/ (\delta I_B) = \delta I_E \Big/ (\delta I_E - \delta I_C) = 1 \Big/ (1 - \alpha) \tag{5}$$

The input resistance of this circuit is high, tens of kilo ohms and the output resistance is low, 1 or 2 kΩ. The voltage gain, $A_v$ is a little less than unity, 0.90 to 0.95. This configuration is also called the emitter follower and is used for matching individual amplifier stages and signal source or loads to amplifiers. The characteristics of a transistor relate currents and voltages in the input and output circuits. The type of transistor connection determines its input and output circuits, therefore the characteristics relate different parameters for each circuit connection.

Thus, for a transistor connected in a CC configuration, the input circuit is the base circuit, and the input characteristics represent the plot of the $I_B$ as a function of the $V_{EB}$, with the $V_{EC}$ remaining constant. The output circuit for this type of connection is the collector circuit and the output characteristic relates the $I_C$ to the $V_{EB}$ with the $I_B$ as parameter. Figure 2.7c illustrates the shape of input (a) and output (b) characteristics for the pnp transistor connected in a CE circuit. At low values of the $V_{EB}$, the base current rises slowly because of the large p-n resistance which decreases with increasing current. As the $V_{EC}$ grows, the input characteristics shift to the right, which points to the fact that the $V_{EB}$ need to be increased to keep $I_B$ constant. The output characteristics show that in the operating region the $V_{EC}$

insignificantly affects $I_C$ because the $I_C$ mainly depends on the number of holes injected into the base, i.e. on the $I_E$.

### 2.2.4 Schottky diodes

The Schottky barrier formed at semiconductor/metal interfaces play an important role in the operation of the hybrid vertical architecture transistor. Many of the properties of the transistor are determined by the behavior of the Schottky barrier. The schematic energy diagram of a Schottky barrier is shown in Figure 2.8. The important quantity in this graph is $q\phi_B$ which is the actual barrier height. $E_F$ is the fermi level of this unbiased Schottky diode. $E_C$ is the conduction band of the semiconductor. $V_{bi}$ is the build in potential across the junction. The Schottky effect lowers the barrier by $q\Delta\phi$ and moves the Schottky barrier maximum away from the interface to $x_m$. $q\phi_B$ is determined by the combination of semiconductor and metal, typical values for Si based diodes are 0.5 - 1eV [26].

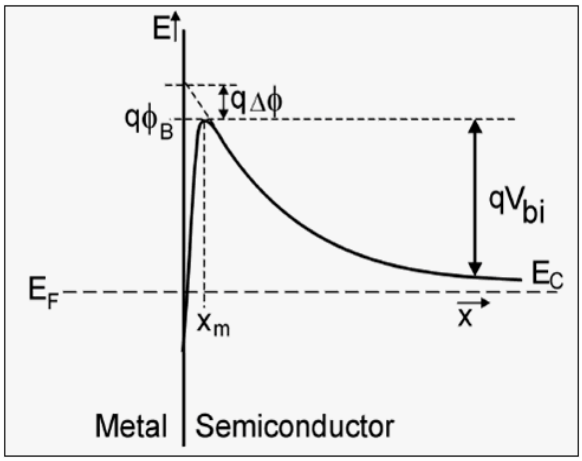


Figure 2.8 Energy diagram of n-type semiconductor Schottky diode, symbols are explained in the text [26]

## Schottky diodes

The current associated with an ideal Schottky diode using the thermionic emission theory is: $I = AA^{**}T^2 \exp\left(-\frac{q\phi_B}{kT}\right)\left[\exp\left(\frac{qV}{kT}\right)-1\right]$ (6)

Here $A$ is the diode area, $AA^{**}$ is the effective Richardson constant ($AA^{**}$ for Si is 1.1 x $10^6$ A/m$^2$/K$^2$), $T$ is the absolute temperature, $q$ is the electron charge, $\phi_B$ is the Schottky barrier height, $k$ is the Boltzman constant and $V$ is the applied voltage.

## 2.3 Magnetic-field-effects on organic semiconducting materials and devices

Magnetic-field-effects are defined as changes caused by an applied external magnetic field. These changes can be seen in a few different processes such as electroluminescence, photoluminescence, photocurrent and electrical injection current. Magnetic field effects are quantitatively expressed with:

$$\Delta MFE / MFE = \left[ \left( S_B - S_0 \right) \right] / S_0 \quad (7)$$

where $S_B$ and $S_0$ are the signal intensity with and without external magnetic field, respectively. Although the MFE on electroluminescence, photoluminescence, photocurrent and electrical injection current in organic semiconducting materials and device have been studied in the past, renewed interest has increased very recently due to the recent discovery of MFE. The MFE does not posses any magnetic field orientation dependence. It seems generally agreed that magnetic field can be employed as an external gadget to further enhance the electron injection of PBTs, increase the efficiency of OSCs, and modulate the efficiency of OLEDs. Basically MFE is a universal phenomenon and has been observed and studied in many polymers or small molecular OSCs. The MFE can be summarized as follow: (i) it can be either positive or negative, depending on the choice of material (the selection of emitter and cathode materials), device architecture, or operating conditions; (ii) it never reach saturation; and (iii) it is independent of magnetic field orientation. There are many theoretical models that have been proposed to explain the phenomenon namely (i) bipolaron [43]; (ii) exciton [44]; and (iii) exciton polaron interaction and electron phonon coupling [45a, 45b]. The first model is based on single charge carrier while the rest are based on bipolar charge carriers.

## 2.4 Models to explain MFE

To date, there are several theoretical models have been put forward in order to explain this effect. We will briefly discuss the hotly debated models which are bipolaron, exciton, and exciton polaron interaction models. The newest proposed model which is based on electron phonon coupling will also be treated here.

### 2.4.1 Bipolaron Model

Bipolaron model suggested that the magnetic field manipulates the mobility of free charge carriers and thus changes the current flow through a device [43]. The claims of this model:

i) This model claims that during the hopping processes, it is possible to have two charges (either electron-electron or hole-hole) located on the same hopping site and form a complex species called a "bipolaron". One should note the difference between bipolaron and e-h pairs or excitons. The difference is that the bipolaron is constituted by same charge carrier while e-h pairs and excitons are from two charge carriers with different charge. The formation of bipolaron can occur at hopping sites with a low energy. According to the Pauli exclusion principle, the formation of a bipolaron is only possible if the two charge carriers that are involved have an antiparallel spin configuration (spin up and spin down). If the two polarons have the same spin configuration, the formation of bipolaron is blocked. Figure 2.9 shows the hopping process with and without magnetic field. As we can see, with the absence of magnetic field, it is assumed that the spins of

free charge carriers are subjected to a random hyperfine field inside the material and it can easily flip and hop. It is argued that as a consequence, hops to all unoccupied and singly occupied sites are allowed since a moving charge carrier is expected to adjust its spin accordingly to have an antiparallel spin configuration in the case of a double occupancy. On the other hand, if the magnetic field is introduced to the device, it actually prevents spin mixing thus reducing the probability of bipolaron formation and at the same time force charge carriers to hop onto unoccupied states only. The presence of magnetic field reduces the number of available hopping sites for charge carrier transport since hops on single occupied sites are not allowed.

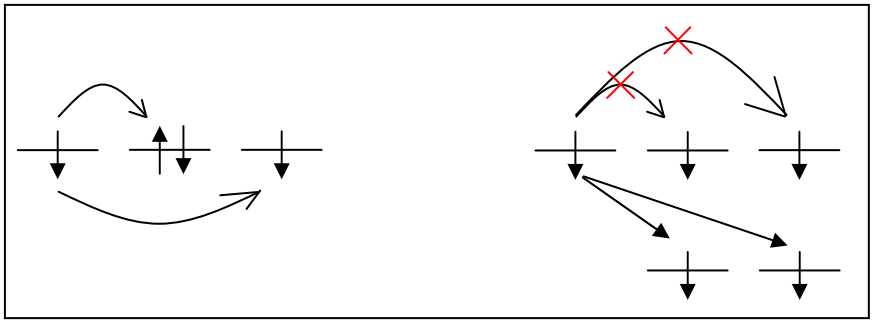

Figure 2.9 Schematic illustration of the hopping transport according to the bipolaron model (left panel) without external without external magnetic field and (right panel) with external magnetic field [43]

ii) One of the main points of this model is their hypothesis that charge carrier mobility and current density in a device are directly affected by changes induced by the magnetic field in the probability of bipolaron formation.

iii) This model claims that due to the increment of polaronic stabilization, charge carriers will have a low mobility when they form bipolaron during hopping transport, compared to the situation when no bipolaron is formed. Due to the fact that the bipolaron formation is reduced upon the introduction of magnetic

field, free charge carriers are expected to have a high mobility. At a certain fixed voltage, this can cause increment in the current and consequently resulting in a positive magnetoconductance. The presence of magnetic field reduces the number of available hopping sites for charge carrier transport since hops on singly occupied sites are not allowed.

iv) This model also claims that "spin blocking" mechanism is able to reduce the current density in the device and therefore causing a negative magnetoconductance. In general, the magnetoconductance can either be positive or negative depending on the contributions of the competing effects.

v) This model also numerically simulates the probability of bipolaron formation in a simplified two-site model. With the use of Monte Carlo simulation, this model predicts that it is possible to reproduce the two fundamental line shapes that have been observed in experimental data.

### 2.4.2 Exciton Model

The exciton model has been proposed by Prigodin et al. based on the effects of magnetic fields on the current flow through a device by changing the exciton formation rate [42]. The claims from this model:

i) This model claims that the exciton formation rate is generally the limiting factor for the current flow in bipolar OLED devices. The exciton formation rate is rather sensitive to magnetic fields as a consequence of the magnetic field dependent spin mixing between singlet and triplet e-h pairs.

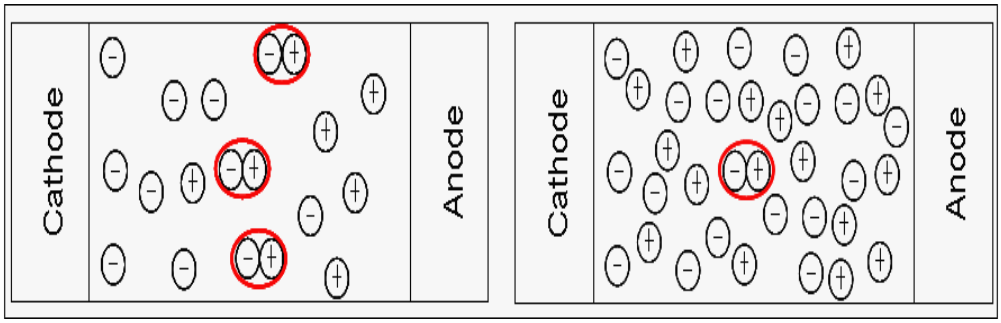


Figure 2.10 Illustration of free charge carriers and excitons in a bipolar OLEDs device according to the proposed model (left panel) without external magnetic field and (right panel) with external magnetic field [44]

As illustrated in Figure 2.10, the exciton formation rate directly causes a magnetic field dependence on the current in bipolar OLEDs. But, no explanation on the relation between exciton formation rate and the current flow in device is given.

i) This model assumes that e-h pairs can either dissociate into free charge carriers or can recombine and form excitons. The process of dissociation is thermally activated and occurs with dissociation rate constants $k_d^S$ and $k_d^T$ for singlet and

triplet e-h pairs, respectively. The process of recombination to an excitonic state occurs with recombination rate constants $k_r^S$ and $k_r^T$ for singlet and triplet e-h pairs, respectively.

ii) This model also considered a case where the dissociation rate is constants and does not show a strong spin dependence ($k_d^S = k_d^T$) and that singlet e-h pairs recombine much faster than triplet e-h pairs ($k_r^S$ ? $k_r^T$).

### 2.4.3 Exciton Polaron Interaction Model

Exciton polaron interaction model proposed by Desai et al. suggests that triplet excitons play the key role in the MFE mechanism [22,45]. Due to the long lifetime of triplet excitons a large number of triplets are present in an OLED during device operation and diffuse through the active material until they decay or dissociate. The following are the claims made in this model:

i) This model claims that the mobility of free charge carriers is affected by scattering events involving triplet excitons. The presence of magnetic field, will change the concentration of triplet excitons later adjust the current through the device. According to the model the interaction between free charge carriers and triplet excitons can be described in the following way:

$$P + T \rightarrow (P...T) \begin{cases} \xrightarrow{k_1} P + T \quad (i) \\ \xrightarrow{k_2} P + S_0^* \quad (ii) \end{cases}$$

where P is a free charge carrier, T is a triplet exciton, (P ... T) is a pair state of charge carrier and triplet exciton, and $S_0^*$ is an excited vibrational level of the molecular ground state. Process (i) is governed by a rate constant $k_1$ and describes the event that a free charge carrier is scattered by a triplet exciton, which is assumed to result in a decrease of the charge carrier mobility. Process (ii) occurs with a rate constant $k_2$ and is known as triplet polaron quenching [44]. It describes the event that a triplet exciton nonradiatively decays after interacting with a free charge carrier. Early study on magnetic field in organic crystals shows

that process (ii) is magnetic field dependent and that triplet-polaron quenching is reduced with increasing magnetic field strength [46].

ii) A main hypothesis in this model is that the magnetic field increases the intersystem crossing rate from triplet excitons to singlet excitons, resulting in a higher singlet concentration and a reduced triplet concentration. However, the exact mechanism causing this magnetic field dependence is not specified in the model.

iii) Due to the fact that the presence of magnetic field will reduce the concentration of triplet excitons, this model predicted a reduction in the number of scattering events for charge carriers, which is believed to increase the charge carrier mobility and enhance the current through the device (Figure 2.11).

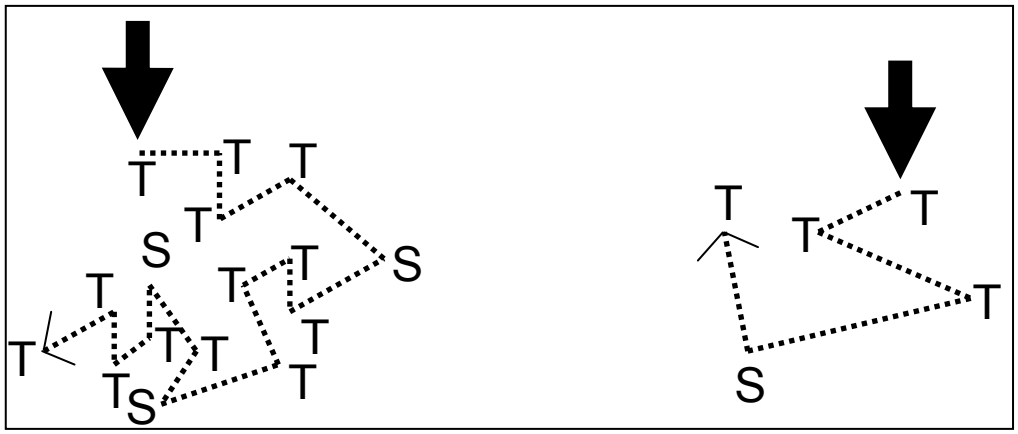


Figure 2.11 Illustration of the charge carrier transport with scattering events at triplet excitons according to the exciton polaron interaction model (left panel) without external magnetic field and (right panel) with external magnetic field [22,45]

Consequently, a positive magnetoconductance can take place. Meanwhile, the increase in the concentration of singlet excitons is supposed to improve the

luminescence output from the device causing a positive magnetoelectroluminescence.

iv) This model also claims that triplet excitons can generate a secondary current after dissociation thus provides a positive contribution to the overall current through the device. If the concentration of triplet excitons is reduced due to the application of magnetic field, this secondary current from dissociation will also decrease resulting in a negative magnetoconductance. Hu et. al. proposed a similar argumentation that triplet excitons can furthermore produce a secondary current by releasing trapped charge carriers from their traps [47-49]. According to the authors, if the triplet concentration is decreased with the presence of magnetic field, a negative magnetoconductance can be observed.

### 2.4.4 Electron Phonon Coupling Model

A newly proposed model has been put forward in attempts to explain the MFE in organic semiconducting devices. The electron phonon coupling model proposed by Xie et. al [45b] is based on Zeeman spin interaction. The claims of this model:

i) The model claims that the negative MFE is sensitive to the carrier concentration or doping in organic semiconductors. They found that the MFE decreases with the increment of carrier concentration at a weak magnetic field.

ii) Another main point in this model is that the MFE values are also sensitive in terms of charge-transfer integral. It is argued that under the same charge carrier concentration, the MFE is increased by a few percent as the charge-transfer integral is reduced.

iii) This model also claims that the charge-transfer integral increases with the temperature in a slow rate. Their hypothesis is that even with the presence of small thermal effect and a little change in charge-transfer integral, the spin relaxation and consequently the MFE will be affected.

iv) It is also proposed that MFE is sensitive to the electron-phonon coupling. In this case, it is claims that no MFE can be seen if the is no electron-phonon coupling parameter. But the increment in MFE value can be observed when the electron-phonon coupling is increased.

v) From the numerical simulation and the primary idea of this model is that the fitting parameter is related with the electron phonon coupling

parameter. This model speculates that a large fitting parameter corresponds to a weak electron phonon coupling.

CHAPTER 3

# Synthesis and characterization of self-doped sulfonated polyaniline for organic transistor

## 3.1 Chemical deposition

Chemical deposition refers to the deposition of films on a solid substrate from a reaction occurring in a solution (almost always aqueous). Chemical deposition can be carried out in both acidic and alkaline solutions, but most chemical reactions have been carried out in alkaline solution. In principle, chemical deposition can be used to deposit any compound that satisfies four basic requirements.

i. The compound can be made by simple precipitation. This generally, although not exclusively, refers to the formation of a stoichiometric compound formed by ionic reaction.
ii. The compound should be relatively insoluble in the solution used.
iii. The compound should be chemically stable in the solution.
iv. If the reaction proceeds via the free anion, then this anion should be relatively slowly generated (to prevent sudden precipitation).

## 3.2 Sample preparation

An organic PBT consists of a number of discrete layers, formed from organic and inorganic materials. Below are details on device fabrication steps and materials used.

### 3.2.1 Materials

Ammonium peroxydisulfate, $(NH_4)_2S_2O_8$ (99.99 %, Fluka) was used without any prior purification.

Aniline, $C_6H_7N$ (99.0 %, Sigma Aldrich) was purified by vacuum distillation prior to use.

Metanilic acid, $C_6H_7NO_3S$ (99.999 %, Sigma Aldrich) was used as purchased.

Ultra pure deionized water (Mili-Q, R > 18.2 MΩ) was used in all experiments.

### 3.2.2 Substrate cleaning

The organic transistors are prepared onto n-Si substrate. But before the fabrication steps took place, the Si cleaning procedures based on multi-step processes are followed and below are chemicals used [50]:

i- sulfonitric acid (99 % purity purchased from VETEC)

ii- distilled water

iii- acetone (99.5 % purity purchased QHEMIS)

iv- isopropanol (99.5 % purity purchased from VETEC)

v- hydrofluric acid:distilled water (1:10 concentration)

Firstly we place Si substrate in ultrasonic bath in sulfonitric acid for 20 minutes to remove any metallic contaminations and organic substances. Before Si substrate is sonicated in acetone for removal of organic residues, it is placed in sonicator in distilled water in order to remove residual acids. After that, the substrate is placed again in sonicator for 20 minutes in isopropanol, for removal of any acetone residue that have stayed on the Si substrate. These are then dried with air compressor.

Lastly, and the most critical step is for the removal of surface oxide layer, Si substrate was etched in a 5 % aqueous solution of hydrofluoric acid (HF). The Si substrates are soaked perpendicularly to the surface of the solution for a short time (5 s) since it reacts rapidly. Since oxide layer is hydrophilic and pure Si is hydrophobic, a non-wetting surface is clean of oxides and is just enough to dry with a compressed air gun. As one knows that Si dioxide is hydrophilic, if in the case of when removing the Si substrate from the solution and there still present drops of its surface, this implies that not all the oxide layer was removed, then all the above processes need to be repeated until the Si substrate is completely clean.

### 3.2.3 Synthesis of sulfonated polyaniline

We adopted a similar synthesizing process of SPAN from previous work [51] and the only difference is that we did not use any physical support to hold the Si substrate. We left the substrate floating on top of reaction solution. The synthesis of SPAN was carried through one simple technique. $(NH_4)_2S_2O_8$ was used as an oxidant agent, in the presence of protonic acid as an external agent. Whereas, $C_6H_7N$ was used as a monomer and also as auto-dopant with the presence of $C_6H_7NO_3S$. The preparation of SPAN was carried through for an amount of 500 mL and the procedures are divided into two parts:

**Part A**

0.245 g of $C_6H_7NO_3S$ was placed in 500 mL beaker. After that the beaker was filled with purified mili-Q water until the level of 400 mL, led to the ultrasonic bath for 6 min. Right after 6 min in the ultrasonic bath, the solution in the beaker was deposited in a 500 mL conical flask, where later $C_6H_7N$ (65 μL) was added into it. The remain of the conical flask

(100 mL) was filled with mili-Q water and finally taken to the refrigerator for 1 h at a temperature of approximately 5 ºC.

**Part B**

2.85 g of $(NH_4)_2S_2O_8$ was placed in a small beaker of 80 mL, filled with 62 mL of mili-Q water. Afterward, it has been taken into the ultrasonic bath for 6 mins and finally taken to the refrigerator for 1 h. Finally, after 1 h, those solutions were mixed together and stirred up for 1 min.

Figure 3.1 shows the SPAN during chemical deposition process on the second day. Figure 3.1a shows two beakers from the front view while Figure 3.1b shows the substrates from the top view.

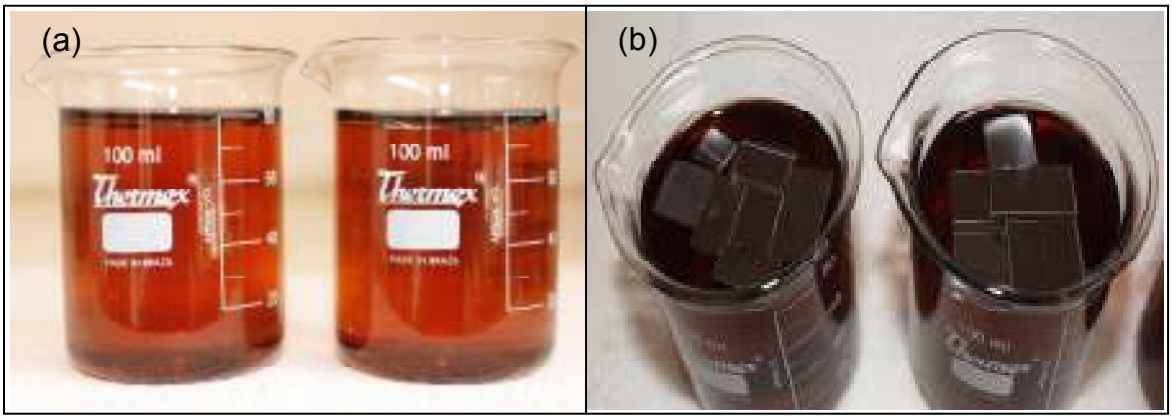


Figure 3.1 Sulfonated Polyaniline is under preparation. Figure (a) is from front view and figure (b) is from top view

The development steps of SPAN film are illustrated in Figure 3.2. A cleaned Si substrate right after cleaning process and ready to be placed in the beaker (Step i). Step ii

represents a placing of the Si substrate onto the reaction solution. The reaction solution is basically transparent in color (Day 1). Step iii is the reaction solution on day 12 and the Si substrate is slightly lower down. After day 12, the Si substrate is recovered from the reaction solution and steps iv and v are rinsing with copious of distilled water and drying it with air gun, respectively. Finally place the Si substrate in the vacuum furnace for 60 min at 50 °C for removal of water residue. All steps are the basic buildup sequence for ultrathin film of SPAN.

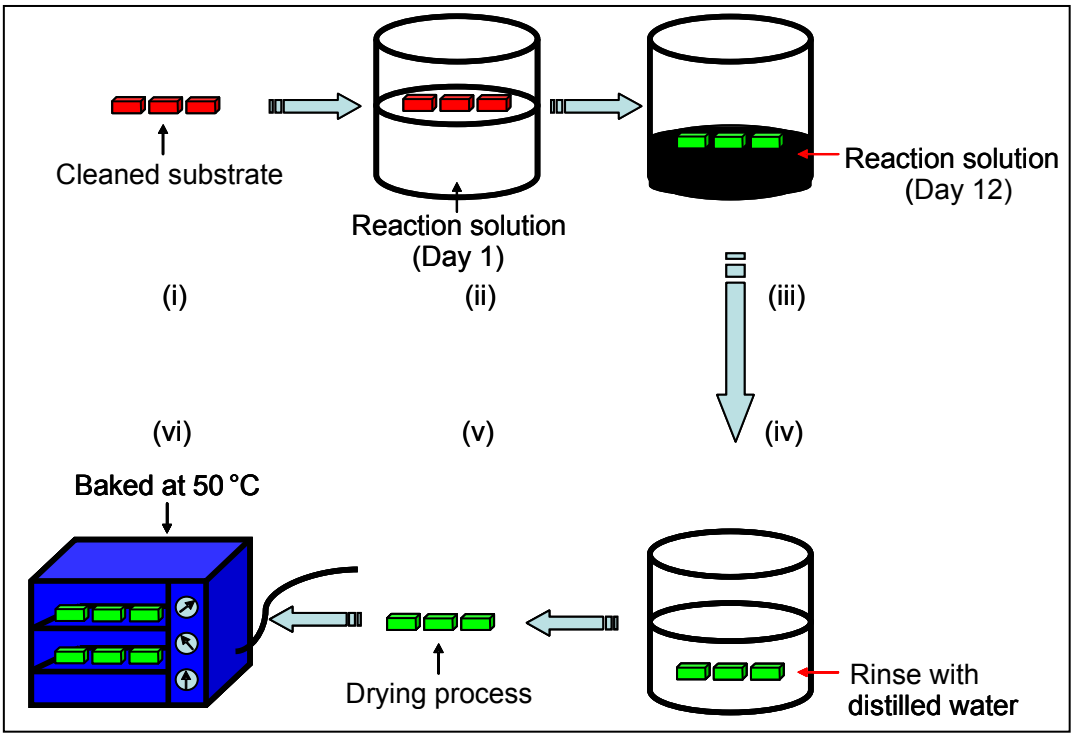


Figure 3.2 Schematic route for SPAN film deposition process employed a self-assembly method

Figure 3.3 below shows the SPAN with 200 nm thick deposited at room temperature.

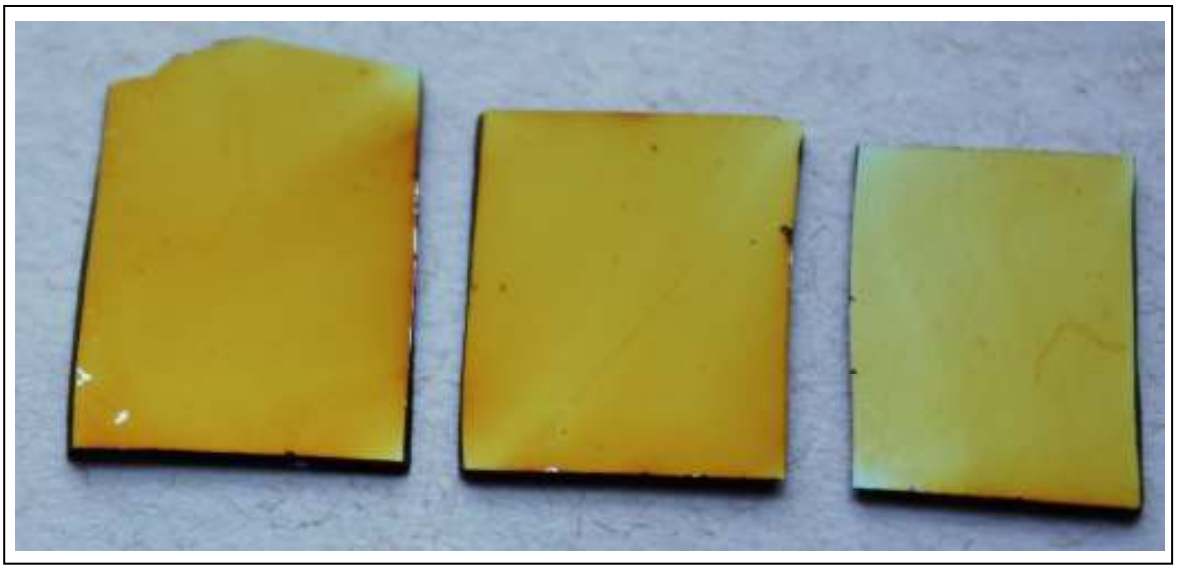

Figure 3.3 Sulfonated polyaniline deposited on top of n-type silicon substrates. The thickness is estimated to be ~ 200 nm

## 3.3 Characterizations

We divided the characterization of SPAN for 2 different categories which are:

i) Physical Properties

ii) Chemical Properties

For physical property of SPAN film, we have performed single characterization on film morphology. Apart from these, we also performed complete characterizations for chemical property of SPAN film, which consists of Fourier Transform Infrared (FTIR), Ultraviolet Visible Near Infrared (UV-VIS-NIR), MICRO-RAMAN, and Thermogravimetric Analysis (TGA). Physical characterizations of SPAN film were carried out at Department of Physics while all chemical characterizations were performed in Department of Chemistry.

### 3.3.1 Physical properties

**Morphology**

We performed the morphology study of the SPAN film by means of an Optical Microscopy. All Optical Microscopy scans were performed in the presence of air. We also carried out an Atomic Force Microscopy (AFM) analysis was also conducted using tapping mode. For surface morphology studies, we have used SPAN deposited on top of Si substrate.

### 3.3.2 Chemical properties

**Fourier-Transform Infrared (FTIR) spectroscopy**

We collected all spectra using a Fourier Transform Infrared (FTIR) Vertex-70 spectrometer (Bruker Optics, Germany) equipped with a narrow band DTGS detector and an attenuated total reflection (ATR) accessory with a zinc selenide crystal. The temperature variations at the crystal surface did not exceed 0.2 °C at any preset temperature. The whole instrument was with a stream of argon heated to approximately 26 °C. The spectra were obtained in attenuated total reflectance mode and each spectrum was an average of 16 scans were collected for each measurement over spectral range of 400-4000 $cm^{-1}$ with a resolution of 4 $cm^{-1}$, recorded with scanner velocity of 10 kHz using a Blackman-Harris 3-term apodization function, and a level of zero-filling equal to four.

To collect an IR spectrum, we prepared the SPAN film on top of Si substrate with a dimension of 1 cm X 1 cm. The SPAN-side down was placed onto the zinc selenide ATR crystal. To ensure reproducible contact between the SPAN film and the crystal, we applied always the same pressure on top of samples of the same type (torque setting of 50 centi-Newton-metres for SPAN; according to the manufacturer, these settings correspond to a pressure of 1.5 kBar, applied over the zinc selenide surface), and kept the samples in place for 10 min before collecting the spectra. The data were analyzed using OPUS version 6.5 software.

### Ultraviolet-Visible-Near-Infrared (UV-VIS-NIR) spectroscopy

Spectra of SPAN film were recorded with the film deposited onto quartz cover-slips 18 $mm^2$ (Deckglaser, Germany). The spectra of this film were recorded with bare quartz cover-slips as the reference. The UV-Vis absorption spectra were carried out using Agilent 8453 spectrometer. The absorbance spectra ranging between 250 to 1100 nm were measured at different equilibrated potentials.

### Micro-Raman spectroscopy

The Raman spectra were obtained in a Renishaw Micro-Raman Image spectrophotometer, coupled to an optical microscope that focuses the incident radiation down to a spot of approximately 1 μm. A He-Ne laser (emitting at $\lambda$ = 632.8 nm) was used, with an incident power of 0.2 mW over 200-2000 $cm^{-1}$ range. The recorded spectra were taken from SPAN deposited at room temperature on top of Si substrate. The Raman spectra thus obtained were fairly smoothened and baseline-corrected for better visibility.

### Thermal analysis

Thermogravimetric Analysis (TGA) measurement was carried out using Netzsch STA 409 equipment, in static air (with no air flow). For TGA analysis, the temperature was between 0 and 1000 °C using alumina crucibles.

## 3.4 Results and Discussion

### 3.4.1 Physical properties

#### Optical Microscopy

SPAN deposited on silicon substrate has better adhesion and passed our peeling test. Under Optical Microscopy, SPAN films deposited on silicon substrate have a smooth surface, homogenous (Figure 3.4a), and there are numerous tiny opening voids distributed all over the surfaces, and there was no fibril morphology as observed in the electrochemically polymerization process [52]. However as one can observed in Figure 3.4b for 61 nm of SPAN, there are several big opening voids on the surface. These big opening voids will be discussed later in Chapter 4.

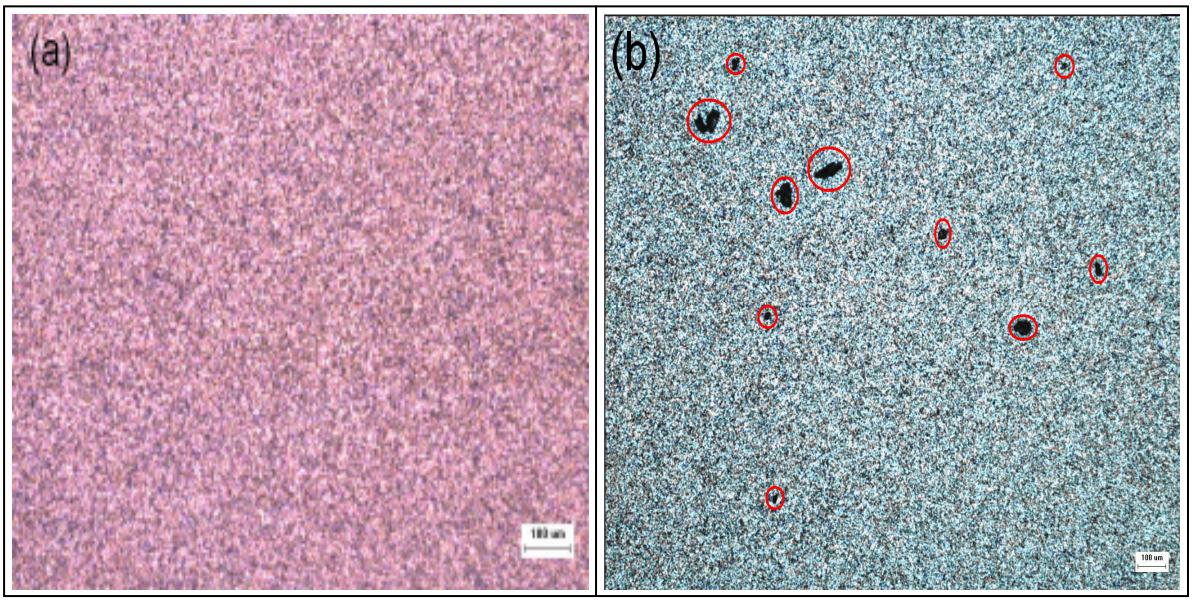


Figure 3.4 Optical Microscopy images of SPAN with different thicknesses deposited on silicon wafer with the thickness of (a) 156 nm, and (b) 61 nm

### Atomic Force Microscope

Figure 3.5 displays the SPAN film morphology with 156 and 61 nm thicknesses, respectively. The surface roughness of polymer film deposited on silicon substrate was estimated to be 6 and 20 nm for polymer with 156 and 61 nm, respectively. No damage was done on the SPAN film deposited on silicon substrate when the cantilever scanned through it. From Figure 3.5a, a small roughness obtained from this scan suggested that SPAN deposited on silicon is smooth and homogenous. From Figure 3.5a, the surface morphology of the SPAN film is homogenous and less hills and valleys can be seen from this figure. Meanwhile, from Figure 3.5b, the SPAN film morphology having the thickness of about 61 nm, it seems like the surface is very rough and uneven over the entire surface. There are a lot of hills and valleys can be seen from this Figure 3.5b.

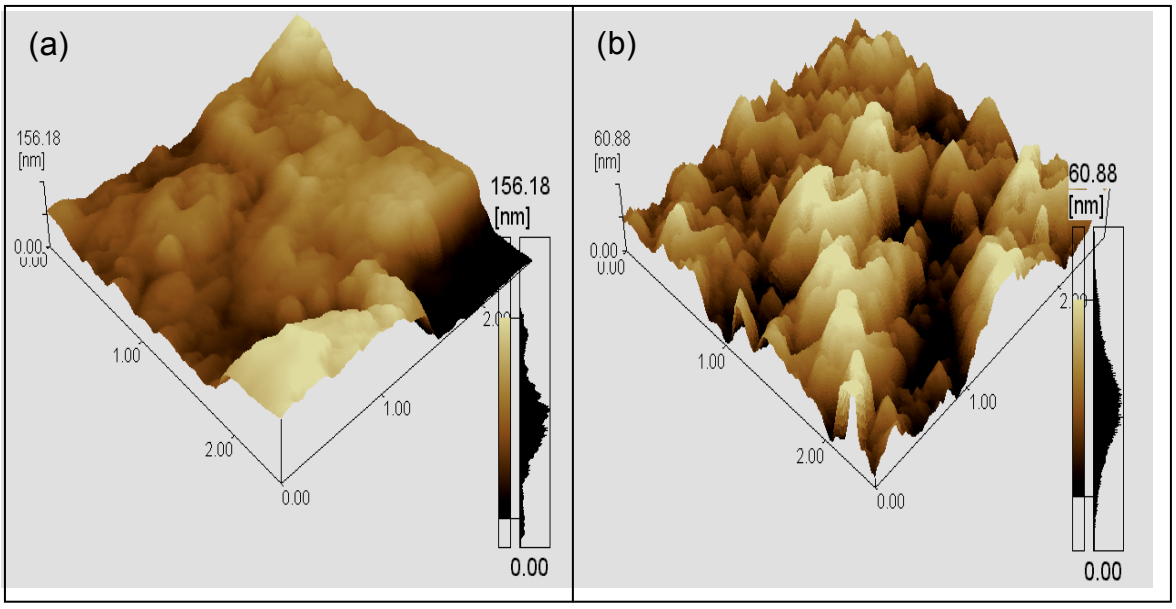


Figure 3.5 AFM images of SPAN with different thicknesses deposited on silicon wafer with the thickness of (a) 156 nm, and (b) 61 nm

### 3.4.2 Chemical properties

**Fourier-Transform Infrared (FTIR) spectroscopy**

The structure of the self-doped conducting polymer films was investigated by absorption FTIR. Except for differences in relative absorbance, all SPANs' FTIR spectra have almost the same features. Figure 3.6 displays all characteristics bands attributed to the absorption of the $SO_3^-$ group at 1082 $cm^{-1}$, 1024 $cm^{-1}$ and 618 $cm^{-1}$, confirm that polyaniline is doped with $SO_3^-$ directly [53,54].

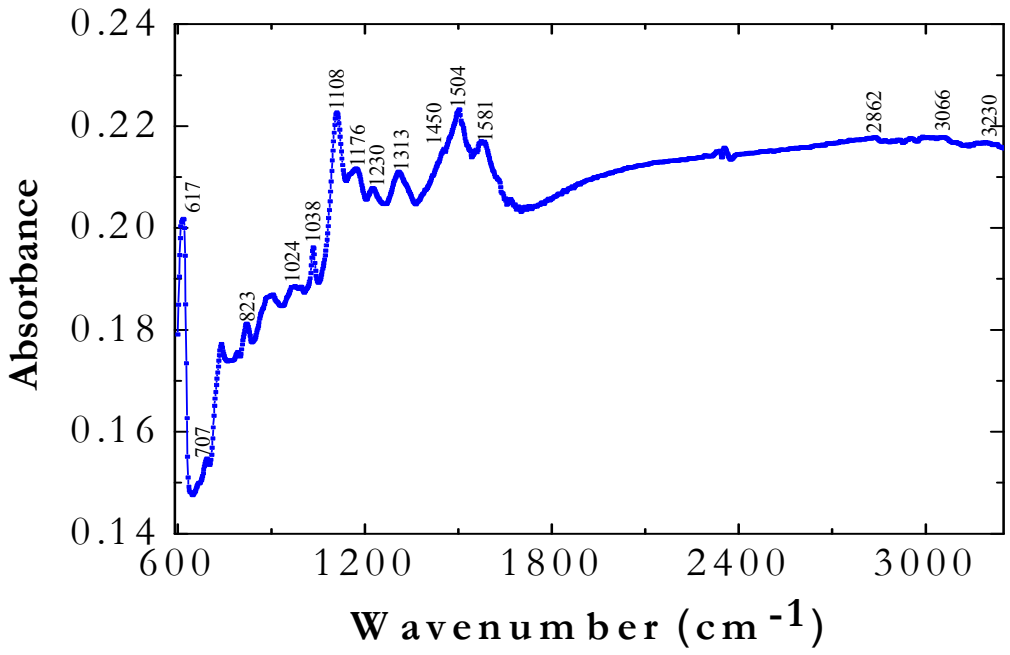


Figure 3.6 FTIR spectra of SPAN recorded at room temperature

These bands are assigned to different vibrational modes, as presented in Table 1 [55]. From the FTIR spectra and according to the calculation methods [55], we are able to calculate degree of sulfonation of our self-assemble water soluble SPAN, which is approximately around 27 %. Figure 3.7 shows FTIR spectra of PANI.

| IR band/cm$^{-1}$ | Bond | Group vibration mode |
|---|---|---|
| 3230 | N-H | Aromatic amine stretching |
| 3066, 2862 | C-H | Aromatic stretching |
| 1581 | C=N | Quinoneimine stretching |
| 1504 | C-C | Aromatic stretching |
| 1450 | $NH_4$ | N/A |
| 1425.9 | C=C | Aromatic stretching |
| 1313 | C-N | Secondary aryl amine stretching |
| 1176.5 | C-H | In-plane bending aromatic |
| 1081.8, 1024.2 | S=O | Sulfonated stretching |
| 1038 | S-O | Stretching |
| 823 | C-H | Out-of-plane bending aromatic |
| 707 | C-S | Aromatic stretching |
| 618 | S=O | Sulfonated stretching |

Table 1 Assignment for IR absorption bands in SPAN

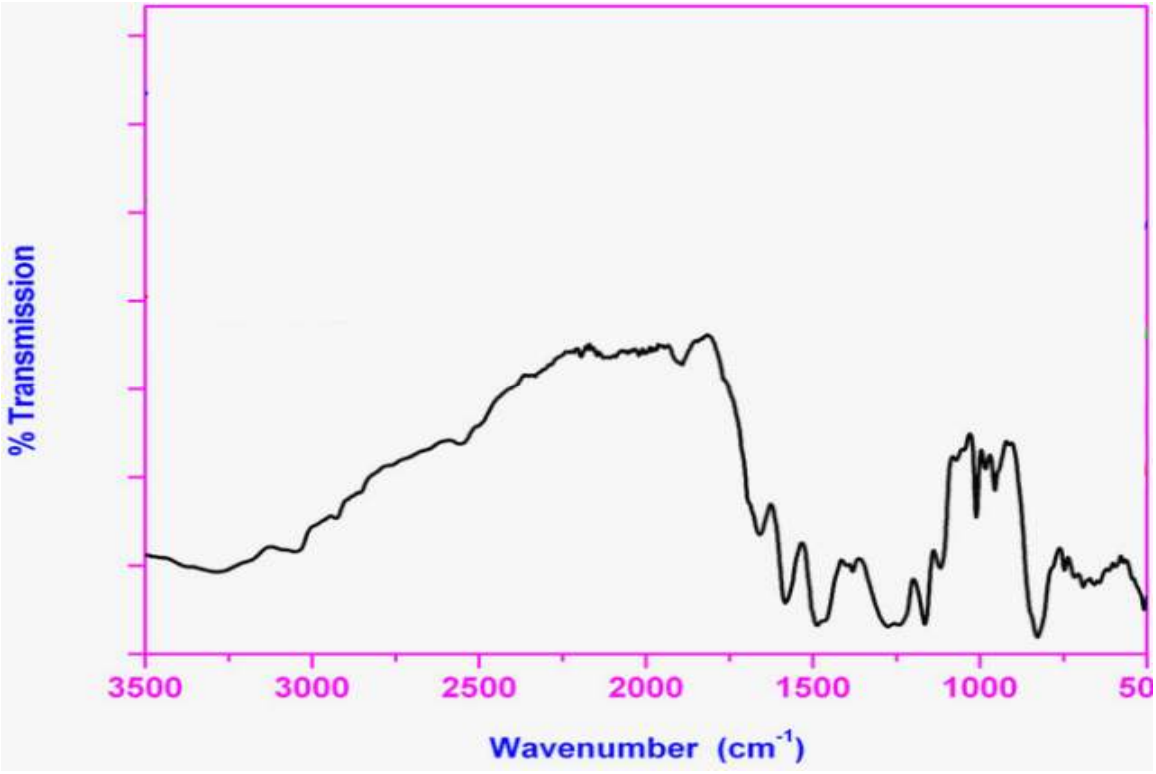


Figure 3.7 FTIR spectra of PANI [56]

### Micro-Raman Spectroscopy

Figure 3.8 shows Raman spectra for the films of SPAN on silicon substrate recorded at room temperature. In the present work, these films have been prepared by copolymerization of aniline with metanilic acid.

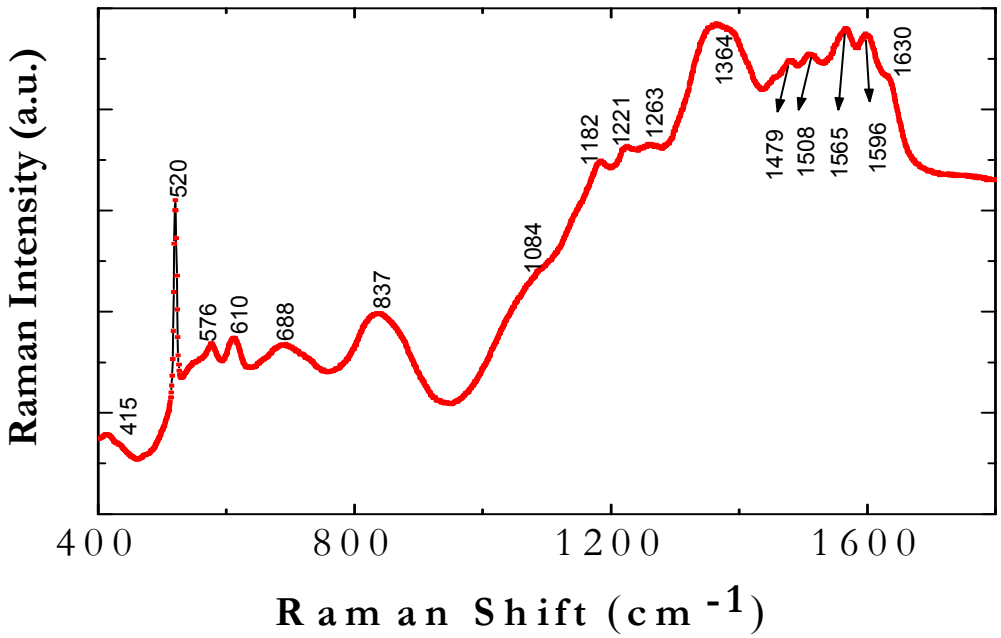


Figure 3.8 Raman spectra of SPAN recorded using a He-Ne laser; λ = 632.8 nm laser excitation

The spectra obtained have many features characteristic for polyaniline, where the frequencies of the major bands and their assignments are summarized in Table 2 [57], however, some specific features should be mentioned. In general, there are three regions in Raman spectrum of SPAN that are sensitive both to the level of oxidation, and the protonation degree:

(1) 1100–1210 $cm^{-1}$ region, where C–H in-plane-bending of benzene or quinone type rings are most prominent;

(2) 1216–1221 $cm^{-1}$ region with characteristic C–N, C=N and C~$N^+$ (where '~' denotes as an intermediate bond between a single and a double) stretching;

(3) 1504–1514 $cm^{-1}$ region with the dominating C–C and C=C stretching of benzene and quinone type rings, respectively.

| Frequency ($cm^{-1}$) | State[a] | Assignment |
|---|---|---|
| 1626-1630 | B | C=C ring stretching |
| 1585-1600 | Q | C-C ring stretching |
| 1506-1516 | Q | Cd=N stretching |
| 1480-1486 | Q | Cd=N stretching |
| 1339-1370 | SQR | C~$N^+$ stretching |
| 1257-1266 | B | C-N stretching |
| 1190-1197 | B | C-H in-plane-bending |
| 1171-1174 | Q | C-H in-plane-bending |
| 885 | B | in-plane-ring deformation |
| 830-836 | Q | in-plane-ring deformation |
| 800-815 | Q | C-H out-plane-bending |
| 712-724 | B | out-of-plane-ring deformation |
| 685-698 | Q | out-of-plane-ring deformation |
| 636 | B | in-plane-ring deformation |
| 511-526 | | out-of-plane C-N-C torsion |
| 412-420 | Q | out-of-plane C-H wag |

[a] B = Benzoid ring, Q = Quinoid ring, SQR = Semiquinone radical

Table 2 Major Raman band and their assignments for a SPAN film

Within the region of 1100–1210 $cm^{-1}$, one band located at 1182 $cm^{-1}$ corresponding to C–H in-plane bending appears less resolved as compared to the parent polyaniline. Although low in intensity, the band corresponding to C–N stretching of emeraldine base (amine sites) is well distinguishable from the parent polyaniline. For parent polyaniline, this band grows in high intensity, whereas nearly no growth of intensity for this band is observed for SPAN. The band corresponding to $C\sim N^{+}$ stretching in polaronic form appears best in SPAN. This band is located at 1364 $cm^{-1}$ with a relatively high intensity. This can be considered as one of the main difference of SPAN regarding the polaron band, where it is located at 1320–1340 $cm^{-1}$ in the parent polymer. The difference is observed for the band corresponding to C=N stretching in emeraldine base, located at 1508 $cm^{-1}$, where there is no growth of this band in the parent polymer. Figure 3.9 demonstrates Raman spectra of PANI.

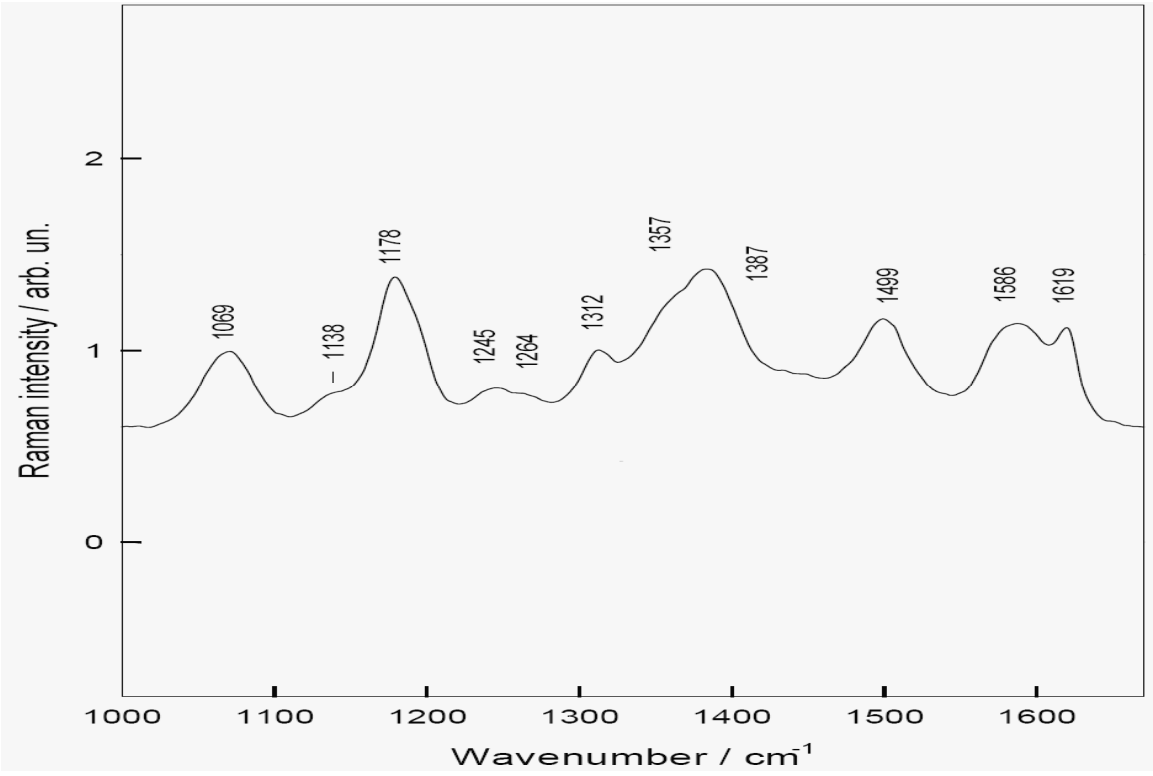


Figure 3.9 Raman spectra of PANI [58]

### Ultraviolet-Visible-Near-Infrared (UV-VIS-NIR) Spectroscopy

To study in more detail the spectral variations associated with different oxidation states of SPAN deposited on quartz, absorption spectra in UV-VIS region were monitored as a function wavelength from 250 to 1100 nm (Figure 3.10). The spectra in the UV-Vis range agreed with those reported early [59-61]. Three bands were observed at 850, 440 and 320 nm. The band at 320 nm was attributed to the π-π* transition of the aniline ring [52]. The band at 440 nm was assigned to the localized cation radical [60]. The absorbance at this wavelength initially increased with oxidation, and then decreased. This corresponds to the initial formation of radical cations that disappears upon further oxidation. The band at 850 nm corresponded to the metallic polaron [62]. The absorbance at 850 nm increased continuously with oxidation and shifted to higher energies in the NIR region. The behavior of the bands in SPAN was very similar to polyaniline. UV-Vis spectra of PANI is shown in Figure 3.11.

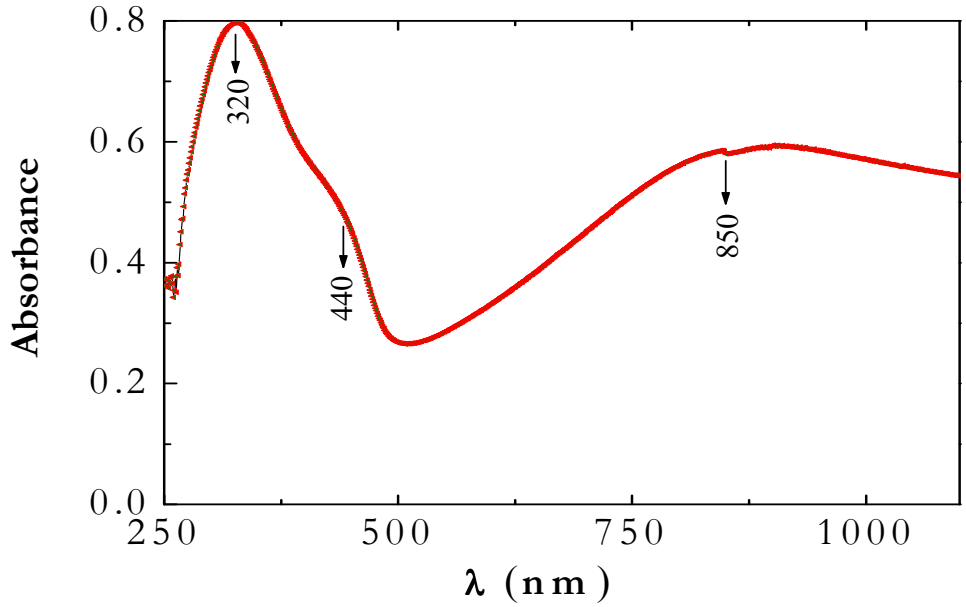


Figure 3.10 UV-VIS-NIR spectrum of SPAN film on quartz recorded at room temperature

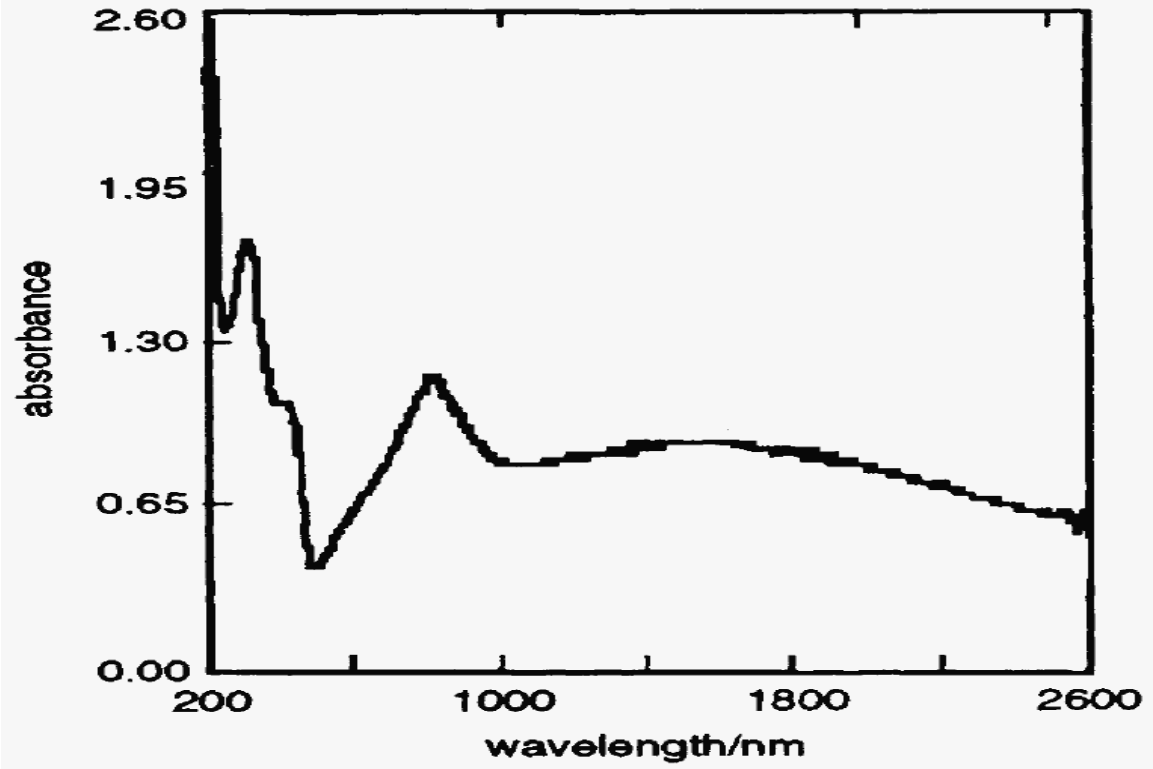


Figure 3.11 UV-Vis spectra of PANI [63]

### Thermal Analysis

To determine the stability of the SPAN, TGA measurements were made, yielding the results shown in Figure 3.12. The TGA thermogram (Figure 3.12) shows a weight loss starting at about 100 °C, which is probably due to the elimination of water molecules from the polymer structure and dopant ions.

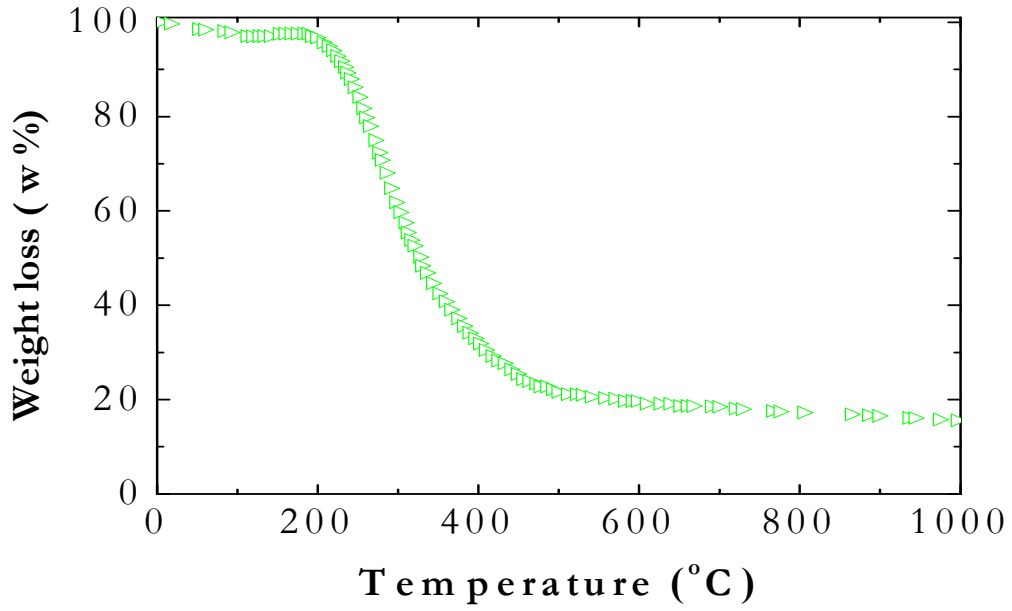


Figure 3.12 TGA curve of SPAN films obtained at room temperature

The second stage of weight loss, in the temperature between 200 and 500 °C, is presumably caused by the elimination of sulfonic acid groups from polymer chains and oligomers. The third decomposition step occurs from 360 °C, where the mass loss may be associated with the breakdown of the main chains in the polymer and there is no significant weight loss at temperature higher than 600 °C. TGA analysis shows that SPAN is thermally

stable up to 200 °C and sulfonic acid groups attached to the polymer backbone diffuse out from the polymeric backbone from temperature 210 °C.

We attributed this high thermal stability of SPAN film due to the existence of the sulfonic acid groups. This observation indeed in a good agreement with the fact that the presence of sulfonic acid groups in the parent polymer backbone increases its thermal stability. Figure 3.13 presents the TGA spectra of PANI.

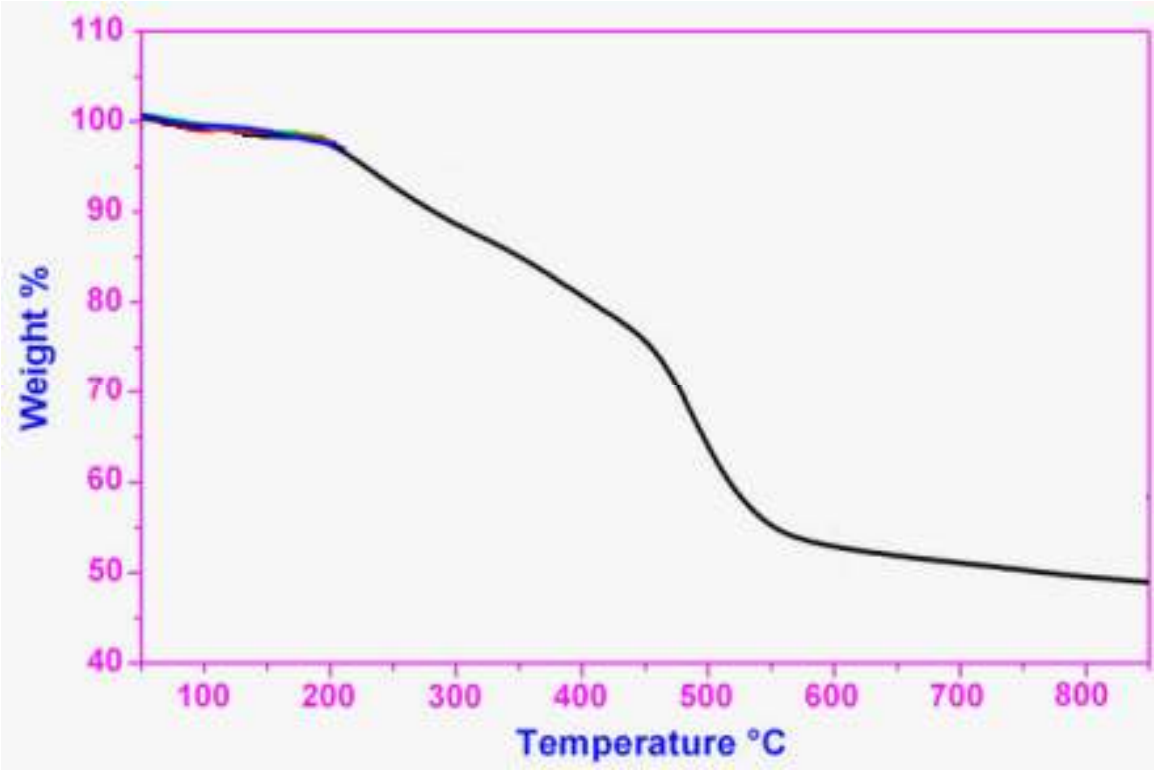


Figure 3.13 TGA spectra of PANI [56]

CHAPTER 4

# Magnetic-field-effect in nonmagnetic organic transistor

## 4.1 Introduction

In this section, we will present the results for all four different nonmagnetic organic transistors. In each structure, the results are divided into 2 main subsections as follow:

i) two terminal measurements

ii) three terminal measurements

Our nonmagnetic organic transistors are as below:

i) n-Si/SPAN/$Alq_3$/Ca/Al

ii) n-Si/SPAN/$Alq_3$/$C_{60}$/$V_2O_5$/Al

iii) n-Si/SPAN/$C_{60}$/$Alq_3$/$V_2O_5$/Al

iv) n-Si/SPAN/$C_{60}$/$Alq_3$/$C_{60}$/$V_2O_5$/Al

The first section is devoted to a single emitter layer organic transistor. In this section we will discuss about bipolar device and also unipolar devices; namely i) electron-only device and ii) hole-only device. We will also discuss regarding high MFE that reached up to $10^3$ % at only 200 mT.

For the second and third section, we will talk about double emitter organic transistor. In this section, we will also discuss about the effects of voids in our transistor. Furthermore, we will also talk about the possible mechanism, for the reduction of $\alpha_O$ and the increment of $\beta^*$ with the increment of SPAN film thickness. Moreover, we are also presenting and discussing the correlation between voids and MFE.

In the final section, we dedicated to a tri-emitter layer organic transistor. This structure is rather trivial since it involved a complicated stack of layers.

## 4.2 Experimental

### 4.2.1 Organic transistor fabrication

Device Fabrication

i) Bipolar Device

The fabrication started with single-side polished 200 μm ‹100› n-type silicon wafers with a high resistivity (ρ > 10 Ω.cm). The thickness of the substrate is 250 μm. Using a slow chemical deposition method, a homogenous SPAN film of 200 nm thick was deposited on the front clean side of the Si. A homogenous film was required to make the subsequent layer homogenous. The SPAN surface was partially covered with a thick poly(methyl methacrylate), PMMA, layer by immersing it, using a saturated PMMA:acetone solution for the purpose of preventing future electrical leakage current or short-circuit problem. Before the deposition of an insulating layer, the backside of the substrate was cleaned with ammonium hydroxide, $NH_3O$ in order to remove any remaining SPAN film. The Si unpolished side was covered with a thin In-Ga eutectic alloy. This process was done to provide ohmic contact to the collector terminal. In the sequence, a 60 nm thick emitter layer ($Alq_3$) was deposited onto the SPAN film using thermal sublimation at a base pressure of $10^{-6}$ Torr, which was followed by a top metal contact Ca/Al double layer evaporation, 1 mm linewidth, evaporated through a shadow mask. The device active area, determined by the superposition of the Ca/Al and insulator uncovered SPAN, was 1 $mm^2$ (Figure 4.1). For devices without the insertion of Ca layer, ultrathin ( < 5 nm) $V_2O_5$ was introduced before the evaporation of the top metal contact.

ii) Unipolar Device

a) Electron-only

The hybrid electron-only sandwich devices were prepared onto ‹100› n-type Si (ϱ > 10 Ω.cm). In the sequence, an insulating PMMA thick layer was deposited by spin-coating on the cleaned part of the n-Si, in order to further prevent the direct contact between the emitter and collector electrodes. The deposition of 60 nm $Alq_3$ served as the emitter layer, followed by Ca (to improve electron injection) and Al were sequentially made without vacuum break on the n-Si polished side. For the finally step of electron-only transistor fabrication, a 60 nm of Al layer was deposited on the Si backside.

b) Hole-only

The hybrid hole-only sandwich devices were prepared onto ‹100› p-type Si ($10^{-15}$ $cm^{-3}$). In the sequence, an insulating PMMA thick layer was deposited by spin-coating on part of the p-Si, in order to further prevent the direct contact between the emitter and collector electrodes. The deposition of 60 nm $Alq_3$ and followed by Au were sequentially made without vacuum break on the p-Si polished side. Finally, 60 nm of Al layer was deposited on the Si backside. In all cases, layer thickness was determined using a Dektak[3] surface profiler.

In this thesis, all devices were characterized at laboratory atmosphere conditions, and the electrical characterization was performed in the dark and we observed that these devices

showed high reproducibility and stability during measurement sessions. The material combination favored stability since n-Si and SPAN were quite stable, which means that the degradation can be overcome by encapsulation strategies that avoid water and oxygen contamination.

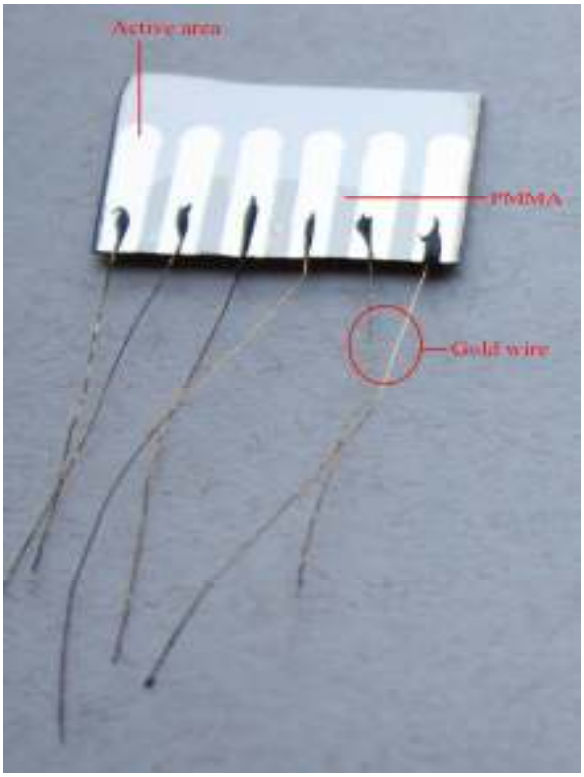


Figure 4.1 A real device fabricated at room temperature

## 4.3 Characterizations

### 4.3.1 Electrical properties

The electric characterization was made in the dark using an Agilent 4155C semiconductor parameter analyzer and consisted of two- and three-terminal measurements. The integration time or scan rate for all measurements was 0.5 s/point and the current measurement interval was 0.1 s. In the two-terminal measurement, the voltage was applied between two electrodes, measuring the current that passed through them. Therefore, measurement was made between all terminals of the transistor: base and collector, base and emitter and also collector and emitter. In the presentation of electrical characterizations results, we will use throughout the text the subscripts E, B and C to denote the emitter, base and collector currents I and voltages V, respectively. Additionally, we will also use $V_{ij} = V_i - V_j$ (i, j = E, B or C).

In three-terminal measurement, we maintained one terminal grounded, while the other two were submitted to ramp of current and the current is measured in each terminal. Two different ways of measurements were used:

i- common-base

ii- common-emitter

In the common-base characteristics (Figure 4.2a), the base terminal was grounded. In this type of measurement, the $I_C$ was measured as a function of the $V_{CB}$ at constant $I_E$. The current source controlled the $V_{BE}$ in order to maintain the desired $I_E$.

Meanwhile the common-emitter characteristics (Figure 4.2b) were determined by measuring $I_C$ as a function of the potential difference between the collector and the emitter, common emitter voltage, for different values of $I_B$ or $V_{BE}$.

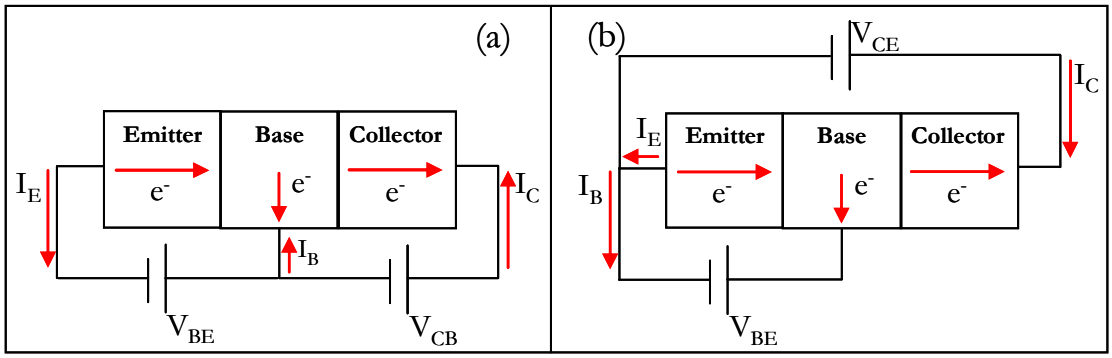


Figure 4.2 Illustrates the measurement diagram in two different ways of operation for n-type devices: (a) common-base; and (b) common-emitter

### 4.3.2 Magnetic-field measurements

The magnetic field on electric transport measurements was performed in the dark at room temperature using a pair of removable permanent magnets, and Agilent 4155C semiconductor parameter analyzer. The sample was placed on the sample holder (Figure 4.3) which was then placed between the magnet poles, adjusting the distance between poles to achieve the desired magnetic field strength in the sample position, which was determined by using a Hall probe. The current voltage characteristics were measured by scanning the voltage at a rate of 0.01 $V.s^{-1}$.

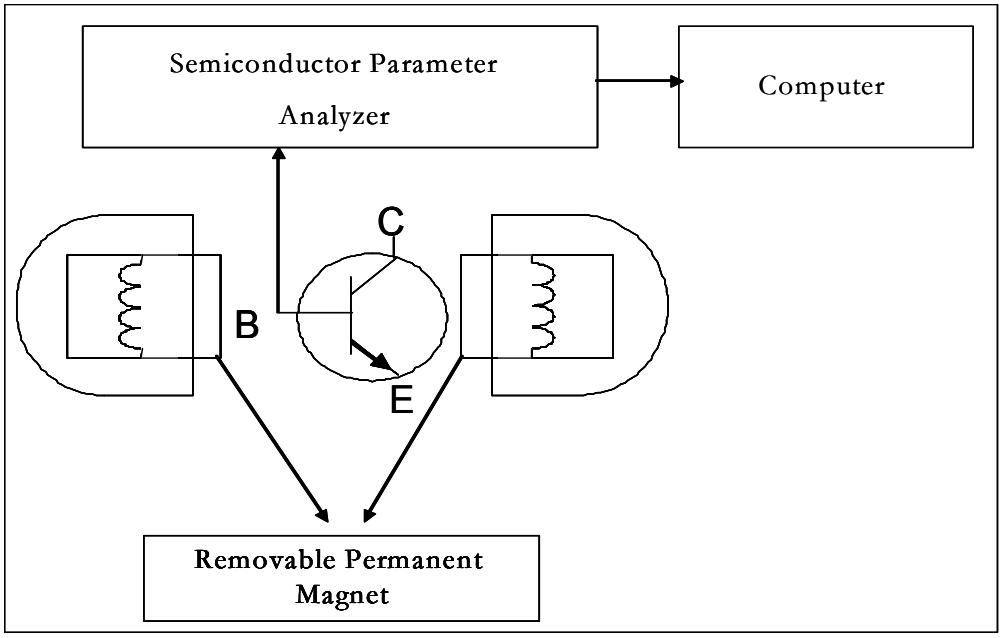


Figure 4.3 Experimental setup used for magnetic field effect measurement

## 4.4 SPAN/$Alq_3$ Heterostructure

### 4.4.1 Device structure

**Bipolar device (single emitter layer)**

In this device, the organic emitter, a 60 nm thick layer of $Alq_3$, was deposited by thermal sublimation in vacuum. To improve the electron transport into the organic semiconductor emitter layer, a 60 nm layer of Ca was deposited on top of the $Alq_3$ layer prior to the top contact metal electrode deposition, which consisted of a 60 nm thick Al layer. The resulting device has an active area of 1 $mm^2$. Another thick Indium-Gallium, In-Ga eutectic alloy layer was deposited on the Si unpolished backside to provide an ohmic contact for the collector terminal. The layers thicknesses were controlled during device preparation using a calibration curve and emitter related depositions were made at a base pressure lower than $10^{-5}$ Torr. Figure 4.4 presents a schematic structure of single emitter later device used in this study.

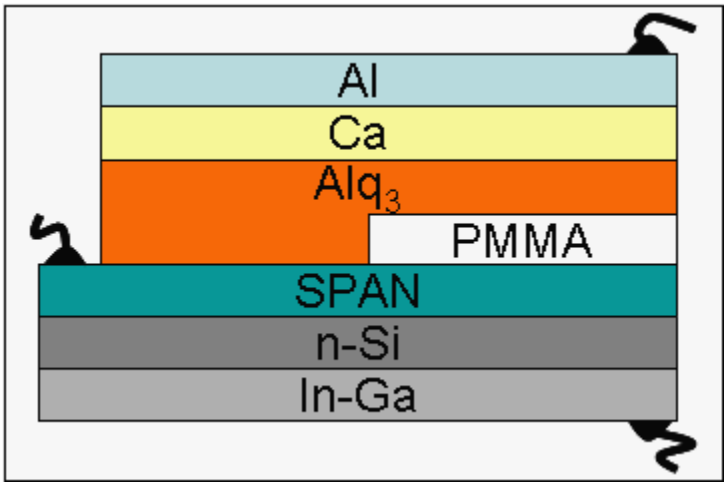


Figure 4.4 Schematic structure of single emitter layer device

### 4.4.2 Energy diagram

The energy level diagram of the n-Si/SPAN/$Alq_3$/Ca/Al device is schematically presented in Figure 4.5. In the case of n-Si/SPAN/$Alq_3$/Ca/Al device, a good ohmic contact between In-Ga and n-Si and the higher barrier height between SPAN and $Alq_3$, which is desirable for an asymmetrical PBT device to achieve high current gain, guarantee the SPAN/$Alq_3$ based PBT to operate well in the common-base and common-emitter modes [62].

The presence of the Ca implies that majority charge carriers arrive at the base region at slightly higher energy. This is due to the higher energy barrier between SPAN and $Alq_3$. Therefore, the recombination current in the emitter is further reduced and the SPAN/$Alq_3$ interface improves the PBT performance. The large energy barrier for electrons at the SPAN/$Alq_3$ does not impose constraints to transport, despite producing some charge accumulation and redistribution of the electric field inside the SPAN/$Alq_3$ bilayer. If the BC junction is reverse biased (base is negatively biased with respect to the collector), the electrons that have been transported through the base to the collector can be collected by this terminal.

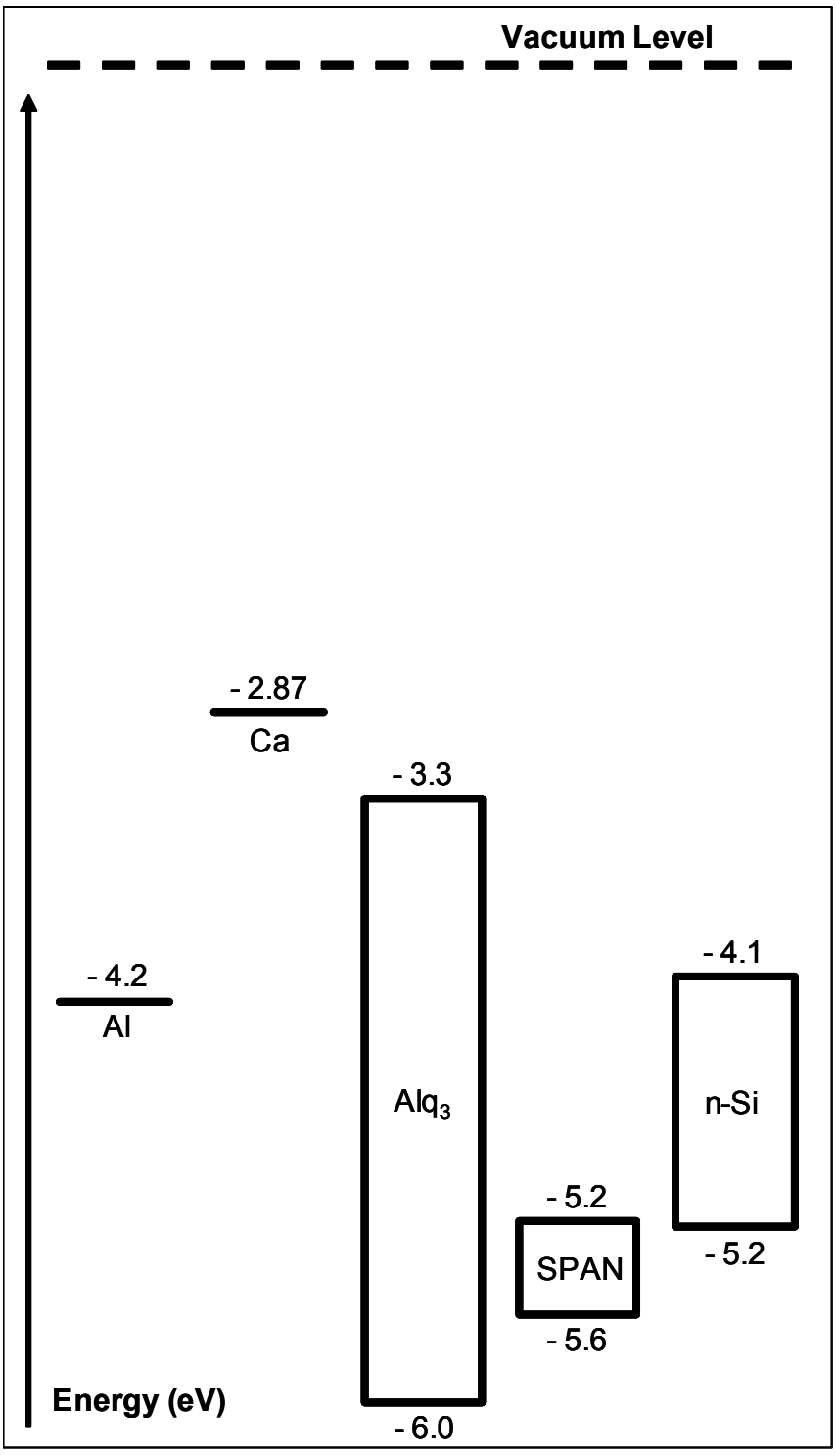


Figure 4.5 Simplified energy schemes of the materials used in device production [65a]

## 4.5 Results and Discussion

### 4.5.1 Two terminal measurements

All measurements and characteristics were sequentially performed twice: (a) without applied external magnetic field; (b) with an applied external magnetic field, $B$ = 100 mT. n-Si/SPAN/Alq3/Ca/Al device was measured for the same values of $I_E$ in a field of 100 mT applied parallel to the silicon surface of the sample; otherwise stated.

Figure 4.6 shows the two-terminal I-V characteristics for a typical transistor with SPAN layer thickness of 200 nm and $Alq_3$/Ca/Al thickness of 60 nm. Note that when the transistor is operating in the forward active mode, $V_{CB}$, $V_{BE}$ and $V_{CE}$ are all positive. The I-$V_{CB}$ characteristic shows that the collector-base, n-Si/SPAN junction behaves like a Schottky diode as expected and is reverse biased when $V_{CB}$ is positive. In Figure 4.6a, one can clearly see that there is no observable effect in the device. Meanwhile for comparison of the I-$V_{BE}$ and I-$V_{CE}$ (Figure 4.6b) characteristics show that in the forward active mode, i.e., $V_{BE}$ and $V_{CE}$ positive, a given value of voltage gives a significantly higher current between emitter and collector than between emitter and base. This means that electron transport from the emitter directly to the collector is significantly easier than from the emitter to and along the base, suggesting that there is a barrier at the EB junction and there are also conduction channels linking the emitter and collector that bypass this barrier, which supports the existence of pinholes.

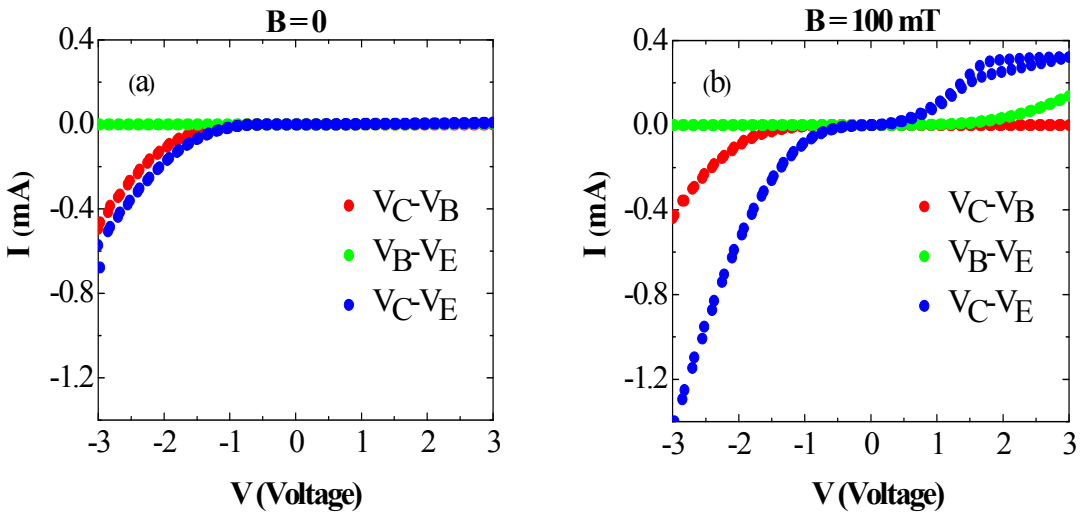


Figure 4.6 Two terminal characteristics between emitter, base and collector of n-Si/SPAN(200 nm)/$Alq_3$/Ca/Al device

In Figure 4.7, we present the comparison of I-V characteristics in the logarithmic scale, under absence and presence of $B$ = 100 mT. From Figure 4.7a, it can be seen that with the influence of magnetic field implies the increment of $I_E$ (Figure 4.7a). The most remarkable part, $V_{BE} < 0$ there is no obvious change in the current, so that with the presence of magnetic field, one can easily observe such a significant increment in the device current rectification. We made the same type of measurement using the SPAN and In-Ga terminals (Figure 4.7b), without observation of MFE. We also could not find evidence of dependence of MFE on magnetic field orientation. We tested the orientation of 0 to 360° in steps of 30° and our observation is in agreement with MFE results reported by other groups.

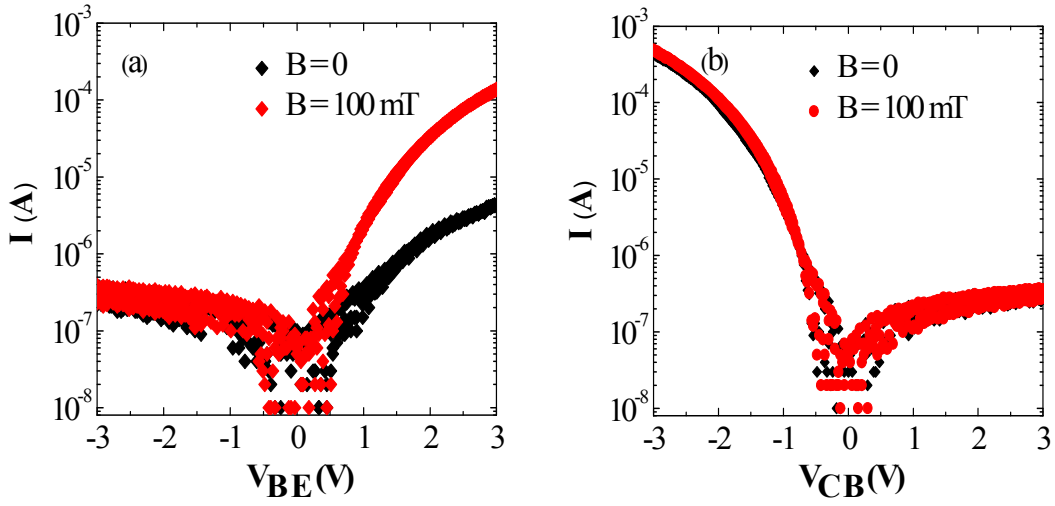


Figure 4.7 Current-voltage characteristics of n-Si/SPAN(200 nm)/$Alq_3$/Ca/Al device [35]

These observations in two-terminal characteristics led us to conclude that magnetic field has a strong influence in the device and this is the reason of high MFE value (the MFE may come from $Alq_3$). As we can see in Figure 4.7b, there is no MFE can be observed. It means that the MFE is not coming either from the collector, base or collector-base interface. But huge increment is seen from Figure 4.7a in the case where current as a function of emitter-base voltage. From this figure it can be seen that the introduction of magnetic field has resulted an abrupt change in current. According to the proposed model by Desai [23,43], the presence of magnetic field can easily influence the mobility of charge carrier and triplet exciton concentration leading to the high increment on the current in the device. By following this rational, we attributed that the high current enhancement in this device is due to the changes in carrier mobility.

**Schottky barrier height**

The dependence of Schottky barrier height as a function of the SPAN thickness was studied by means of I-V technique. Figure 4.8 shows the extracted parameters of barrier height for I-V method for at least 3 diodes with different SPAN films thicknesses.

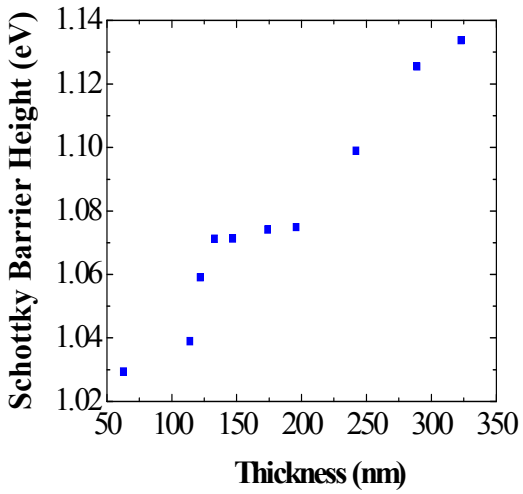


Figure 4.8 Schottky barrier heights from I-V technique

It appears that the extracted Schottky barrier height increases from 1.03 eV to 1.13 eV when the SPAN thickness increases from 63 to 323 nm, in accordance with a previous report by Silva et al. [64]. The lower Schottky barrier height of the 63 nm SPAN film may come from the imperfect formation of SPAN deduced from the irregular interface morphology. As shown, the Schottky barrier is proportional to the SPAN thickness. Note that the minimum barrier height is 1 eV for 63 nm SPAN film. Details Schottky barrier height determination is shown in Appendix.

**Thermal annealing**

Meanwhile in Figure 4.9, we present barrier heights for three different SPAN thicknesses as a function of annealing temperatures, from I-V characteristics. Thermal annealing was carried out at each desire temperature up to 200 °C in oxygen atmosphere for 10 minutes using a simple thermal annealing glass-tube where the n-Si/SPAN was placed inside the glass-tube, right in the middle. Prior to this placement, the annealing system was heated until it reached at a desire temperature. Each value is the average value for 3 diodes. It can be observed that the barrier height of the n-Si/SPAN diodes slightly decreases upon annealing at 100 °C. One can find that the barrier heights decrease as the temperature increases.

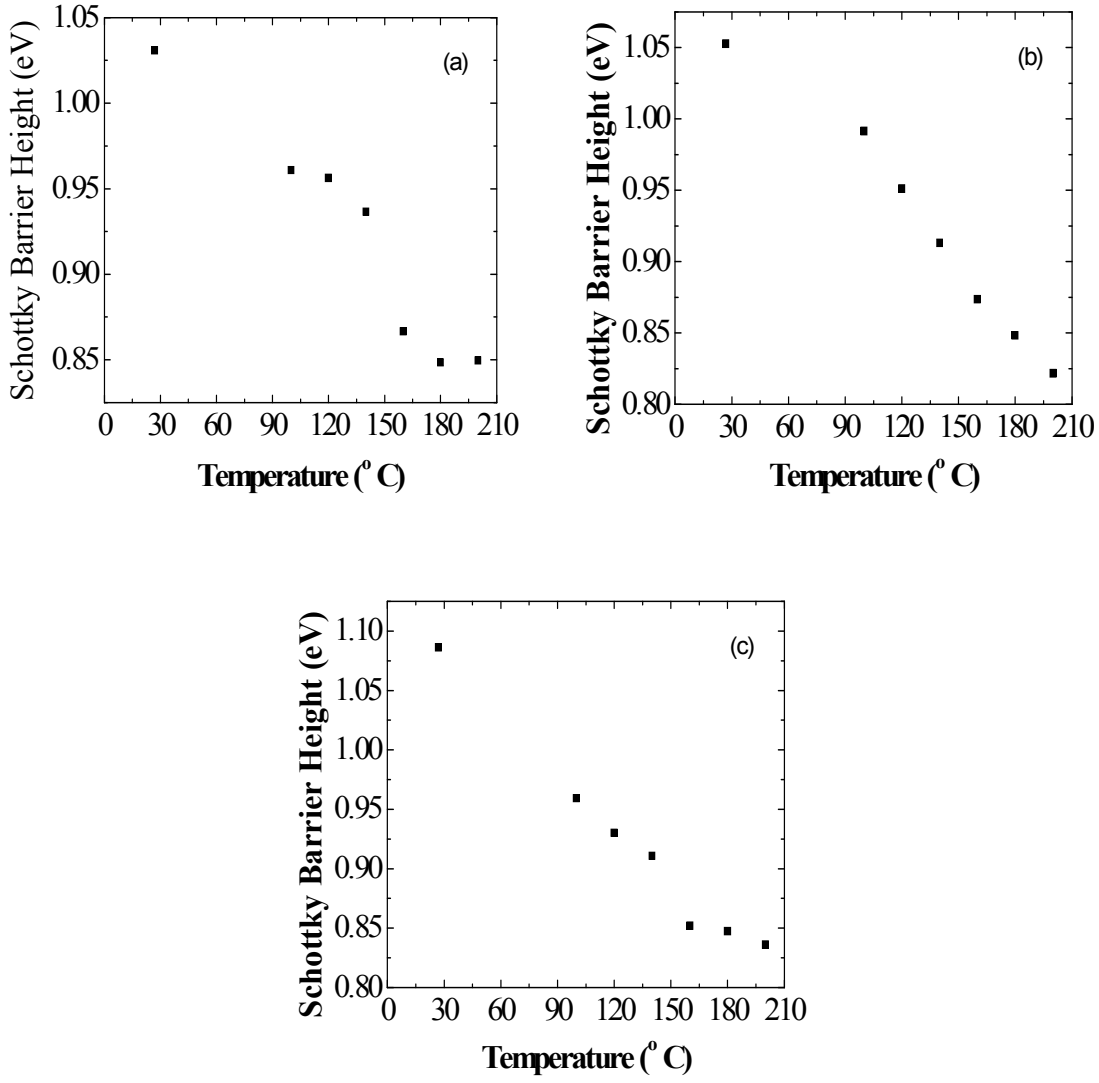


Figure 4.9 Schottky barrier heights of n-Si/SPAN on selected annealing temperatures with different thicknesses (a) 180 nm, (b) 200 nm, and (c) 220 nm

## 4.5.2 Three terminal measurements

### Common-base mode

Figure 4.10 depicts a comparison of the common-base characteristics of n-Si/SPAN/$Alq_3$/Ca/Al between two cases (with and without magnetic field). But the results for both cases show a clear evidence of transistor behavior, since small positive $V_{CB}$ ($V_{CB}$: potential difference between collector and base), a saturation of the $I_C$ is observed at values almost equal to the selected $I_E$.

It can be seen that the magnitude of saturation $I_C$ can be controlled by the $I_E$, meaning that almost all electrons injected by the emitter into the base arrive at the collector. There is a rapid increase in $I_C$ for negative $V_{CB}$ due to the forward-biased n-Si/SPAN Schottky junction and this is reason the current magnitude is high.

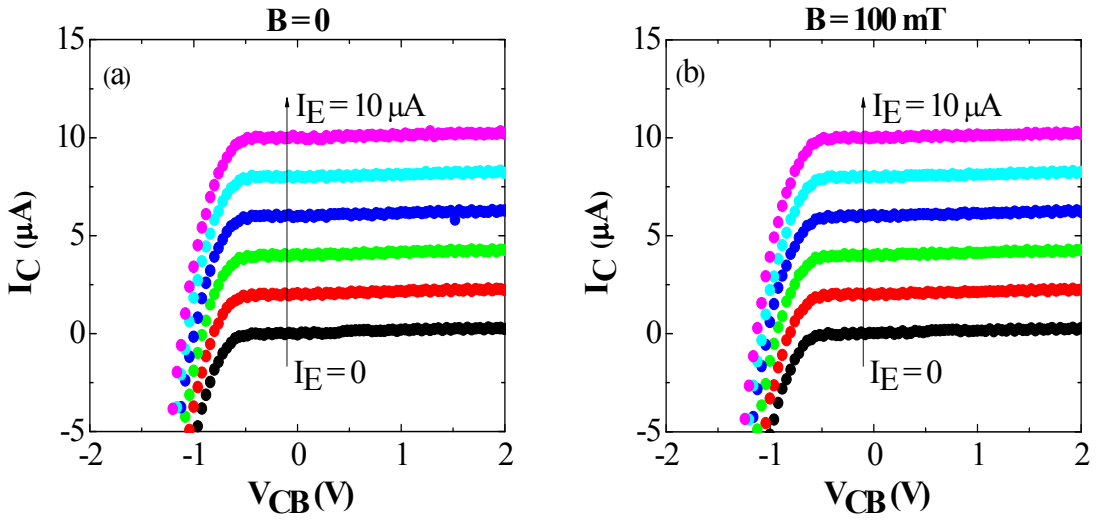


Figure 4.10 Common-base characteristics of n-Si/SPAN(200 nm)/$Alq_3$/Ca/Al device

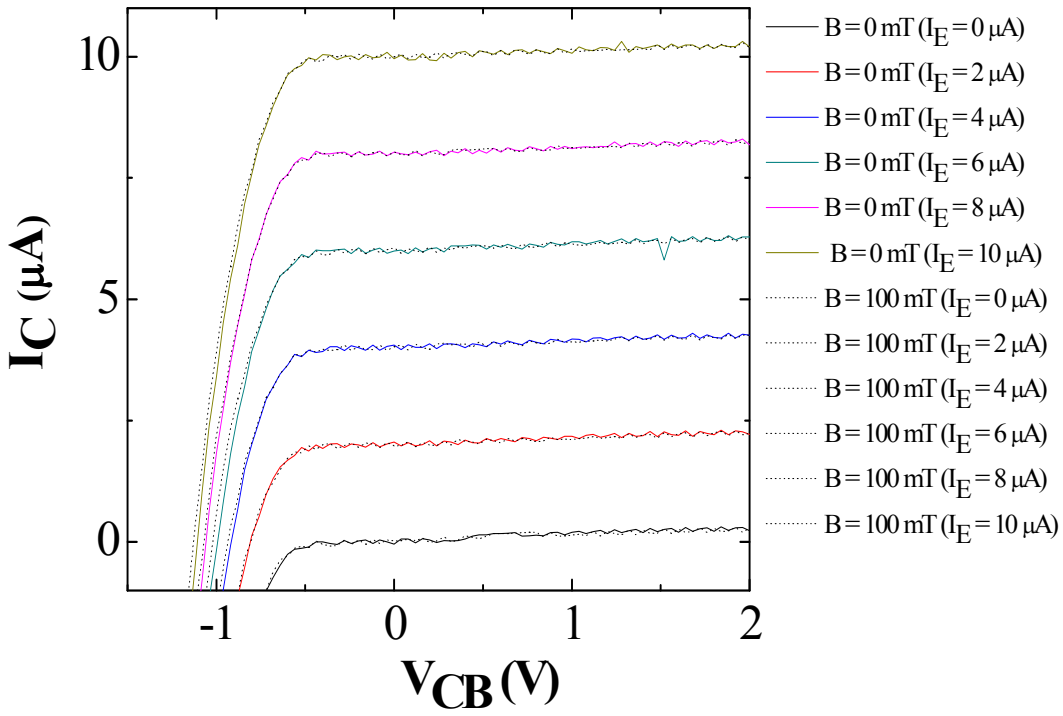


Figure 4.11 The overlapped of common-base characteristics for two different conditions (dotted line) with magnetic field, and (solid line) without magnetic field at different $I_E$

If we look deeper into this characteristic, there is a very small change in $I_C$ as we introduced the magnetic field (Figure 4.11). This trend has been reported by Gruber et. al [65] where they observed a strong different in $I_C$ as we increased the $V_{CB}$. But this might be because of the leakage current but at the negative $I_C$ and negative $V_{CB}$, there is also a small change. We attributed this small change to the displacement of Fermi level.

The plot of $I_C$ as a function of $I_E$ at a constant $V_{CB}$ that allows calculating the common-base current gain is presented in Figure 4.12. To eliminate the contribution of the leakage current, $I_L$ which is assumed to be constant, the common-base current gain, defined as $\alpha_O = dI_C / dI_E$ is calculated at $V_{CB} = 0$. In both cases, the slope $\alpha_O$ equals 0.99, which is near to the ideal common-base current gain, which equals 1, with electrons transport primarily through pinholes in the base (will be discussed in 4.7.3). This high $\alpha_O$ also indicates that the base transport factor, $\alpha_T$ in these SPAN/$Alq_3$ based PBT device is high since $\alpha_O < \alpha_T$.

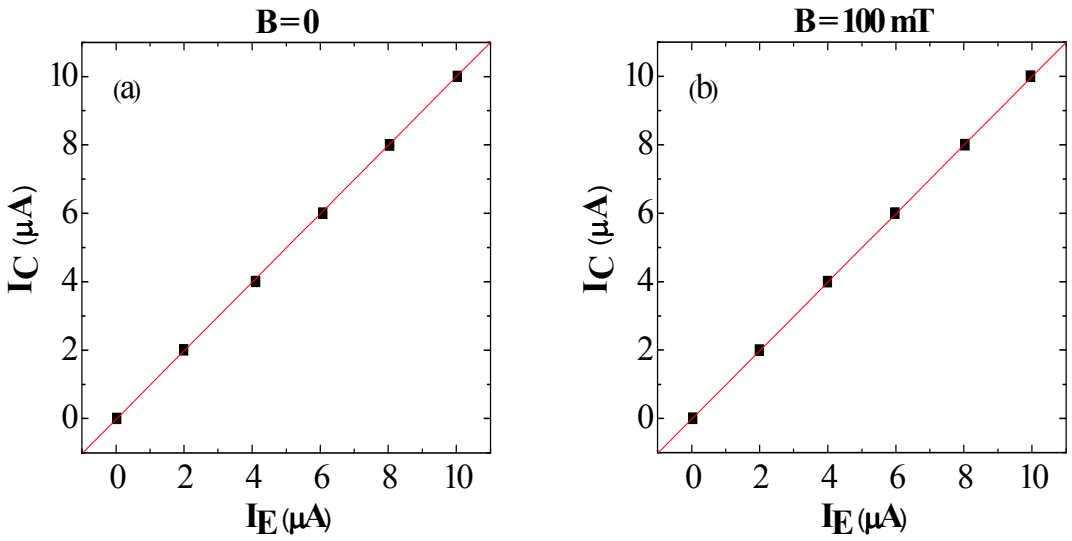


Figure 4.12 Dependence of $I_C$ on $I_E$ of n-Si/SPAN(200 nm)/$Alq_3$/Ca/Al device

One of the important characteristic of our transistor is shown in Figure 4.13. As can be clearly observed, device with and without the presence of external magnetic field, the voltage required to achieve current levels of the order of 1 mA/mm$^2$ is similar, which is lower than 1 V. This implies to low power dissipation in the emitter layer.

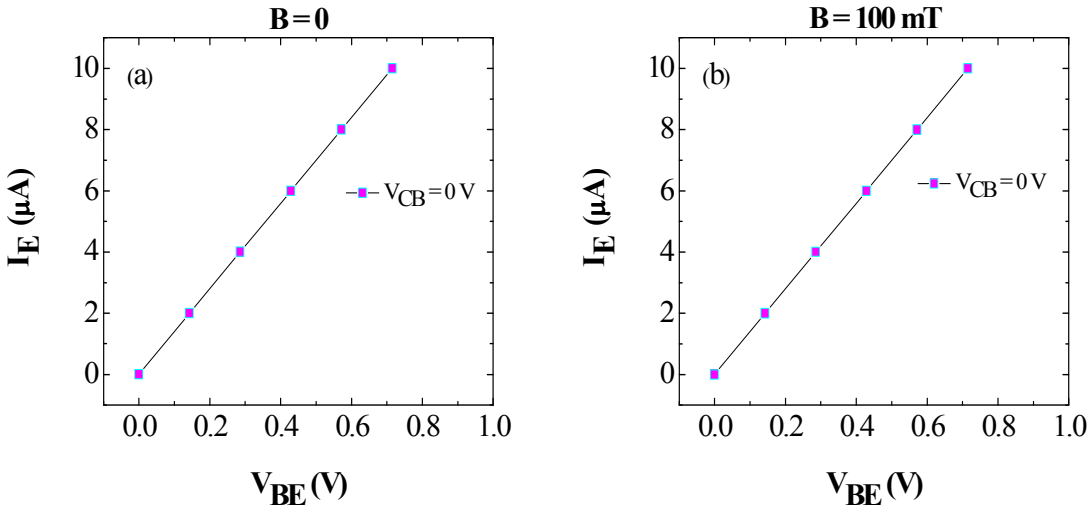


Figure 4.13 Dependence of $I_E$ as a function of $V_{BE}$ on n-Si/SPAN(200 nm)/$Alq_3$/Ca/Al

Low power dissipation becomes an important issue in designing criteria especially in the environment of portable systems where a low supply voltage, given by a single cell battery, is used. This characteristic is mainly important in case of organic and hybrid devices, because organic materials are more sensible to high temperatures than their inorganic counterparts and heat dissipation constitutes a general problem if higher integration is aimed.

n-Si/SPAN/$Alq_3$/Ca/Al device shows permeable base characteristics, since at constant $I_E$, we observe that $\partial V_{BE} / \partial V_{CB} = 1$, indicating that the base is not able to shield the emitter from electric field changes between base and collector [67], as can be seen in Figure 4.14a and b.

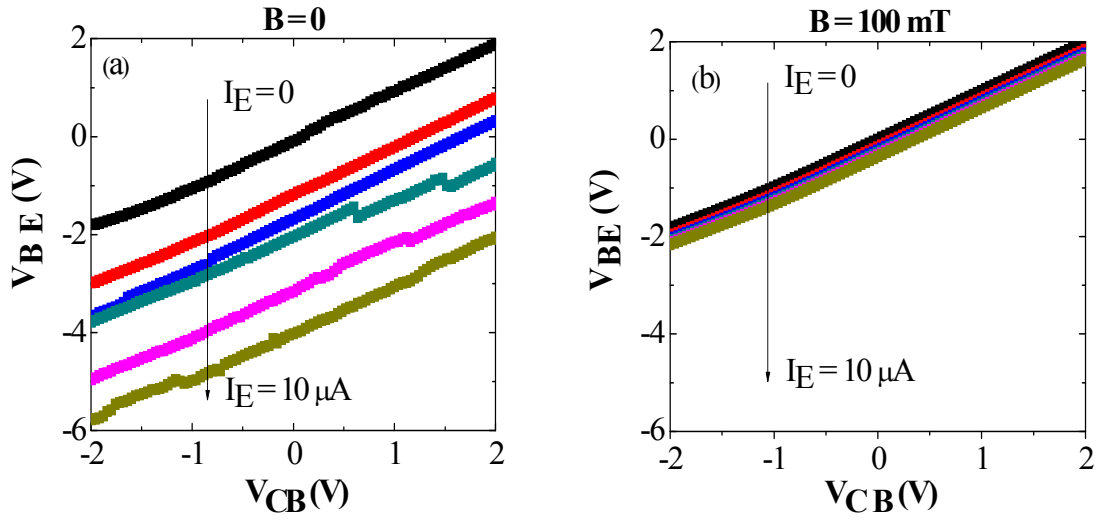


Figure 4.14 Dependence of $V_{BE}$ on $V_{CB}$, for constant $I_E$, of n-Si/SPAN(200 nm)/$Alq_3$/Ca/Al device

This characteristic is very interesting since all similar devices prepared with $C_{60}$ instead of $Alq_3$ at a constant $I_E$, show metallic-base characteristics $\partial V_{BE} / \partial V_{CB} = 0$ [66]. This indicates that the interface between emitter and base plays such a vital role in defining transistor characteristics. Permeable base characteristics are frequently observed in vertical architecture devices when metal layer of the base is very thin due to granular character of the metal film, which facilitates the existence of unintentional pinholes [67,68]. However, a very thin base tends to imply in high electrical resistance along the base film, which leads to bad device performance when operated at higher $I_B$ due to the voltage drop along the base film. Under such conditions the current density from emitter to collector is not uniform, because the base does not constitute a nearly equipotential plane, leading to higher current density near the base wiring connection region.

### Common-emitter mode

Figure 4.15 illustrates the common-emitter characteristics in the dark at room temperature under two obvious different conditions. One can see that in Figure 4.15a, there is a bad common-emitter characteristic when there is no external magnetic field applied to the device. On the other hand, it can be seen in Figure 4.15b that with the introduction of external magnetic field, the $I_C$ is significantly larger than that of the device without external magnetic field, which is also related to a remarkable increase in the common-emitter current gain, $\beta^*$ (Figure 4.16). These observations led us to conclude that the magnetic field has a strong influence on the electron transport in the $Alq_3$. In order to clarify this matter, we developed and characterized the electron-only and hole-only devices. In these two devices, it is demonstrated that there is no clear indication of MFE in these majority charge carrier transport devices (will be discussed in Unipolar Devices-Appendix).

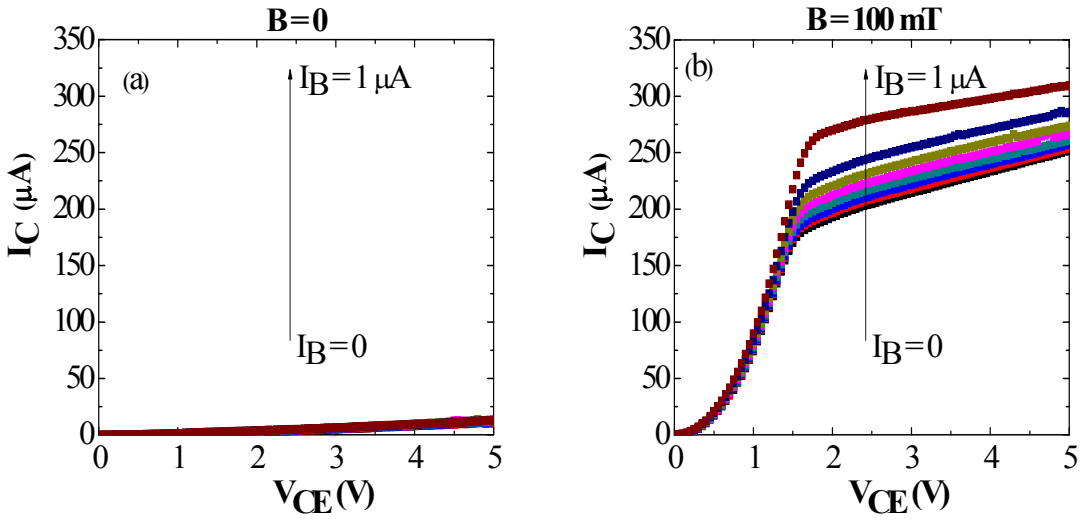


Figure 4.15 Common-emitter characteristics of n-Si/SPAN(200 nm)/$Alq_3$/Ca/Al device [65a]

As illustrated in Figure 4.15, common-emitter characteristics allow the determination of the common-emitter current gain $\beta^*$. Due to the existence of $I_C$ at $I_B = 0$, we define it as the $I_L$ and $\beta^*$ is given by the related quantity $\beta^* = \left[I_C - I_L\left(I_B = 0\right)\right] / I_B$. Without the presence of magnetic field, the $\beta^*$ is distributed between 0 and 2, with a large spread and noise (Figure 4.16a). In Figure 4.16b, in spite of a weak magnetic field, the $\beta^*$ reaches the maximum value of 8 at $V_{CE}$ = 2.0 V and $I_B$ = 0.86 μA. As seen in Figure 4.16b, this device shows high gain about 2 at $I_B$ = 0. As the $I_B$ increases, the increasing rate of $I_C$ tends to be lower, almost tending to a saturation in $I_C$ – $I_L$ and consequently, to a stabilization of $\left(I_C - I_L\right) / I_B$ at a lower level.

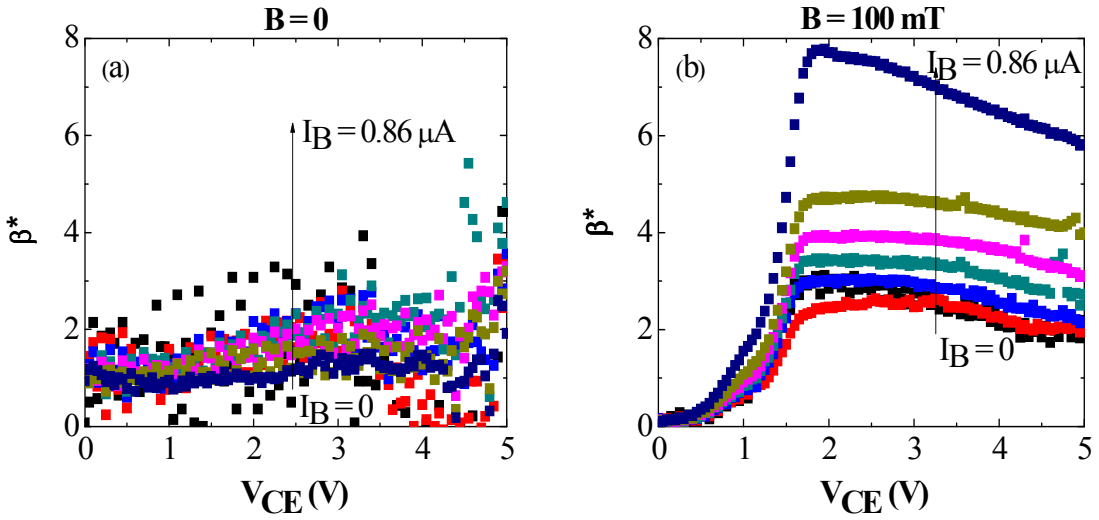


Figure 4.16 Common-emitter current gain of n-Si/SPAN(200 nm)/$Alq_3$/Ca/Al device [65a]

The charge carrier transport to or from the base, to either collector or emitter, is hindered by some kind of transport barrier, since the differential resistance $R_d = \left(\partial I / \partial V\right)^{-1}$

for transport between emitter and collector is the lowest one when the two terminal measurements are compared, as can be seen in Figure 4.10. It is consistent with the permeable base character suggesting that the potential barrier for charge transfer from emitter to collector is much lower than the potential barrier between emitter and base. Additionally, when the charge carrier transport is from the base or to the base, the current must be transported along the film up to the base terminal connection, implying the inclusion of a series resistance.

In Figure 4.17, we plot the ratio $I_C/I_E$, which corresponds to the maximum possible ratio of majority to total (majority plus minority) charge carrier contribution in the current through the $Alq_3$, as a function of $V_{CE}$ for three different values of $I_B$, at $B = 0$ (Figure 4.17a) and $B$ = 100 mT (Figure 4.17b). If the $I_C/I_E$ ratio is taken at $V_{CE} > V_{BE}$, one can see that $I_C/I_E \cong 1$.

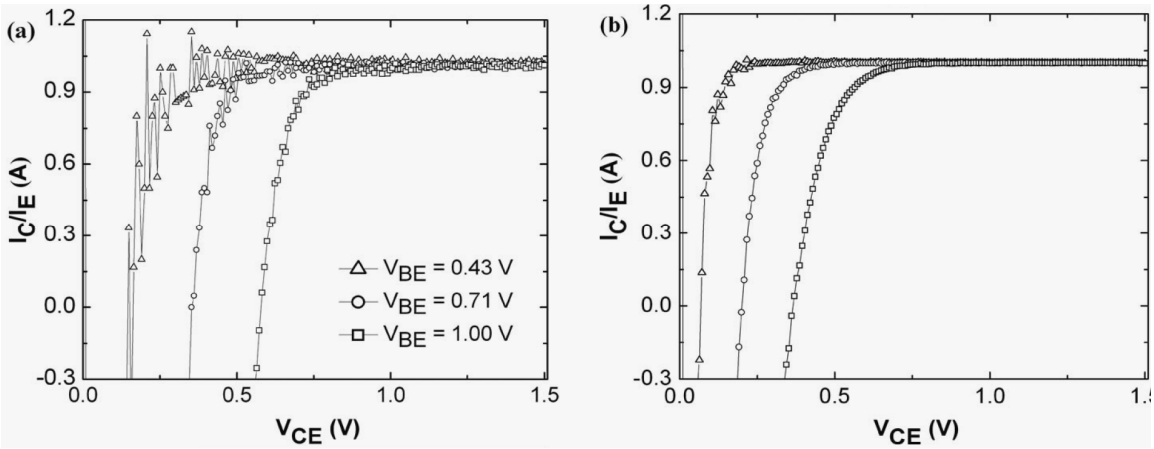


Figure 4.17 $I_C/I_E$ ratio as a function of collector voltage in common-emitter mode measurements for $V_{BE}$ = 0.43, 0.71 and 1.00 μA at (a) $B = 0$ and (b) $B = 100$ mT [65a]

## 4.6 SPAN/$Alq_3$/$C_{60}$ Heterostructure

### 4.6.1 Device structure (double emitter layer)

In this device, we performed a detailed and comprehensive study on the SPAN thin films used as the base terminal in our fabricated devices. It is demonstrated that the introduction of ultrathin $V_2O_5$ between the top electrode, Al and the emitter, $Alq_3$/$C_{60}$ indicating a significant improvement in device performance. Essentially, we have found a correlation between current gain, opening voids and MFE in PBT. A schematic illustration of n-Si/SPAN(153 nm)/$Alq_3$(60 nm)/$C_{60}$(60 nm)/$V_2O_5$(5 nm)/Al(100 nm) is shown in Figure 4.18.

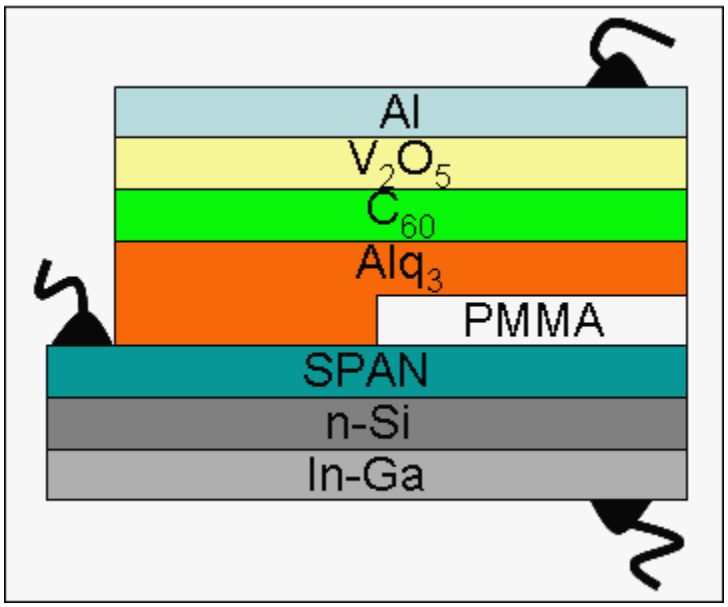


Figure 4.18 Schematic diagram of the proposed PBT layers sequence

### 4.6.2 Energy diagram

The energy level diagram of the n-Si/SPAN/$Alq_3$/$C_{60}$/$V_2O_5$/Al device is schematically presented in Figure 4.19. A good Schottky contact of SPAN and n-Si is desirable for an asymmetrical PBT device to achieve high current gain, guarantee the $Alq_3$/$C_{60}$ based PBT to well operate at the common-base and common-emitter modes.

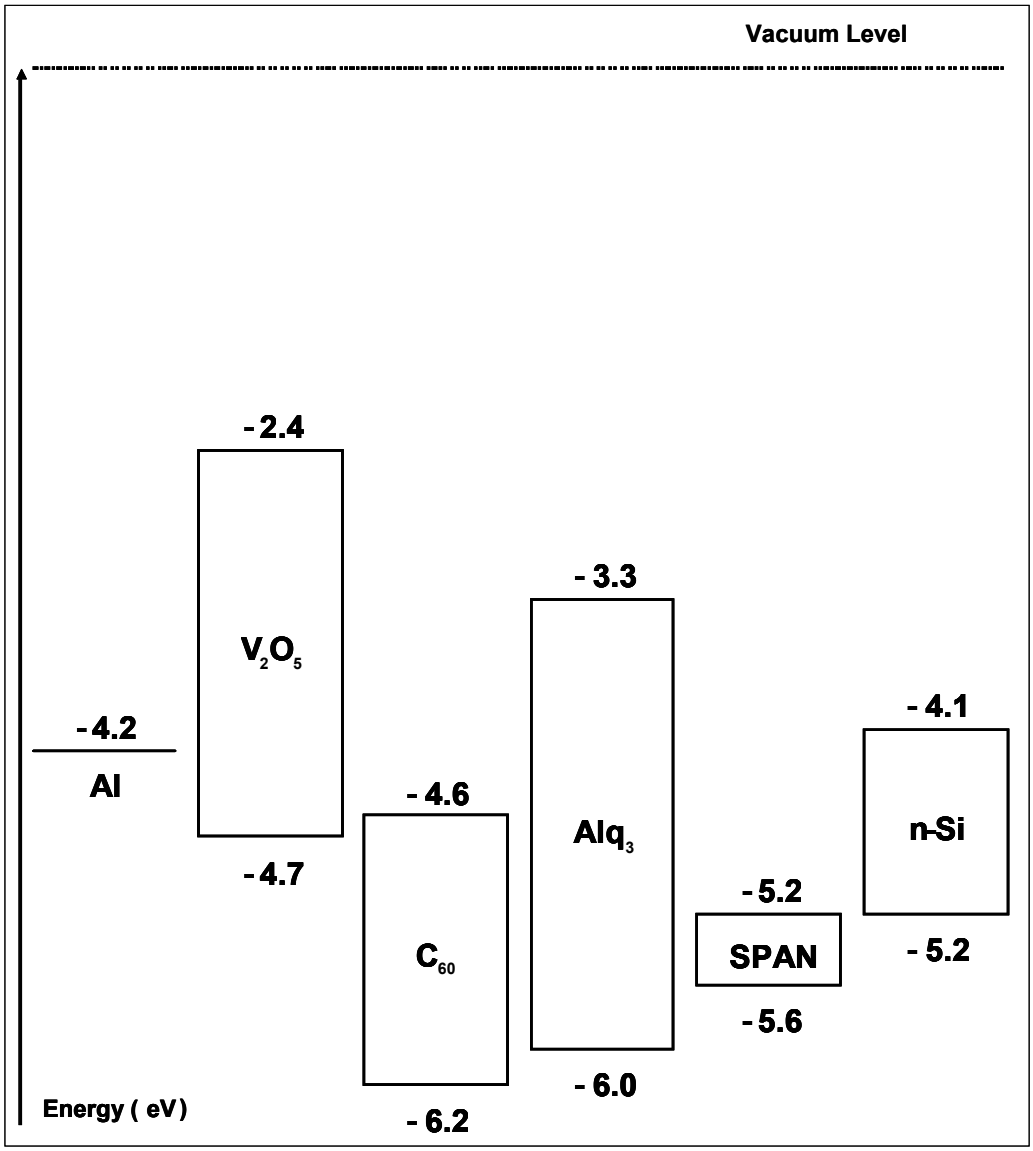


Figure 4.19 The energy level diagram of the n-Si/SPAN(153 nm)/$Alq_3$/$C_{60}$/$V_2O_5$/Al

The presence of the $Alq_3$ implies that majority charge carriers arrive at the base region with energy, and also increases the injection of the holes (minority charge carriers) from SPAN to the $Alq_3$, when compared to the case of $C_{60}$. This is due to a slightly lower energy barrier of 0.4 eV between SPAN and $Alq_3$, compared to the 0.6 eV barrier between SPAN and $C_{60}$, and indeed in an agreement with our earlier hypothesis that the higher the HOMO level of the base layer, the higher the chances of probability holes being injected to the emitter. Hence, the recombination current in the emitter is further decreased. The small energy barrier for electrons at the $Alq_3/C_{60}$ does not impose constraints to transport, despite producing some charge accumulation and redistribution of the electric field inside the $Alq_3/C_{60}$ layer. A deep understanding of the organic junction will be helpful for further developing high performance PBT.

## 4.7 Results and Discussion

### 4.7.1 Two terminal measurements

In Figure 4.20, we illustrate the I–V characteristics in the semi-logarithmic scale, under the absence of magnetic field and under the presence of magnetic field = 100 mT. From Figure 4.20a, there is a very small increment in emitter current, $I_E$ due to the influence of magnetic field. As expected, $V_{BE} < 0$ there is no obvious change in the current, meaning that with the presence of magnetic field, one can easily observe such an increment in the device current rectification. To obtain some clues about the influence of magnetic field on the device, it was further examined via the same form of measurement. In this measurement, we used the SPAN film and In-Ga terminals (Figure 4.20b) and indeed this type of measurement is in accord with the previous observed behavior where there is no MFE. To

further investigate the influence of magnetic field, we also carried out a simple test of the dependence of MFE on magnetic field orientation and yet again in agreement with MFE results reported by other groups.

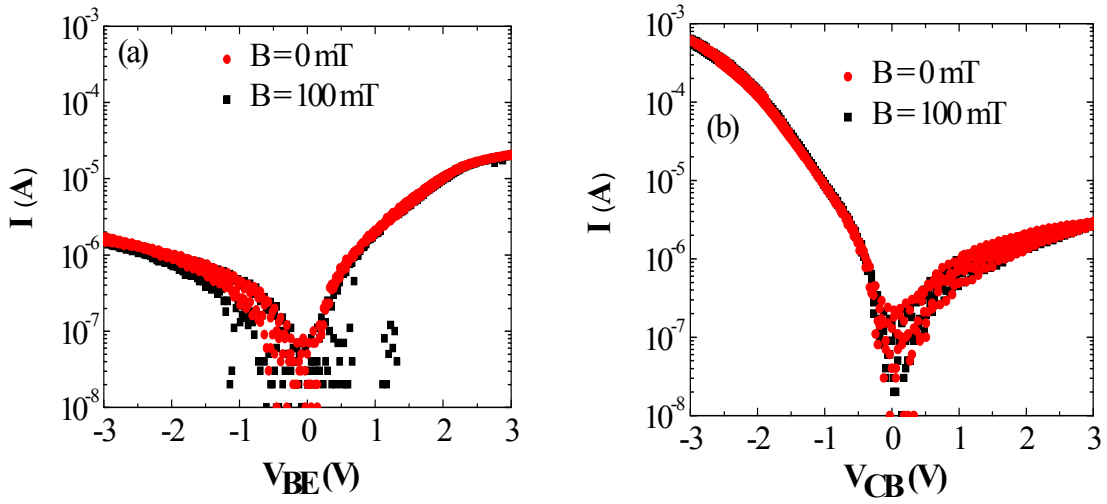


Figure 4.20 Two terminal current-voltage characteristics of n-Si/SPAN(153 nm)/$Alq_3$/$C_{60}$/$V_2O_5$/Al device

## 4.7.2 Three terminal measurements

Figure 4.21 shows family curves of common-base current-voltage characteristics of n-Si/SPAN/$Alq_3$/$C_{60}$/$V_2O_5$/Al. These figures also provide clear evidence of bipolar transistor behavior, since small positive $V_{CB}$ ($V_{CB}$: potential difference between collector and base), a saturation of the $I_C$ is observed at values almost equal to the selected $I_E$. Notice that, when the $I_E$ = 0, the $I_C$ is not equal to zero. This is due to the current attributed to thermal holes and electrons crossing the BC junction in the reverse direction. It can also be seen that the magnitude of saturation $I_C$ can be controlled by the $I_E$ in which the $I_C$ increases with $I_E$. Apparently the n-Si/SPAN/$Alq_3$/$C_{60}$/$V_2O_5$/Al device exhibits sharp turn-on behavior and

rapid increase in $I_C$ for negative $V_{CB}$. That is, under forward-biased n-Si/SPAN Schottky junction, assuming the SPAN layer is thinner than the mean free path of the carrier, almost all electrons injected by the emitter get into the base arrive at the collector and for this reason the current magnitude is high.

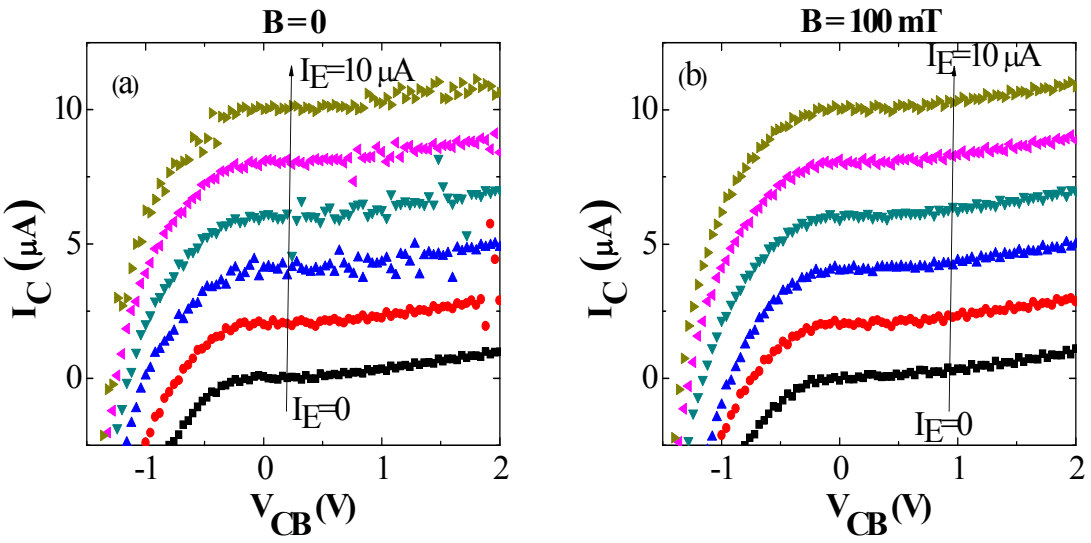


Figure 4.21 Common-base characteristics of n-Si/SPAN(153 nm)/$Alq_3$/$C_{60}$/$V_2O_5$/Al device

Since the $I_E$ is constant (to allow better determination of $\alpha_T$), it is hard to observe the different between these studied cases. There are small changes in $I_C$ in these two different cases (Figure 4.22) as reported by Gruber et. al [65]. From the Figure 4.22, the solid line (thick) and thin line are with and without magnetic field is applied to the device, respectively can be used to observe this changes. We can see that there is a slight difference between the case with and without magnetic field especially at negative IC and negative VCB where the base/collector junction is in the forward biased condition. These small changes may be due to the changes in Fermi level pinning in the device.

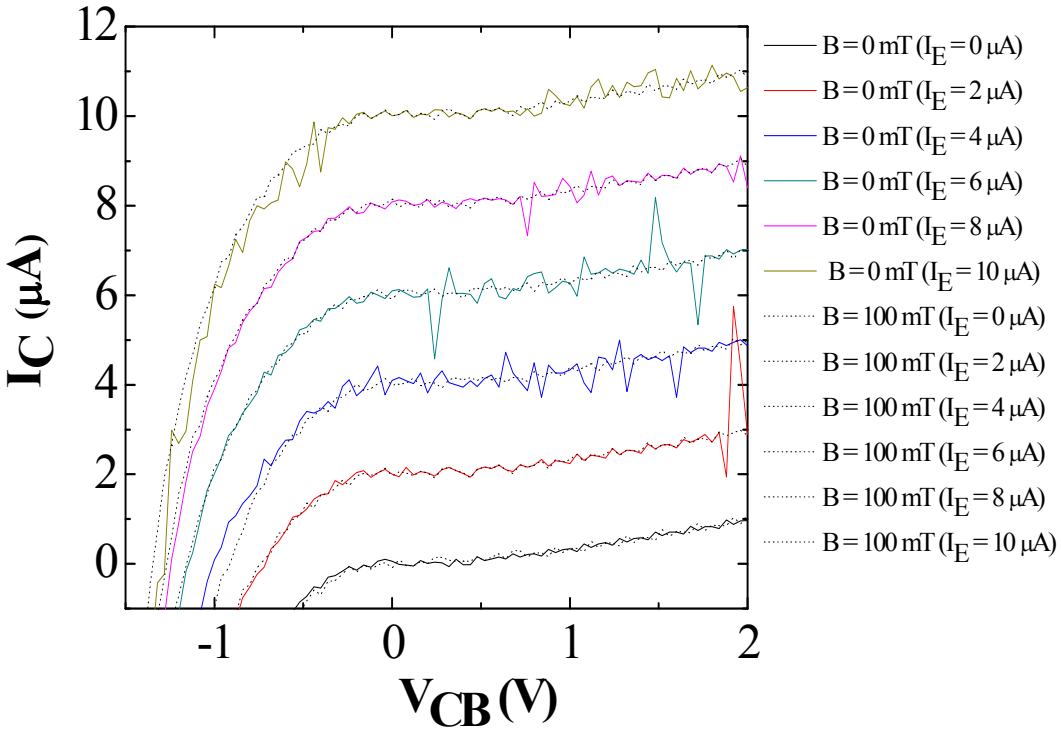


Figure 4.22 The overlapped of common-base characteristics for two different conditions (dotted line) with magnetic field, and (solid line) without magnetic field at different $I_E$

Figure 4.23 presents the plot of $I_C$ as a function of $I_E$ at $V_{CB}$ = 0. For the determination of $\alpha_O$, the contribution of $I_L$ must be eliminated. From this figure, either with the presence or without the presence of applied magnetic field (Figure 4.23a and b), the slope $\alpha_O$ equals 0.99. This nearly unity gradient corresponds to the electron transport from emitter to the base through pinholes is at the optimal condition. This value is indeed in a good agreement to the ideal $\alpha_O$, which equals 1. The obtained result indicates that the base transport factor, $\alpha_T$ in these SPAN/$Alq_3$ based PBT devices is high.

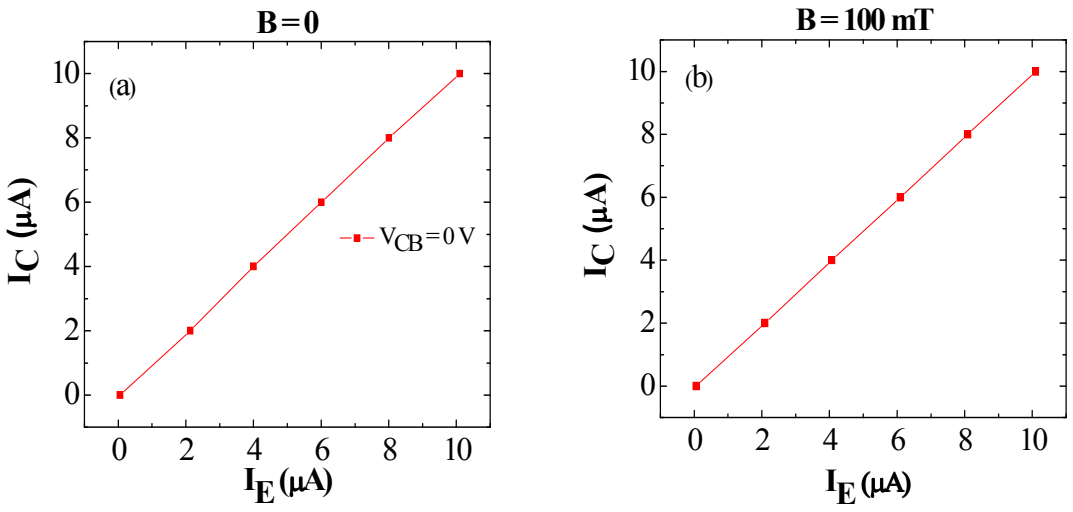


Figure 4.23 Dependence of $I_C$ on $I_E$ of n-Si/SPAN/$Alq_3$(153 nm)/$C_{60}$/$V_2O_5$/Al device at constant $V_{CB}$ = 0 V

Our studied device (n-Si/SPAN/$Alq_3$/$C_{60}$/$V_2O_5$/Al) shows permeable base characteristics. This is due to the observation in Figure 4.24 that $\partial V_{BE} / \partial V_{CB} = 1$ at a constant $I_E$ from 0 to 10 μA at 2 μA per step. This relation essentially indicates that the base is not able to shield the emitter from electric field changes between base and collector [67]. The interface between emitter and base is important in defining the transistor characteristics. This is because comparable devices prepared with $C_{60}$ instead of $Alq_3$, show metallic-base characteristics [64].

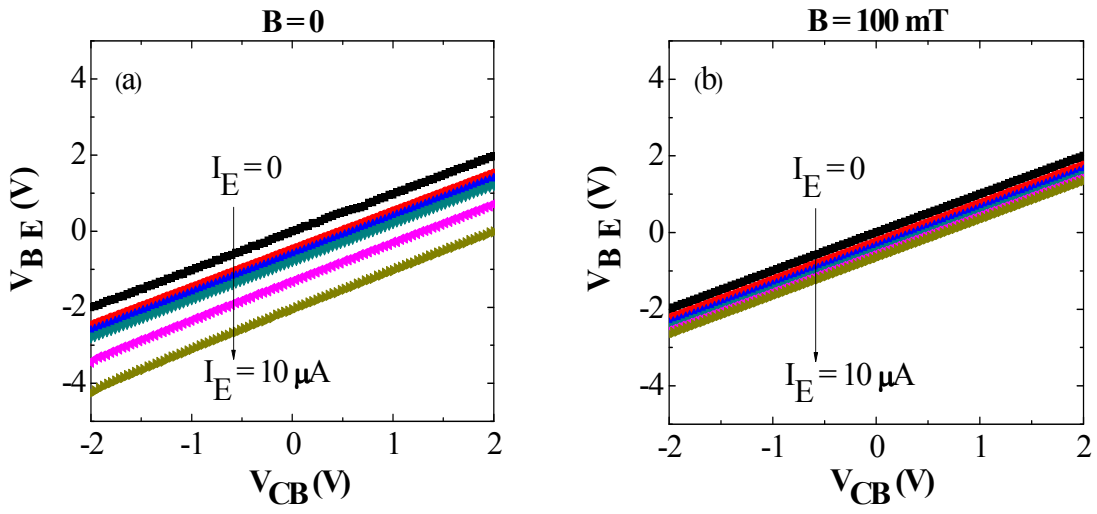


Figure 4.24 $V_{BE}$ as a function of $V_{CB}$ at a constant $I_E$ for n-Si/SPAN(153 nm)/$Alq_3$/$C_{60}V_2O_5$/Al device, measured at room temperature in the darkness

The common-emitter characteristics of an n-Si/SPAN/$Alq_3$/$C_{60}$/$V_2O_5$/Al device are shown in Figure 4.25, allowing the determination of the $\beta^*$ (see Figure 4.26). Curves are measured in steps of 0.14 μA/step starting with zero $I_B$. The results show a variation in $I_C$ as a function of magnetic field indicating that the transistor behaves as magnetically tunable device with a field dependent gain. As can be seen the studied device can be operated under wide $I_C$ regime.

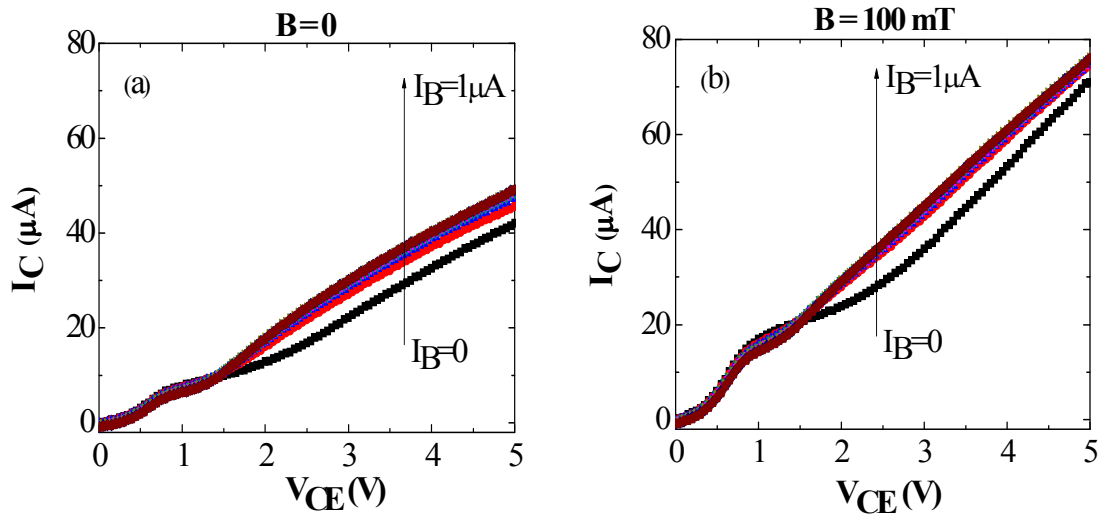


Figure 4.25 Common-emitter I–V characteristics for n-Si/SPAN(153 nm)/$Alq_3$/$C_{60}$/$V_2O_5$/Al with an emitter area of 1 $mm^2$, measured at 25 °C

In Figure 4.26, we present a plot of $(I_C - I_L)/I_B$ as a function of $V_{CE}$. It can be clearly seen that these devices show high gain for low $I_B$, but as $I_B$ increases the increasing rate of $I_C$ tends to be lower, almost tending to a saturation in $I_C - I_L$ and consequently, to a stabilization of $(I_C - I_L)/I_B$ at a lower level. Experimentally, in both figures, the studied device exhibits $\beta^*$ greater than unity even at $I_C = 0$. Indeed the $\beta^*$ of an n-Si/SPAN/$Alq_3$/$C_{60}$/$V_2O_5$/Al is 36 $V_{CE}$ = 3.0 V and $I_B$ = 0.86 μA.

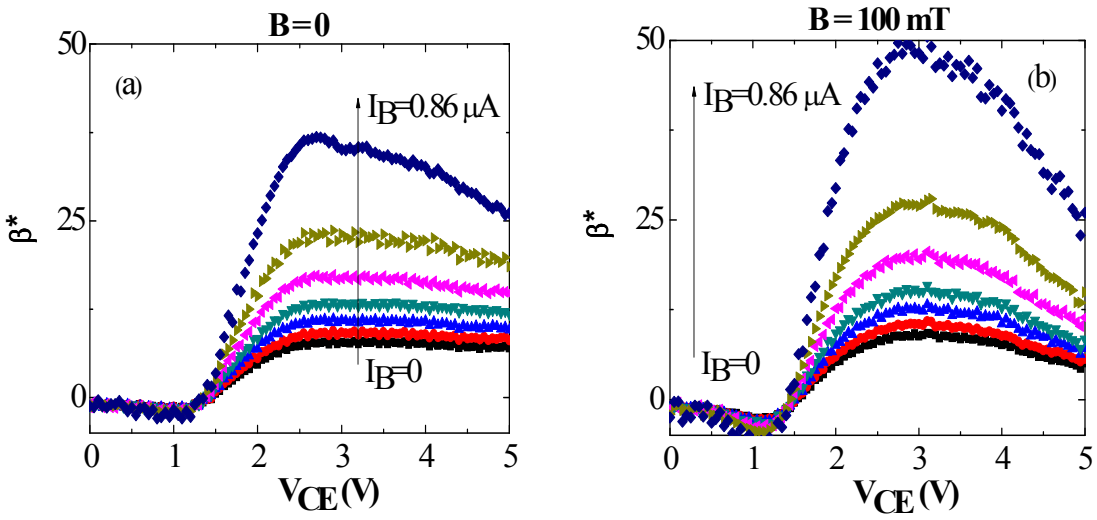


Figure 4.26 Common-emitter current gain characteristics for n-Si/SPAN(153 nm)/$Alq_3$/$C_{60}$/$V_2O_5$/Al with an emitter area of 1 $mm^2$, measured at 25 °C

A change in the transistor $\beta^*$ is observed in the presence of an external magnetic field. The change in $\beta^*$ upon introduction of external magnetic field, is calculated as follows:

$$\delta\beta^* = \left( \beta^*(B) - \beta^*(0) \Big/ \beta^*(0) \right) \times 100$$

where the term $\beta^*(B)$ is the current gain at a magnetic field of and a bias $V_{CE}$ and $\beta^*(0)$ is the zero magnetic field current gain at the same bias. The magnetoamplification, $\delta\beta$ is calculated for a constant $V_{CE}$ for a given $I_B$. To the best of our knowledge, $\beta^*$ = 36 is the highest value attained for SPAN-based organic transistor without the presence magnetic field. As compared with other device structure in this thesis, the value of $\beta^*$ is the highest for the case without the presence of magnetic field. The maximum variation of the average $\beta^*$ was 38.9 % measured at 100 mT, $V_{CE}$ = 2.75 V and $I_B$ = 0.86 μA. However the $\beta^*$ reaches

approximately 50 at $V_{CE}$ = 2.85 V and $I_B$ = 0.86 μA with the presence of magnetic field and it is due to the electrons that arrived at the collector; injected and transported from the emitter through the base layer. As we also observed for $I_B$ from 0.14 to 0.71 μA, $\beta^*$ decreases slowly and becomes almost constant between 3 and 5 V, which may be due to a change in the ratio of the minority carrier contribution. This observation is again in agreement with our earliest results [12] that the magnetic field has a significant influence in the device. The presence of high $\beta^* > 1$ at low current region is mainly attributed to the high base quality. This is certainly suitable for a low-voltage and a low-power circuit application.

### 4.7.3 Dependence of $\alpha_O$ and $\beta^*$ on SPAN thickness

$\beta^*$ is an important figure of merit for a transistor. For organic transistor, the $\beta^*$ is limited by its emitter injection efficiency, which is a measure of the injected majority-carrier current compared to the total $I_E$. Thus, for high $\beta^*$ in organic transistor, one should either increase the injected majority-carrier current (i.e., by doping the emitter much more heavily than the base), or reduce the back-injected minority-carrier current by creating a potential barrier to minimize the back injection of minority carriers. However, the organic transistor possesses many potential advantages such as a simple device structure and mature fabrication and growth techniques. One could achieve adequate gain despite using a highly doped base.

In this device, we observed a small decay in $\alpha_O$ and a large increment in $\beta^*$ as we changed the SPAN film thickness (from thin to thick film). Thus in order to get a full

understanding and a real picture of these dependencies, we developed a new set of devices and characterized them by means of AFM and Optical Microscopy. A complete study of the n-Si/SPAN(X nm)/$C_{60}$(60 nm)/$Alq_3$(60 nm)/$V_2O_5$(5 nm)/Al(100 nm) device was conducted where the SPAN layer thickness (X nm) has been changed, ranging from 63 to 234 nm, and we have found that crucial characteristics (common base characteristics) of the device remain unchanged.

**Optical microscopy images**

To further investigate the mechanism responsible for the reduction of $\alpha_O$ and increment $\beta^*$ values with increasing SPAN thickness, SPAN film images by Optical Microscopy for the samples with 61 and 156 nm thick SPAN films deposited onto the n-Si are illustrated in Figure 3.4. Figure 3.4 shows the surface morphology of SPAN films grown via chemically deposited at room temperature and at the rate of 1.5 nm/h. A rough, uneven and with big opening voids distributed irregularly over the surface of the film can be seen in Figure 3.4a (circle regions) while in Figure 3.4b, a smooth surface image was found to be well covered to the substrate surface, with less opening voids observed.

**Atomic force microscope images**

We chose AFM to characterize and analyze the surface morphology of SPAN thin films. With its high-resolution, AFM allows the study of the thin films deposited by chemical methods. AFM has the advantage over many microscopic methods that the measurements can be come out at both solution/solid and gas/solid interfaces. By operating AFM in the

so-called tapping mode (TM-AFM) or intermittent mode (IC-AFM) damages caused by lateral shear forces can be largely excluded. An AFM image (Figure 3.5a) shows that the surface is composed of regular features with a root mean square (RMS) surface roughness estimated in 5.2 nm. The AFM image of SPAN film is shown for comparison in Figure 3.5b. The roughness of both films, obtained from the AFM measurement in the region with no opening voids, are about 79 and 30 nm, respectively and the size of opening voids was approximately 10-20 nm. Since the thickness difference between these two samples is 95 nm, the diffusion current reduction should result in such a slim reduction of $\alpha_O$ value from 0.996 to 0.977, indeed in agreement with our earlier hypothesis (Optical Microscopy) that the reduction of $\alpha_O$ is accompanied with the reduction of opening voids as the base thickness increases.

Therefore, assuming that most of the $I_C$ flows through the opening voids instead of diffusing through the SPAN film, the $\alpha_O$ value reduction should be attributed to the decrease of big opening voids with increasing of the SPAN thickness. Another possible explanation for the decrement in $\alpha_O$ may be ascribed to the enhancement of the potential barrier for electron injection. The high $\beta^*$ may be due the fact that the larger base thickness will introduce more base recombination and at the same time the reduction of $\beta^*$ with increasing thickness (after an optimized SPAN thickness) is attributed to a possible increase in the hole current back injected into the emitter. Under this assumption, role of the opening voids at the SPAN film would be similar to the grip structure in the static induction transistors (SITs) [69]. The major difference is that the size of the grid structure in SITs is limited by the metal masks. The optimized linewidth is usually of several tens of

micrometers. In Figure 4.27, we present the values of $\beta^*$ and $\alpha_O$ as a function of SPAN layer thicknesses. It is interesting to see that magnetic field has a big influence on the $\beta^*$. The $\beta^*$ changes abruptly in a device with 156 nm of SPAN (Figure 4.27). It suffers a dramatic drop to 16 at $V_{CE}$ = 3.0 V and $I_B$ = 1 μA when the SPAN thickness is increased to 175 nm. It is worth emphasizing that all devices show similar $V_{BE}(V_{CB})$ characteristics at constant $I_E$ and $I_C(I_E)$ at different $V_{CB}$ values, which indicates that all of them operate as PBT, although with thicker base. We could also easily observe that $\alpha_O$ decreases exponentially with SPAN base thickness and reached 0.953 at 234 nm of SPAN. As $\alpha_O$ is also one of the important indexes to evaluate the performance of organic transistor, which leads to the conclusion that $\alpha_O$ is considerably affected by the interface at the n-Si/SPAN. This phenomenon is attributed to a decreasing number of opening voids as the base layer thickness increases.

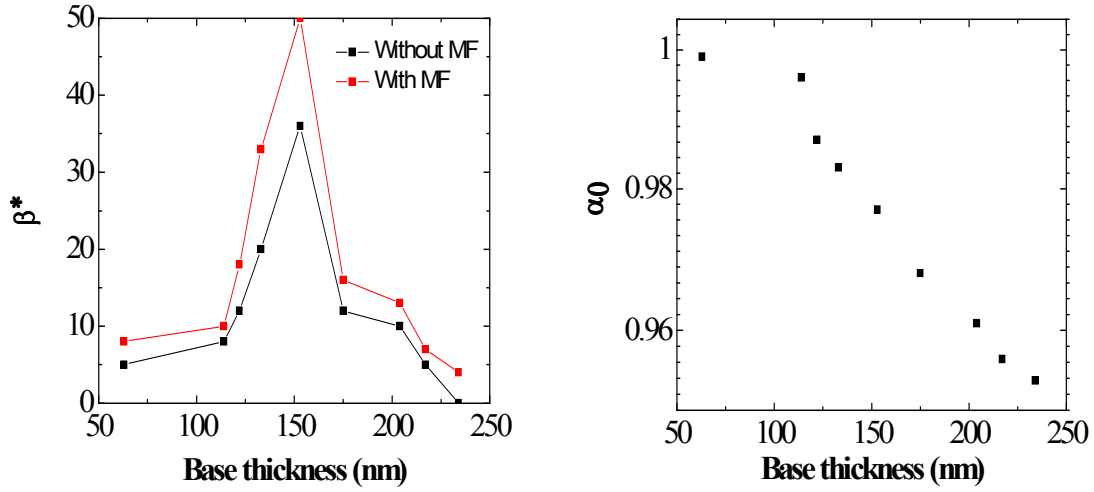


Figure 4.27 Common-emitter current gain, $\beta^*$ and common-base current gain, $\alpha_O$ for n-Si/SPAN(153 nm)/$Alq_3$/$C_{60}$/$V_2O_5$/Al devices, at $V_{CE}$ = 3.0 V, $I_B$ = 1 μA and at $V_{CB}$ = 0 V, respectively

## 4.8 SPAN/$C_{60}$/$Alq_3$ Heterostructure

### 4.8.1 Device structure (double emitter layer)

For structuring and contacting the double emitter layers transistor, a thick insulating PMMA layer was brought onto a part of the coated substrate by immersion of the substrate in the saturated solution. Before the immersion process, SPAN film was annealed for 60 min at 50 °C. $C_{60}$ was evaporated on the SPAN-coated substrate. 5 nm ultrathin layer of $V_2O_5$ was evaporated as electron injecting material and finally, a 100 nm thick Al layer was evaporated on top of the organic layers (Figure 4.28).

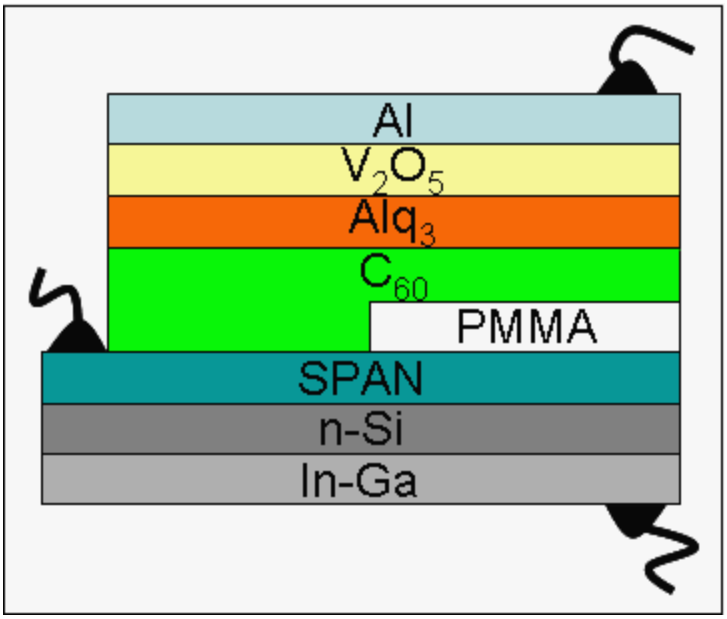


Figure 4.28 Layer stack of a double emitter layer transistor studied in this work

### 4.8.2 Energy diagram

The energy band profile of the PBT in an unbiased condition is shown in Figure 4.29. The hot carrier in this device is the electron and to elucidate the picture of electron, all energy levels are shown. The work function of Al is 4.2 eV and the HOMO and LUMO of n-Si, SPAN, $C_{60}$, $Alq_3$ and $V_2O_5$, are 4.1 and 5.2, respectively.

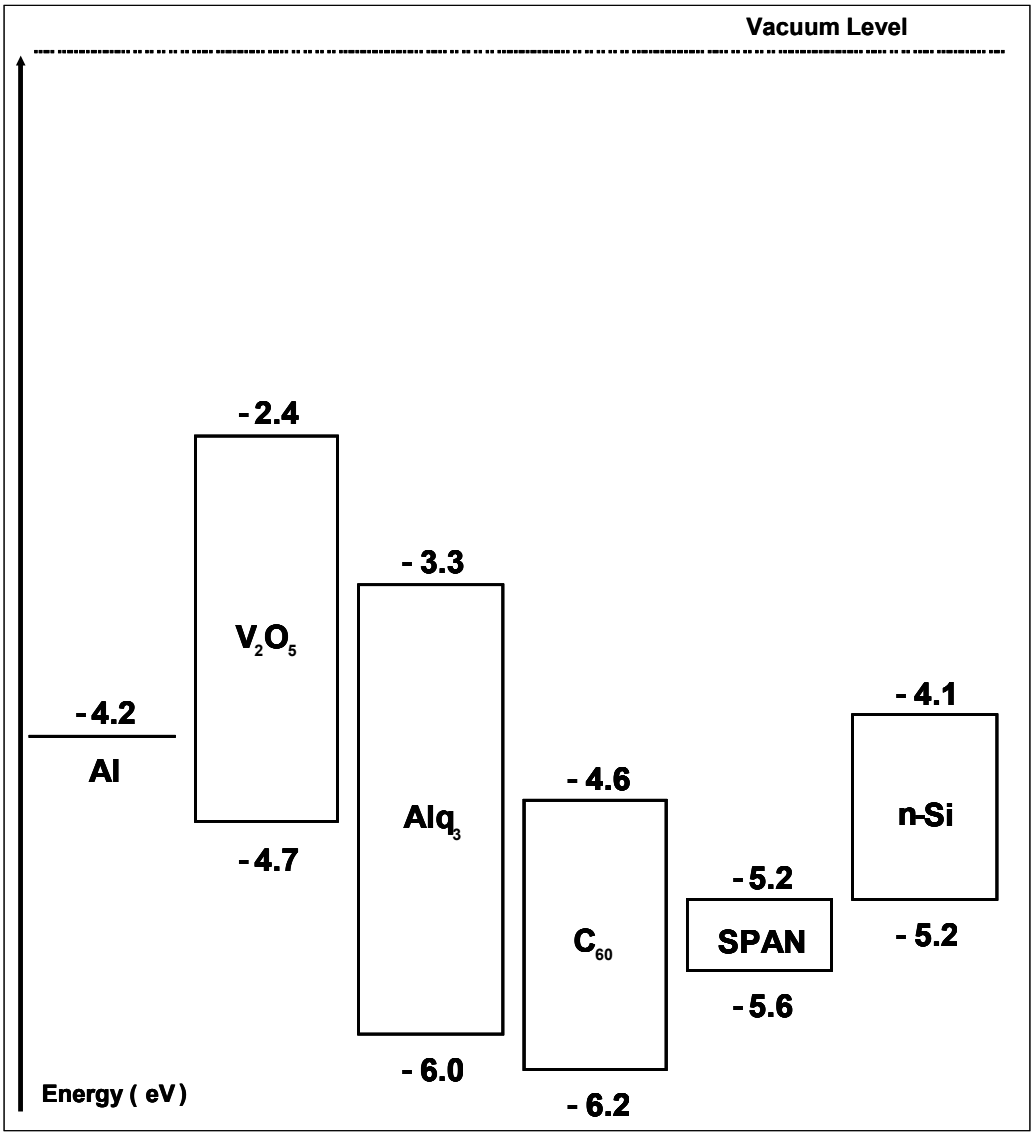


Figure 4.29 Schematic representation of the energy band diagram of n-Si/SPAN(175 nm)/$C_{60}$/$Alq_3$/$V_2O_5$/Al device

## 4.9 Results and Discussion

### 4.9.1 Two terminal measurements

As shown in Figure 4.30, we display a comparative study of I–V characteristics in the semi-logarithmic scale, under the absence of magnetic field, *B* and under the presence of *B* = 100 mT. In Figure 4.30a, it is hard to distinguish between the measurements made at 0 and 100 mT. In $V_{BE} < 0$ there is no obvious change in the $I_E$, hence that with the presence of magnetic field, one can simply observe such a slight increment in the device current rectification.

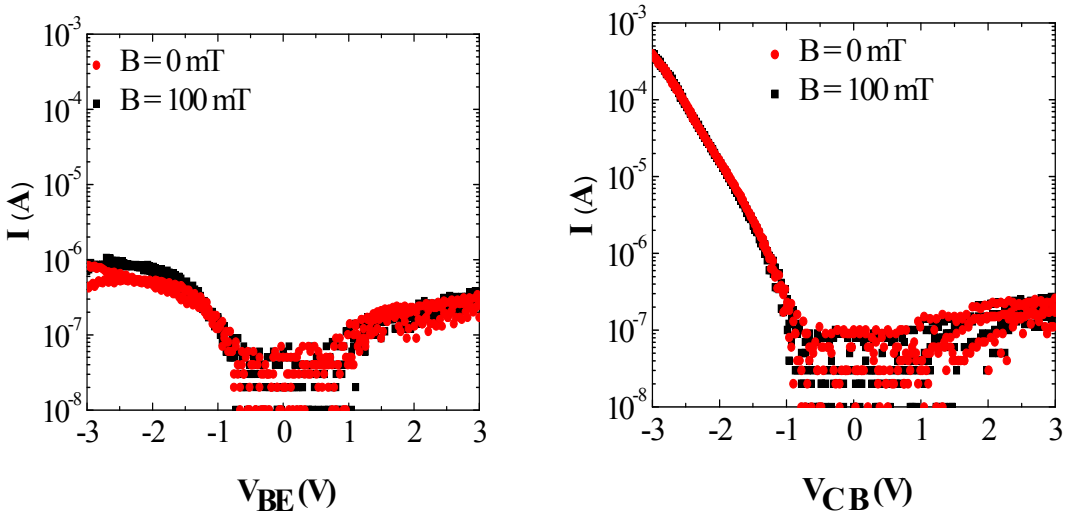


Figure 4.30 Two terminal current-voltage characteristics of n-Si/SPAN(175 nm)/$C_{60}$/$Alq_3$/$V_2O_5$/Al device

The same type of measurement using the SPAN film and In-Ga terminals (Figure 4.30b) was conducted and we were not able to observe any MFE effects. Reverse $I_L$ was less than 1 x $10^{-3}$ A at the BC applied bias of -3 V, indicating a relatively small breakdown voltage in the device operation.

### 4.9.2 Three terminal measurements

Figure 4.31 shows the CB I–V characteristics of the PBT with $V_{CB}$ ranging from -2 V to 2 V at a step of 1 V. As seen from the line at $I_E$ = 0 A, the breakdown voltage, $BV_{CBO}$ is more than 2 V.

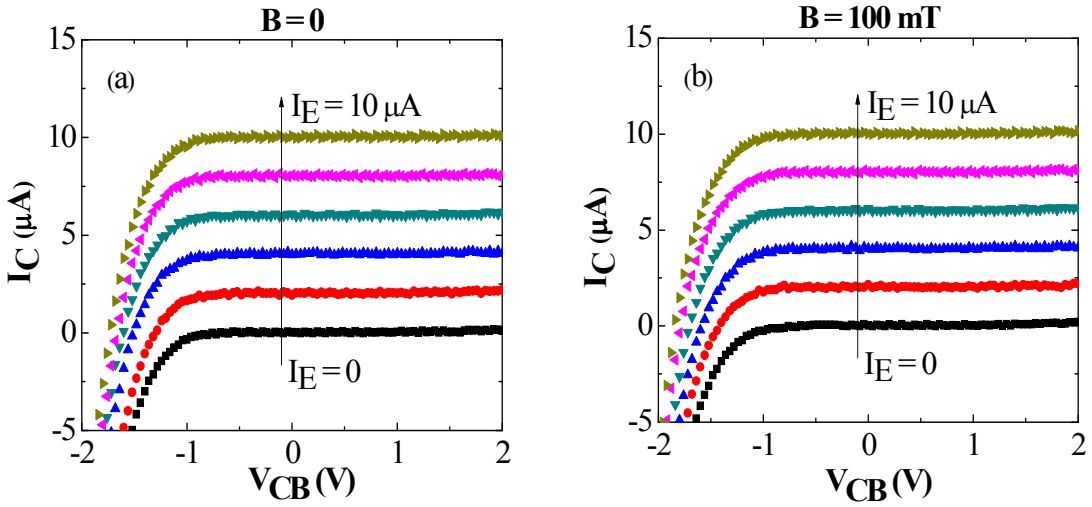


Figure 4.31 Common-base characteristics for n-Si/SPAN(175 nm)/$C_{60}$/$Alq_3$/$V_2O_5$/Al with 1 $mm^2$, measured at room temperature

The offset voltage remains unchanged below -1 V even $I_E$ is changed from 0 to 10 μA. As the magnetic field is varied, the $I_C$ remains virtually unchanged for both cases (Figure 4.31a and b) which lead us to the conclusion that there is no influence of magnetic field in CB characteristics. At $I_E$ = 0, the common-base characteristics can be regarded as the BC diode characteristic. In this case, the BC junction also needs to be forward-biased to compensate the $I_E$. Thus $V_{CB}$ is negative, as shown in Figure 4.31. After $V_{CB}$ is larger than the offset voltage, the $I_C$ increases sharply. Following passing the $V_{knee}$, the $I_C$ is independent of $V_{CB}$. The sharp turn-on behavior and nearly $V_{CB}$-independent $I_C$ in the turn-on region

indicate that our PBT is free of $I_C$ blocking. The $V_{knee}$ increases with an increase in the $I_C$ and it changes from negative to positive value, as shown in Figure 4.31. In the common-base configuration, $V_{CB}$ is directly the bias of the BC junction.

Although we hardly see any differences measurements made with the magnetic field as presented in the previous device, there is certainly a small change on $I_C$ as we scanned the $V_{CB}$ as previously published by Gruber et. al [65] (Figure 4.32). As we can find form Figure 4.32 at a region where $I_C$ and $V_{CB}$ are negative, there is small and slight change. This may be due to the fact that there is some displacement in Fermi level.

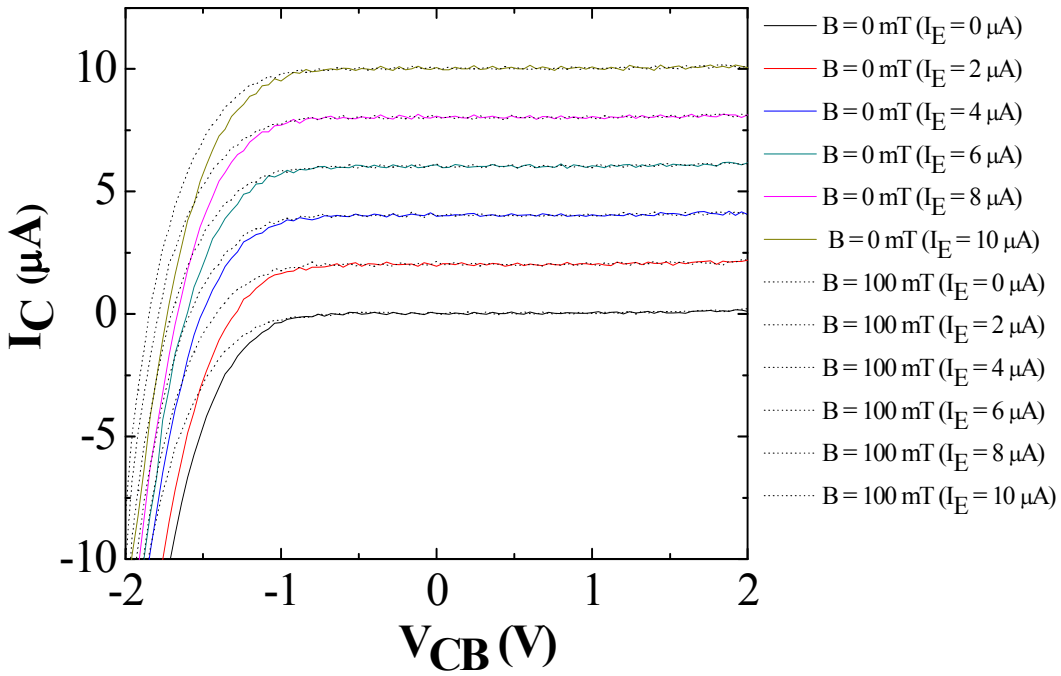


Figure 4.32 The overlapped of common-base characteristics for two different conditions (dotted line) with magnetic field, and (solid line) without magnetic field at different $I_E$

If $I_C$ is plotted against $I_E$ at constant $V_{CB}$ values, as shown in Figure 4.33, straight lines are obtained, which correspond to common-base current gain $\alpha_O = dI_C / dI_E$ of the n-Si/SPAN/$C_{60}$/$Alq_3$/$V_2O_5$/Al devices, calculated to be about 0.996, nearly ideal value of 1.

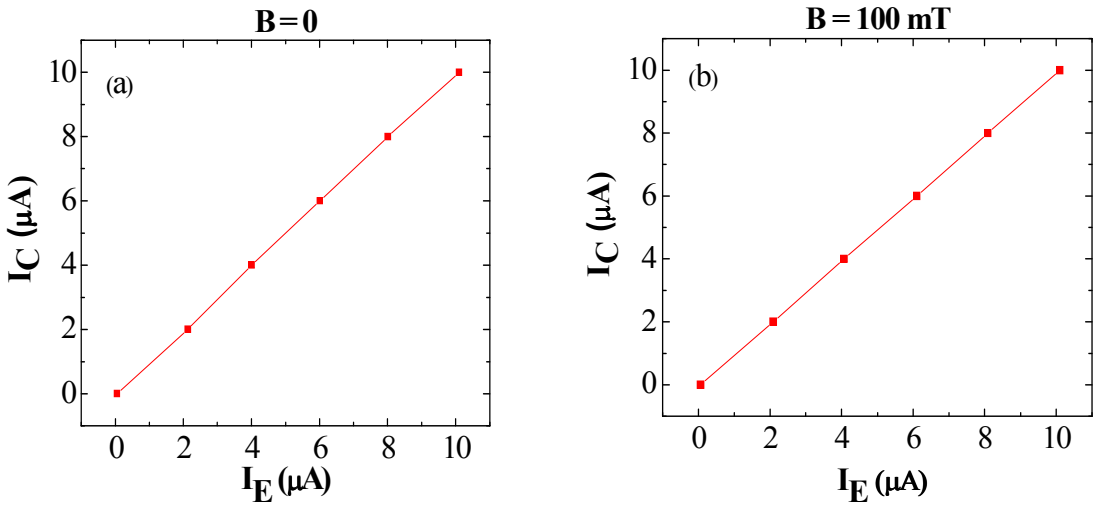


Figure 4.33 Variation of incremental $I_C$ with $I_E$ at a constant $V_{CB}$ values

A linear relation between $I_C$ and $I_E$ is expected, but a slightly larger $I_C / I_E$ is seen at high $I_E$. This is mostly due to the extra $I_L$ contribution as the device heats up with large $I_E$. Another effect that accounts for a larger $I_C$ at high $I_E$ is the non-zero resistance of the base layer. This high $\alpha_O$ indicates that almost all electrons injected by the emitter are able to cross the base, being collected by the collector.

Additionally, there is no significant $I_L$, indicating that the $C_{60}$/$Alq_3$ interface shows negligible minority carrier injection and this also indeed indicates that SPAN can form a better Schottky contact with n-Si, in which favors the suppression of the $I_L$, as expected. Our

transistors operate like PBT since the relationship of $V_{BE}$ as a function of $V_{CB}$ at constant $I_E$ is $\partial V_{BE}/\partial V_{CB} = 1$ [67] (Figure 4.34).

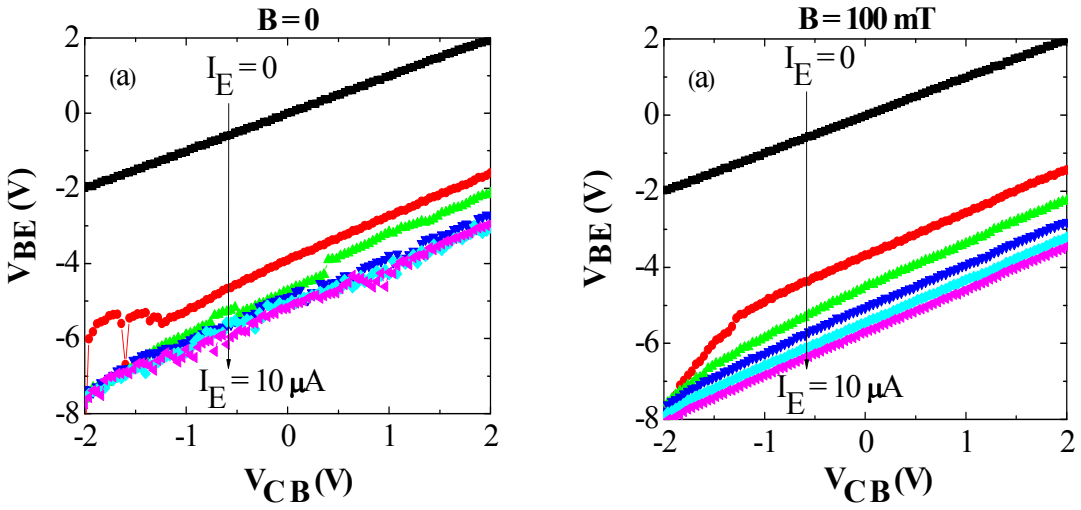


Figure 4.34 Variation of incremental $V_{BE}$ with $V_{CB}$ at different $I_E$ values

This also indicates that the metal base must present pinholes, resulting in the electrical field not being effectively shielded. Figure 4.34 shows the variation of $V_{BE}$ necessary to maintain $I_E$ constant during the $V_{CB}$ scan. As can be seen $\partial V_{BE}/\partial V_{CB} = 1$ at different values of $I_E$, ranging from 0 (top) to – 10 μA (bottom) at steps of -2 μA, indicating that the device operates as PBT. It is widely known that the process of charge transfer between the emitter and collector occurs mainly through small openings in the base layer, rather than by ballistic transport across, it is the principle behind PBT [70]. Hence it is consistent with the existence of pinholes in the SPAN base layer, which is indeed observed in Optical Microscopy, as exemplified in Figure 3.4.

Room temperature I-V curves of common-emitter characteristics of n-Si/SPAN/$C_{60}$/$Alq_3$/$V_2O_5$/Al device are shown in Figure 4.35, allowing the determination of the common-emitter current gain $\beta = \delta I_C / \delta I_B$. An unexpected low $V_{CE}$ offset value around 2 V is observed and this means that small potential barrier exists for charge transfer from emitter to collector (Figure 4.35a). On the other hand, the $I_C$ curve has a considerable sensitiveness to magnetic field, as one can see in Figure 4.35b. One can also find a low offset may be due to a good ohmic characteristic of the n-Si and In-Ga eutectic alloy. As can be seen, device with applied magnetic field has a lower offset voltage and a high $I_C$, 1.8 V and 8 μA, respectively, compared to the device without magnetic field. We attributed this to the lower emitter-base turn-on voltage of the device with magnetic field.

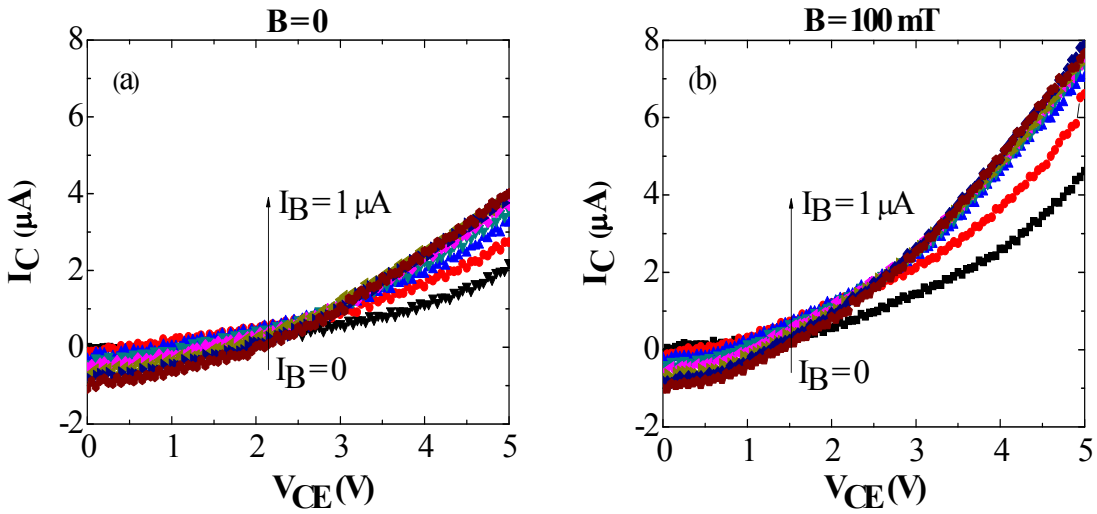


Figure 4.35 Common-emitter characteristics of n-Si/SPAN(175 nm)/$C_{60}$/$Alq_3$/$V_2O_5$/Al measured at different $I_B$ values

The device also shows a tendency towards saturation for voltages less than 2 and 1 V for the case without and with the presence of magnetic field, respectively. With the

increment of $I_B$, the increase in the $I_C$ is observed as shown in Figure 4.35. As $V_{CE}$ is increased; there is a corresponding increment in the $I_C$. This is presumably results from an early effect and leads to non-zero slope. As shown in Figure 4.36a and b, the DC $\beta^*$ of n-Si/SPAN/$C_{60}$/$Alq_3$/$V_2O_5$/Al device, measured at different $I_B$ and constant $V_{CE}$, as the magnetic field rises from 0 to 100 mT. Since both devices have the same structure, we noted that the magnetic field improves the PBT performance, increasing $\beta^*$ by 200 % for $B = 100$ mT, $I_B$ = 0.86 μA and $V_{CE}$ = 5 V (see Figure 4.36b). This high increment is ascribed to the electron injection efficiency during operation due to the introduction of external magnetic field. In this PBT and for a very low $I_C$, the $\beta^*$ is very small due to the generation-recombination in the EB depletion region. As the $I_C$ increases, the relative contribution of the generation-recombination current to the total $I_C$ decreases, thereby leading to an increase in the $\beta^*$. This result also shows SPAN/$C_{60}$/$Alq_3$ interfaces can be used to study MFE effects in organic semiconductor device. The high $\beta^*$ is maintained over a wide $V_{CE}$ range.

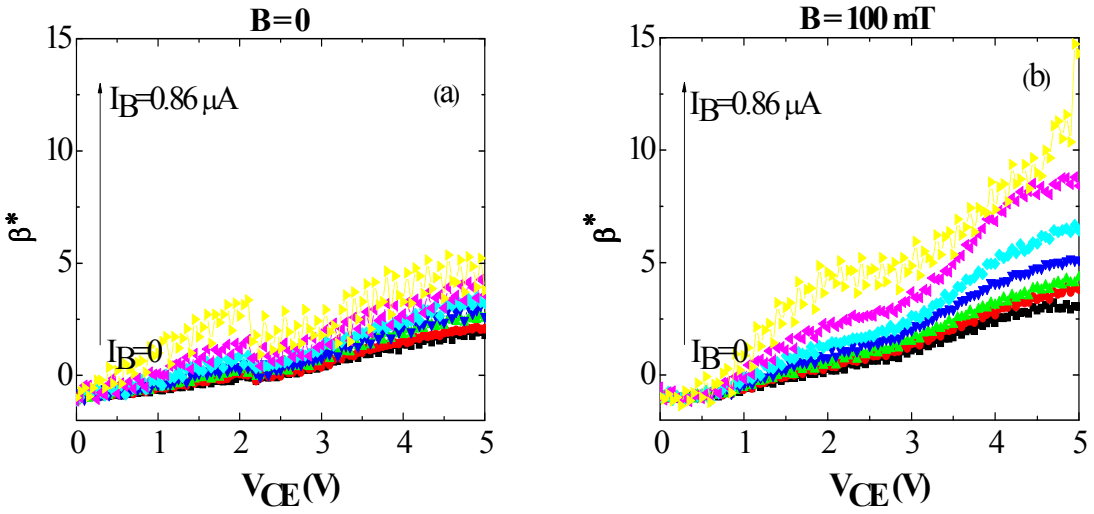


Figure 4.36 Variation of incremental $\beta^*$ with $V_{CE}$ at a different $I_B$ values

## 4.10 SPAN/$C_{60}$/$Alq_3$/$C_{60}$ Heterostructure

### 4.10.1 Device structure (tri emitter layer)

The nature of the interface between base layer and emitter layer in hybrid vertical PBT is of paramount importance for device characteristics, as devices designed for obtaining large MFE values [12]. Here we chose buckminsterfullerene, $C_{60}$, because there are well established and straightforward methods of preparing high quality thin films and also because $C_{60}$ can transport electrons at an appropriate energy level for injection into Si [71]. Using these layers sequence, we avoided the presence of $Alq_3$/SPAN and $Alq_3$/$V_2O_5$ interfaces, strongly favoring electron injection and transport (Figure 4.37).

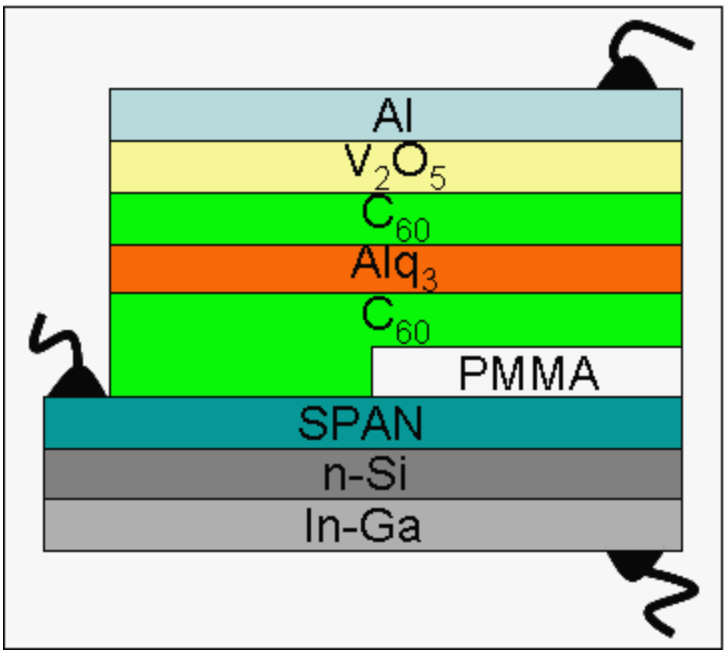


Figure 4.37 Schematic tri-emissive layer design of n-Si/SPAN(200 nm)/$C_{60}$/$Alq_3$/$C_{60}$/$V_2O_5$/Al

## 4.10.2 Energy diagram

Figure 4.38 shows the energy level diagram of the n-Si/SPAN(200 nm)/$C_{60}$(60 nm)/$Alq_3$(60 nm)/$C_{60}$(60 nm)/$V_2O_5$(5 nm)/Al(120 nm).

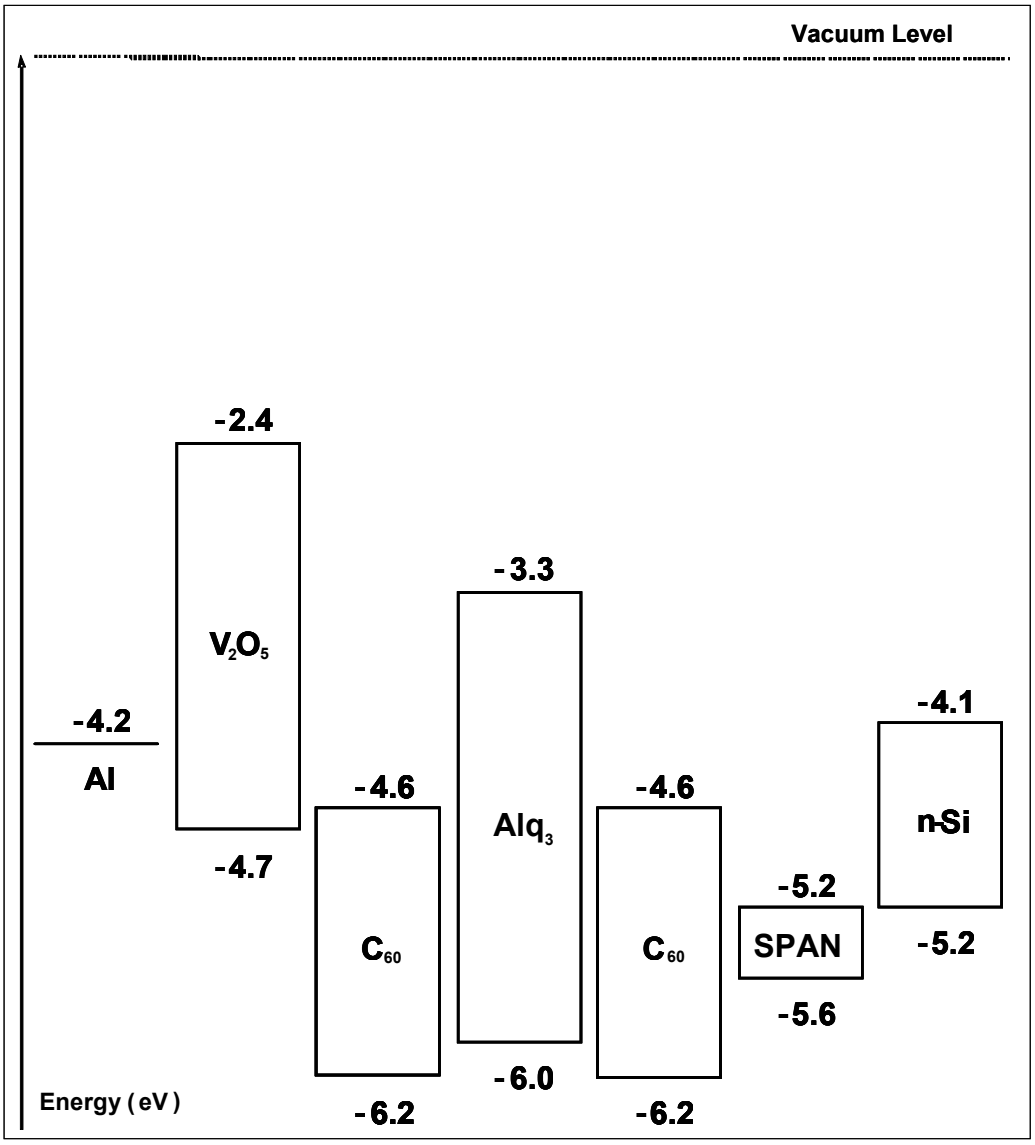


Figure 4.38 Schematic representation of the energy band diagram of n-Si/SPAN(200 nm)/$C_{60}$/$Alq_3$/$C_{60}$/$V_2O_5$/Al device

From this figure, $V_2O_5$ is usually applied for positive charge carrier injection improvement [72-74]. Considering that the HOMO and LUMO are respectively at - 4.7 and - 2.4 eV with respect to vacuum level [75,76], $V_2O_5$ should not contribute to electron injection improvement from Al into emitter layers.

## 4.11 Results and Discussion

### 4.11.1 Two terminal measurements

Diodes characteristics measured on BE and CB diodes are shown in Figure 4.39. The lower current levels in the high positive bias regime suggests a higher series resistance, due to lower hole mobility in the Si collector.

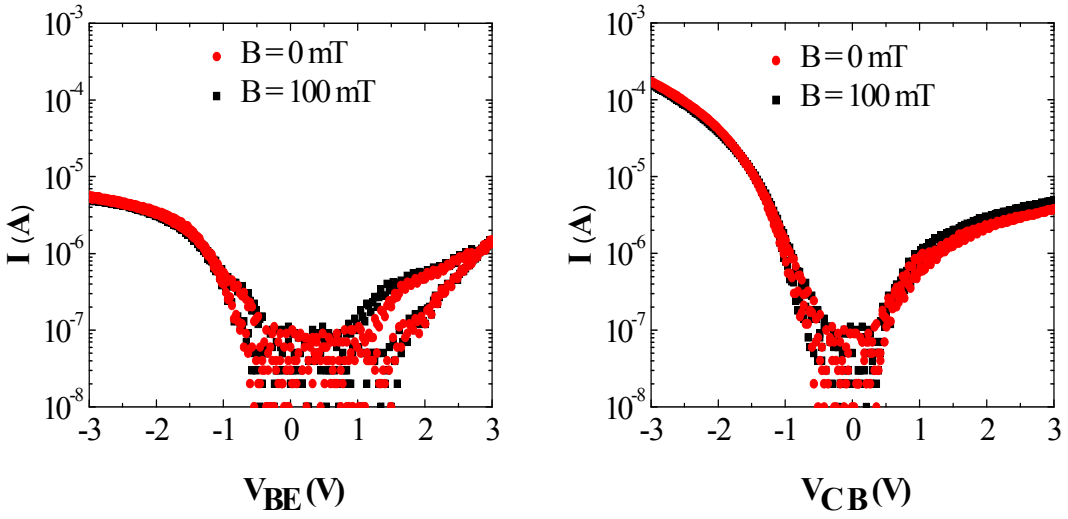


Figure 4.39 Typical I-V characteristics of BE and CB diodes at room temperature

### 4.11.2 Three terminal measurements

Figure 4.40 demonstrate the common-base characteristic of n-Si/SPAN/$C_{60}$/$Alq_3$/$C_{60}$/$V_2O_5$/Al. When $V_{CB}$ is sufficiently negative, a large forward current flow across the base/collector junction and $I_C$ are large and negative. The intercept of the $I_C$ curves in Figure 4.40 with the horizontal axis at negative $V_{CB}$ is due to reverse $V_{CB}$ induced by the $I_E$ drop over the base and due to hot electron current which equals the $I_C$ for negative voltage. For positive $V_{CB}$, $I_C$ is practically constant and almost equal to $I_E$, which implies that $\alpha_0$ is very close to one. This behavior is exactly what would be expected for an ideal transistor that functions by charge injection across a potential barrier [26].

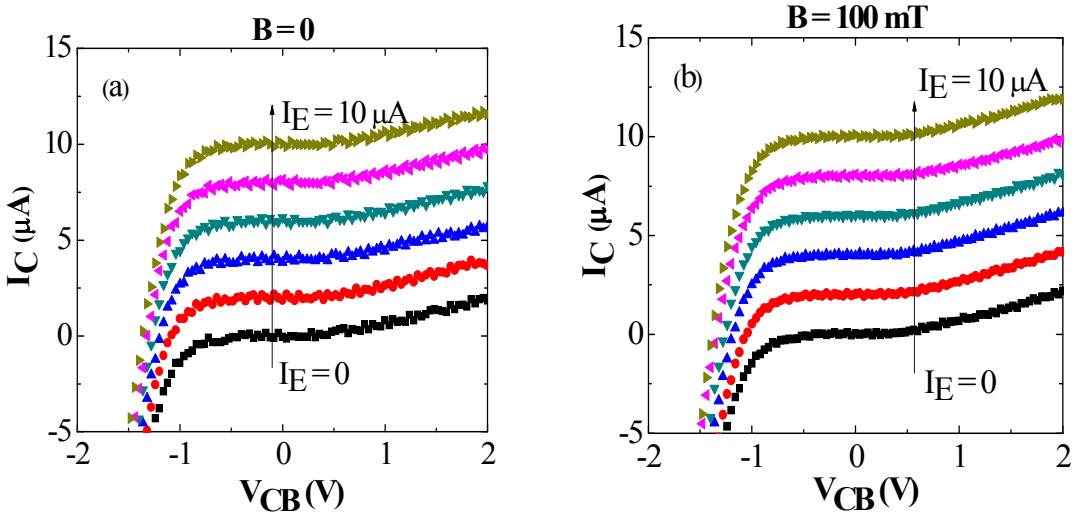


Figure 4.40 Common-base I-V characteristics of n-Si/SPAN(200 nm)/$C_{60}$/$Alq_3$/$C_{60}$/$V_2O_5$/Al. The applied $I_E$ is 0 (bottom trace), 2, 4, 6, 8, 10 μA (top trace)

From Figure 4.40 it can be seen that the $I_L$ contribution is relatively large even in the case with applied external magnetic field. The operating case does not have a profound effect on the device performance. The $I_C$ does not vary linearly with injection current, which

might be attributed to a slightly low barrier height of emitter and collector interface, large area 1 x 1 $mm^2$ and possibly damage to the collector barrier surface (unsaturating $I_L$ usually evidence of this, caused by local high reverse field and thermionic field emission).

There is an interesting effect at negative IC and negative VCB where a small change can be observed from Figure 4.41. This is essentially the forward biased of base/collector junction and this small change is related to the change in Fermi level pinning.

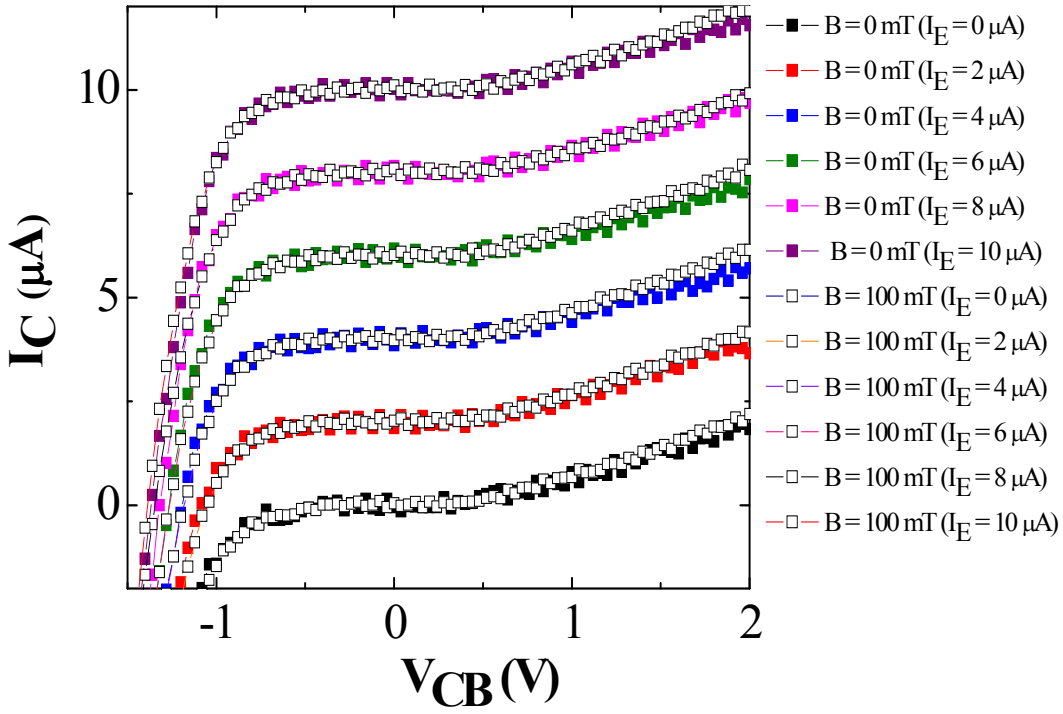


Figure 4.41 The overlapped of common-base characteristics for two different conditions (dotted line) with magnetic field, and (solid line) without magnetic field at different $I_E$

Figure 4.42 is a plot of $I_C$ as a function of $I_E$. The gradient which is equal to $\alpha_O$, is constant and has a value of 0.99 ± 0.02. The measured value of $\alpha_O$ corresponds to a common-base current gain. In both cases, one can see that electron transport from emitter terminal through the opening voids gets into the base terminal. The observed values are in agreement with other device structure value, which equals to unity.

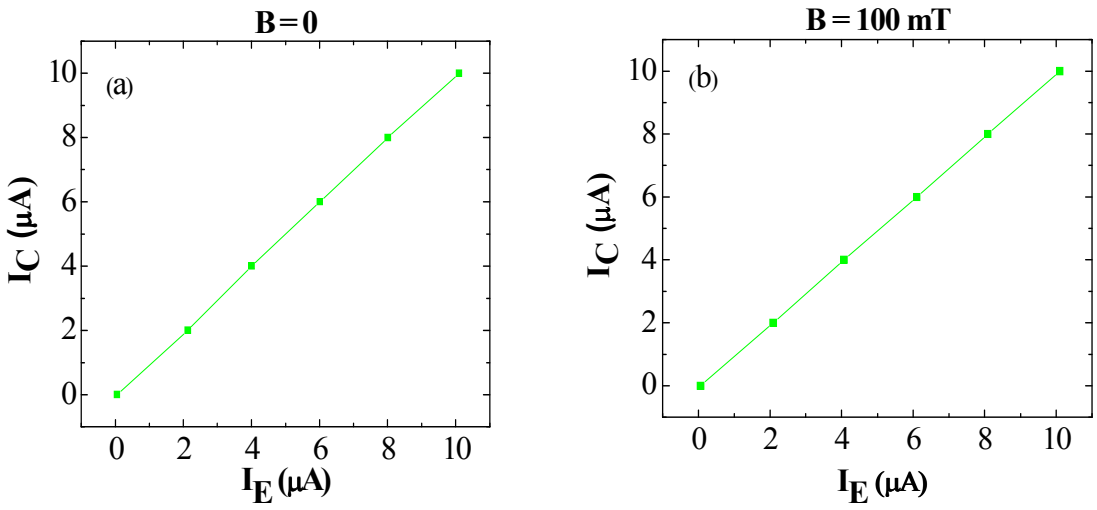


Figure 4.42 $I_C$ as a function of $I_E$ n-Si/SPAN(200 nm)/$C_{60}$/$Alq_3$/$C_{60}$/$V_2O_5$/Al device for $V_{CB}$ = 0

It is important to stress that these currents correspond to high current densities, considering organic semiconductors, being several orders of magnitude larger than in the case of $Alq_3$-base SITs [67].

Another important aspect is that such high currents are achieved at relatively low base-emitter voltage, as can be seen in Figure 4.43, implying low power dissipation inside the

emitter layer. One can see that the voltage required to achieve current level of the order of 1 $\mu A/mm^2$, is lower than 1 V.

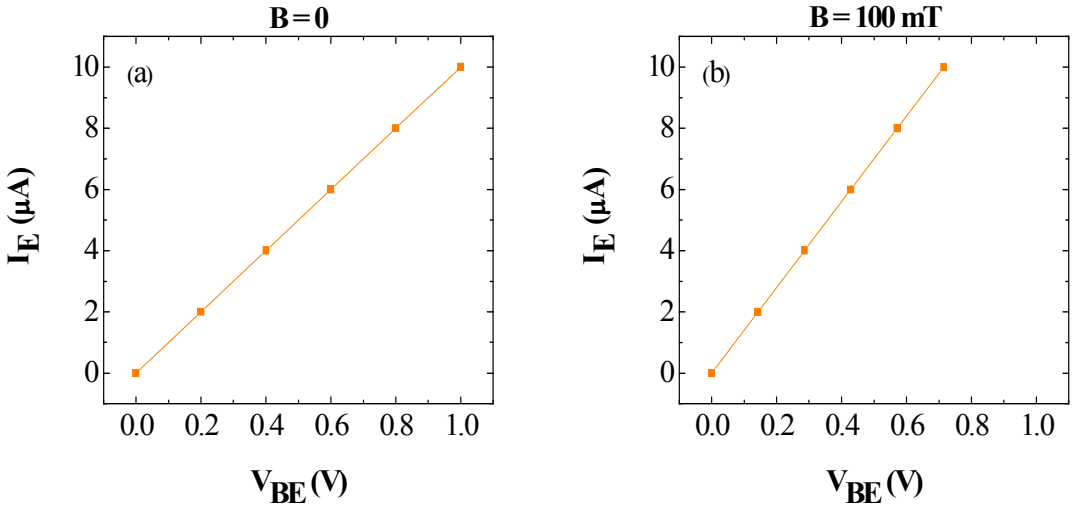


Figure 4.43 Relationship between $I_E$ and $V_{BE}$ at $V_{CB}$ = 0 of n-Si/SPAN(200 nm)/$C_{60}$/$Alq_3$/$C_{60}$/$V_2O_5$/Al device

In Figure 4.44 we present the variation of $V_{BE}$ necessary to maintain $I_E$ constant during the $V_{CB}$ scan. The $\partial V_{BE} / \partial V_{CB} = 1$ indicates that the device indeed operates as PBT, since the base is not able to effectively screen the electrical field [58]. This permeable-base characteristic behavior was observed in all produced devices corresponding to base thickness between 63 to 212 nm.

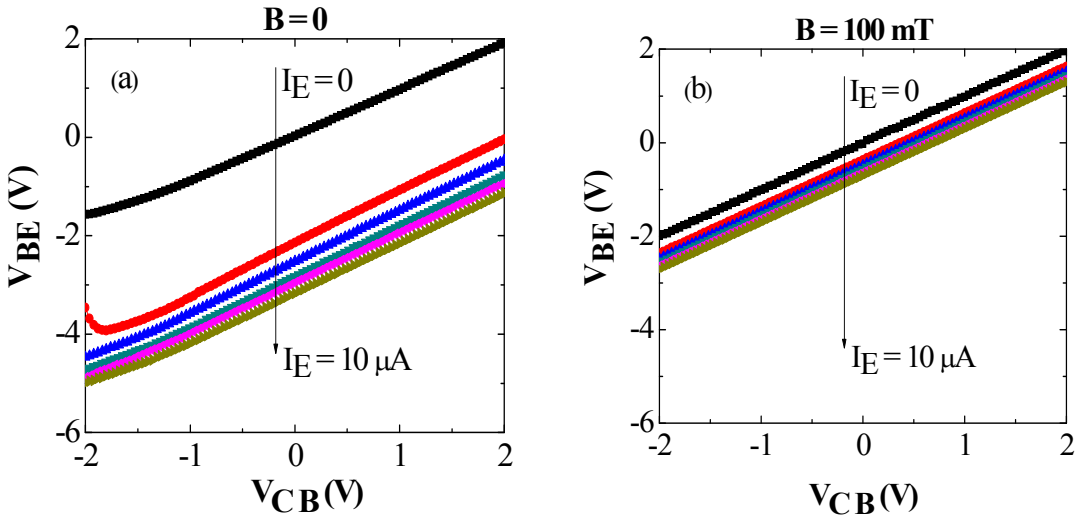


Figure 4.44 Variation of $V_{BE}$ as a function of $V_{CB}$ at a different constant $I_E$ step of 0.14 μA of n-Si/SPAN(200 nm)/$C_{60}$/$Alq_3$/$C_{60}$/$V_2O_5$/Al

The common-emitter characterization of n-Si/SPAN/$C_{60}$/$Alq_3$/$C_{60}$/$V_2O_5$/Al is presented in Figure 4.45. The $I_B$ ranged from 0 to 1 μA in 0.14 μA steps in which an offset voltage is of about 1 V is visible in both figures. The offset voltage is generally caused by a poor base contact resistance and also a high sheet resistance due to the incomplete activation of acceptors in the thin base layer. At low current density, $I_L$ is observed due to soft breakdown in the BC junction. A resistor-like behavior is observed at higher $V_{CE}$, which may be due to a large lateral resistance of the base layer. No saturation is observed in both common-emitter characteristics. One possible reason for this can be considered. It is the early effect, where the $\beta^*$ increased with the $V_{CE}$ due to lower base acceptor concentrations. It is well known that the extrapolated I–V curves meet at the Early voltage ($V_A$) on the voltage axis if the Early effect occurs. In Figure 4.45, however, the extrapolated I–V curves are not likely to meet on the voltage axis and therefore, it seems difficult to explain the lack

of the saturation in I–V characteristics using the early effect. Similar unsaturated I–V characteristics have been reported for other structures except device with SPAN/$Alq_3$ interface.

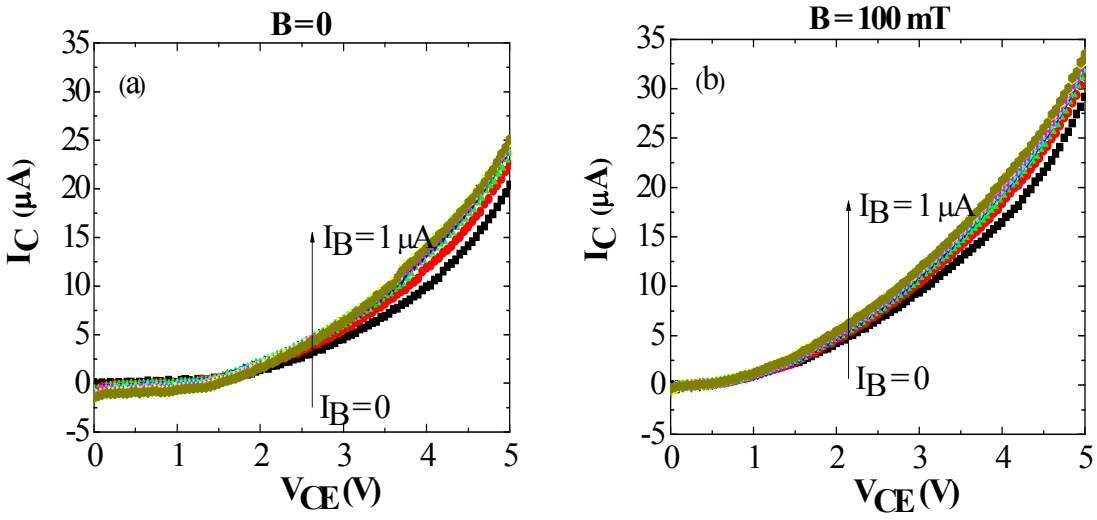


Figure 4.45 Common-emitter output characteristics with $I_B$ step of 0.14 μA of n-Si/SPAN(200 nm)/$C_{60}$/$Alq_3$/$C_{60}$/$V_2O_5$/Al

Likewise, $I_C - V_{CE}$ curves of the magnetic field indicate a change in characteristics in the vicinity of $I_C$ = 0. This region is magnified in Figure 4.46. The device with external magnetic field has a notably lower offset and $V_{knee}$ than device without external magnetic field. The device with external magnetic field (Figure 4.46a) has an offset voltage of $V_{offset}$ = 0.5 V (measured at $V_{CE}$ = 1.5 V and $I_B$ = 0 μA), which is approximately 1 V less than that of the device without external magnetic field, displayed in Figure 4.46a. This reduction promotes the operation of power amplifiers at low $V_{CE}$, increasing efficiency. An interesting feature of magnetic field is the dependence of the $V_{offset}$ on the $I_B$.

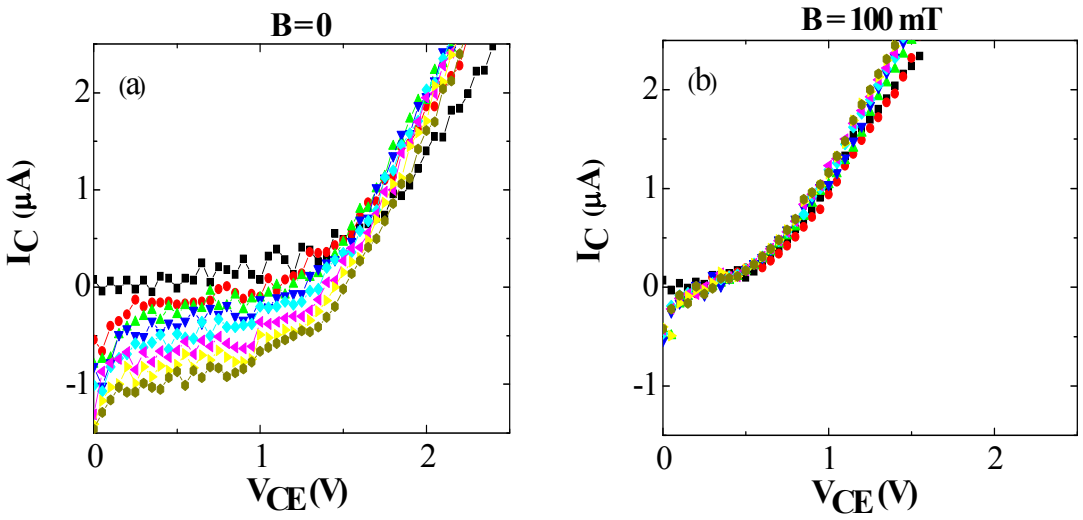


Figure 4.46 Common-emitter output characteristics with $I_B$ step of 0.14 μA of n-Si/SPAN(200 nm)/$C_{60}$/$Alq_3$/$C_{60}$/$V_2O_5$/Al

Since we observed that $\beta^*$ in n-Si/SPAN/$C_{60}$/$Alq_3$/$C_{60}$/$V_2O_5$/Al devices are inconstant, small changes in the $I_B$ result in significant changes in the $I_C$ and correspond to a positive $\beta^*$. The $I_B$ ranged from 0 to 0.86 μA in 0.14 μA steps. As shown in Figure 4.47a, without the presence of an external magnetic field, the value of $\beta^*$ exceeds unity and reaches a value around ~ 10 at $V_{CE}$ = 5 V and $I_B$ = 0.86 μA. Surprisingly, a remarkable increase of the $\beta^*$ could easily be observed of about ~ 23 at $V_{CE}$ = 5 V and $I_B$ = 0.86 μA with the presence of a weak perpendicular magnetic field to the plane of the device. This indicates that the magnetic field has a strong influence in the output current, in which it was larger than the changes in the input current, i. e., current amplification occurred.

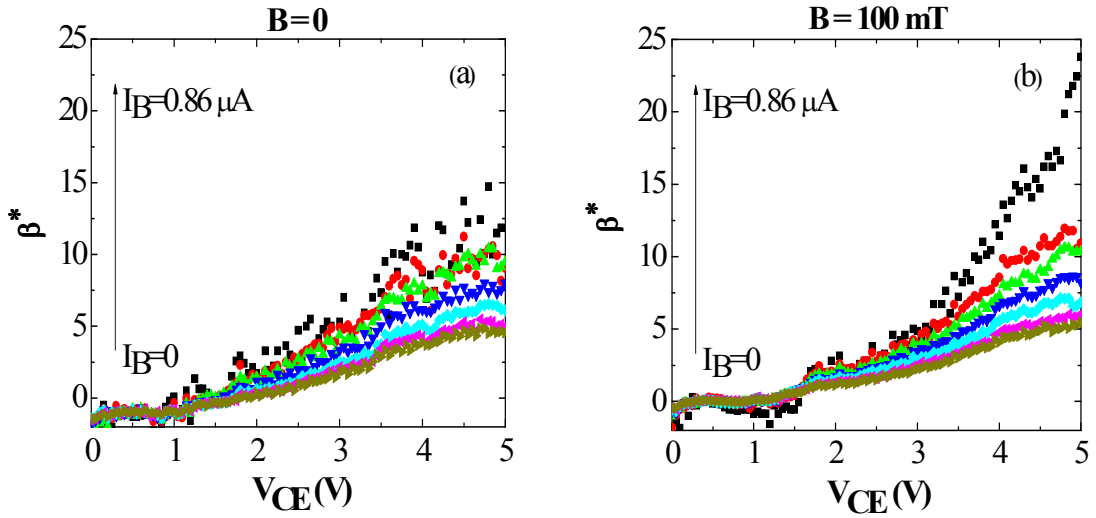


Figure 4.47 Variation of $\beta^*$ against $V_{CE}$ at various constant $I_B$ of n-Si/SPAN(200 nm)/$C_{60}$/$Alq_3$/$C_{60}$/$V_2O_5$/Al

The physics behind the current amplification is not yet understood, but it seems like the electron injected into the base from the emitter can modulate the output current. It is worth to note that the amplification may be caused by removing the carriers from the base. Opening the $I_B$ will allow electrons to flow from emitter to collector. Per 1 electron taken from the base about 100 or so are released to go from emitter to collector. The electrons in the base block the current from emitter to collector electrostatically (they recombine with the holes in the base). Without the $I_B$ there would be no $I_C$. For an ideal current amplification, base transport factor, $\alpha_T$ and emitter efficient, $\gamma_e$, which measures the contribution of injected electrons from the collector and to the emitter, respectively, are equally important. This maximum value of $\beta^*$ is nearly 3 times higher than that of previous SPAN-base hybrid transistor having single $C_{60}$ or $Alq_3$ or layer as emitter [27,28].

In order to clearly understand the relation in the nature of interface the values of $\beta^*$ (with and without magnetic field) as a function of SPAN layer thickness for studied devices at $V_{CE}$ = 5 V and $I_B$ = 0.86 μA are presented in Figure 4.48. It is interesting to observe that considering the magnitude of errors in Figure 4.48, the $\beta^*$ initially increased when the base thickness is increased. In both cases, a rapid increase of $\beta^*$ from 63 until 122 nm SPAN film, reaches a certain maximum value and subsequently decrease with further thickness increasing.

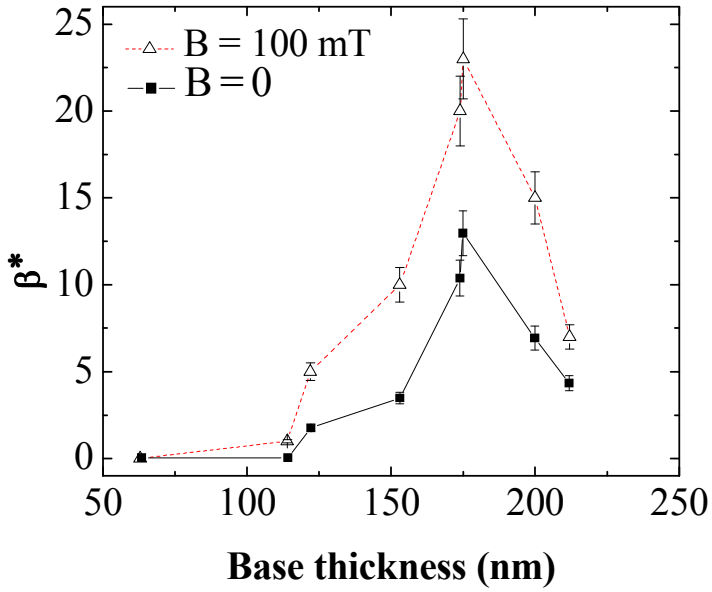


Figure 4.48 Common-emitter current gain for n-Si/SPAN(200 nm)/$C_{60}$ (60 nm)/$Alq_3$(60 nm)/$C_{60}$ (60 nm)/$V_2O_5$ (5 nm)/Al (120 nm) device as a function of base thickness $V_{CE}$ = 5 V and $I_B$ = 1 μA

The mechanism for obtaining high $\beta^*$ is not completely understood and we attributed the maximum of $\beta^*$ to an optimal base thickness, which represents a compromise

between high probability of electron transport from the emitter across the base to the collector and low base in-plane resistance, effectively allowing a uniformity of potential along the base plane. Thinner base implies in higher in-plane resistance and as a consequence, the potential difference between base and emitter depends on the position in the base with respect to metal wire contact due to the base voltage drop, especially at higher $I_B$. However, thicker base reduces the probability of electron transport from emitter to collector, independently of the actual transport mechanism across the base, which can be charge carrier diffusion, tunneling, or drift through pinholes, depending on base thickness and morphology [29]. The $I_C$ for all structures also does not exhibit self-heating. This can be clearly seen from all common-emitter characteristics where $I_C$ is large in the case without magnetic field and even larger with magnetic field, where self-heating in the device will simply reduced the $I_C$. Proof of concept has been established of a 'high' $\beta^*$ (greater than unity), magnetically sensitive, and SPAN-base nonmagnetic organic transistor. (The use of the word 'high' is with respect to other nonmagnetic organic transistors.) This device has a $\beta^*$ slightly greater than unity, which is 3 times larger than any other nonmagnetic organic transistor, although it is still less than the typical bipolar junction transistor $\beta^*$ of 100. However as shown, it is possible for this design to achieve $\beta^*$ comparable to the bipolar junction transistor. In absence of magnetic field and at room temperature, the common-emitter I–V characteristics are similar to those of conventional transistors and afford $\beta^*$ greater than unity and respectable $I_E$. The $\beta^*$ of the device can be magnetically tuned up to 384 % which occurred at 100 mT, $V_{CE}$ = V and $I_B$ = 0.86 μA. Moreover, the $I_B$ and $V_{EC}$ control this field-dependent gain. However, the device described has a number of shortcomings, which, if eliminated, may provide improved performance.

# CHAPTER 5
# Outlook

## Outlook

Summarize of future works:

1-A comprehensive research on true unipolar devices (electron and hole only device).

2-A comprehensive exploration of nonmagnetic organic permeable base transistor in a high frequency, temperature and speed range.

3-A serious study on SPAN preparations in terms of room temperature and controlled temperature.

4-Optimized the nonmagnetic organic permeable base transistor in order to obtain all important key figure of merits (MFE, current gain, on/off current ratio and leakage current).

# CHAPTER 6
# References

## References


[1] R. P. Groff, R. E. Merrifield, A. Suna, P. Avakian, *Physical Review Letters* **29** (1972) 429.

[2] R. P. Groff, A. Suna, P. Avakian, R. E. Merrifield *Physical Review B* **9** (1974) 2655.

[3] V. Ern, R. E. Merrifield, *Physical Review Letters* **21** (1968) 609.

[4] J. Kalinowski, M. Cocchi, D. Virgili, P. di Marco, V. Fattori, *Chemical Physics Letters* **380** (2003) 710.

[5] Ö. Mermer, G. Veeraraghavan, T. Francis, M. Wohlgenannt, *Solid State Communications* **134** (2005) 631.

[6] Ö. Mermer, G. Veeraraghavan, T. Francis, Y. Sheng, T. D. Nguyen, M. Wohlgenannt, A. Köhler, M. K. Al-Suti, M. S. Khan, *Physical Review* B **72** (2005) 205202.

[7] T. A. Skotheim, J. R. Reynolds, *Conjugated Polymers: Theory, Syntheis, Properties and Characterization* (2007)

[8] J. Singh, *Electronic and Optoelectronic Properties of Semiconductor Structures* (2003)

[9] V. Ramamurthy, *Organic Molecular Photochemistry* (1997)

[10] F. So, *Organic Electronics : Materials, Processing, Devices and Applications* (2010)

[11]Z. V. Vardeny, *Organic Spintronics* (2010)

[12] A. R. B. M. Yusoff, W. J. da Silva, J. P. M. Serbena, M. S. Meruvia, I. A. Hümmelgen, *Applied Physics Letters* **94** (2009) 253305.

[13] C. Ciccarelli, B. G. Park, S. Ogawa, A. J. Ferguson, J. Wunderlich, *Applied Physics Letters* **97** (2010) 082106.

[14] T. Reichert, T. P. I. Saragi, *Applied Physics Letters* **98** (2011) 063307.

[15] M. Nishioka, Y.-B. Lee, A. M. Goldman, Y. Xia, C. D. Frisbie, *Applied Physics Letters* **91** (2007) 092117.

[16] S. A. Bagnich, U. Niedermeier, C. Melzer, W. Sarfert, H. von Seggern, *Journal of Applied Physics* **106** (2009) 113702.

[17] S. A. Bagnich, U. Niedermeier, C. Melzer, W. Sarfert, H. von Seggern, *Journal of Applied Physics* **105** (2009) 123706.

[18] I. Bergenti, V. Dediu, E. Arisi, T. Mertelj, M. Murgia, A. Riminucci, G. Ruani, M. Solzi, C. Taliani, *Organic Electronics* **5** (2004) 309.

[19] A. H. Davis, K. J. Bussmann, *Journal Vacuum Science and Technology A* **22** (2004) 1885.

[20] P. Desai, P. Shakya, T. Kreouzis, W. P. Gillin, *Physical Review* B **76** (2007) 235202.

[21] P. Desai, P. Shakya, T. Kreouzis, W. P. Gillin, *Journal of Applied Physics* **102** (2007) 073710.

[22] P. Desai, P. Shakya, T. Kreouzis, W. P. Gillin, N. A. Morley, M. R. J. Gibbs, *Physical Review* B **75** (2007) 094423.

[23] R. Liu, Y. Zhang, Y. L. Lei, P. Chen, Z. H. Xiong, *Journal of Applied Physics* **105** (2009) 093719.

[24] T. D. Nguyen, J. Rybicki, Y. Sheng, M. Wohlgenannt, *Physical Review* B **77** (2008) 035210.

[25] T. Nguyen, Y. Sheng, J. Rybicki, G. Veeraraghavan, M. Wohlgenannt, *Synthetic Metals* **160** (2010) 320.

[26] H. Odaka, Y. Okimoto, T. Yamada, H. Okamoto, M. Kawasaki, Y. Tokura, *Applied Physics Letters* **88** (2006) 123501.

[27] N. Rolfe, P. Desai, P. Shakya, T. Kreouzis, W. P. Gillin, *Journal of Applied Physics* **104** (2008) 083703.

[28] G. Salis, S. F. Alvarado, M. Tschudy, T. Brunschwiler, R. Allenspach, *Physical Review* B **70** (2004) 085203.

[29] P. Shakya, P. Desai, T. Kreouzis, W. P. Gillin, *Journal of Applied Physics* **103** (2008) 043706.

[30] P. Shakya, P. Desai, M. Somerton, G. Gannaway, T. Kreouzis, W. P. Gillin, *Journal of Applied Physics* **103** (2008) 103715.

[31] G. Veeraraghavan, T. D. Nguyen, Y. Sheng, Ö. Mermer, M. Wohlgenannt, *IEEE Transactions Electron Devices* **54** (2007) 1571.

[32] L. Xin, C. Li, F. Li, S. Liu, B. Hu, *Applied Physics Letters* **95** (2009) 123306.

[33] J. Behrends, A. Schnegg, K. Lips, E. A. Thomsen, A. K. Pandey, I. D. W. Samuel, D. J. Keeble, *Physical Review Letters* **105** (2010) 176601.

[34] G. J. Ritchie, *Transistor Circuit Techniques: Discrete and Integrated* (1993)

[35] E. Cantatore, *Proceeding of the SAFE/IEEE Workshop* **27** (2000) 27.

[36] F. Garnier, *Philosophical Transactions* **355** (1997) 815.

[37] C. D. Dimitrakopoulos, D. J. Mascaro, *IBM Journal of Research and Development* **45** (2001) 11.

[38] L. L. Chua, J. Zaumseil, J. F. Chang, E. C. W. Ou, P. K. H. Ho, H. Sirringhaus, R. H. Friend, *Nature* **434** (2005) 194.

[39] C. K. Chiang, C. R. Fincher, Jr., Y. W. Park, A. J. Heeger, H. Shirakawa, E. J. Louis, S. C. Gau, A. G. MacDiarmid, *Physical Review Letters* **39** (1977) 1098.

[40] H. Sirringhaus, *Advanced Materials* **17** (2005) 2411.

[41] G. J. Ritchie, Transistor Circuit Techniques Discrete and Integrated, Chapman & Hall/CRC (1993)

[42] Lecture notes from Department of Physics, Georgia Institute of Technology

[43] P. A. Bobbert, T. D. Nguyen, F. W. A. van Oost, B. Koopmans, M. Wohlgenannt, *Physical Review Letters* **99** (2007) 216801.

[44] V. N. Prigodin, J. D. Bergeson, D. M. Lincoln, A. J. Epstein, *Synthetic Metals* **156** (2006) 757.

## References


[45] (a) P. Desai, P. Shakya, T. Kreouzis, W. P. Gillin, *Journal of Applied Physics* **102** (2007) 073710. (b) X. –F. Dong, X. –X. Li, S. –J. Xie, *Organic Electronics* **12** (2011) 1835.

[46] D. Hertel, K. Meerholz, *Journal of Physical Chemistry B* **111** (2007) 12075.

[47] V. Ern, R. E. Merrifield, *Physical Review Letters* **21** (1968) 609.

[48] B. Hu, Y. Wu, *Nature Materials* **6** (2007) 985.

[49] B. Hu, L. Yan, M. Shao, *Advanced Materials* **21** (2009) 1500.

[50] D. J. Gundlach, T. N. Jackson, D. G. Schlom, S. F. Nelson, *Applied Physics Letters* **74** (1999) 3302.

[51] C. –H. Yang, L. –R. Huang, Y. –K. Chih, W. –C. Lin, F. –J. Liu, T. –L. Wang, *Polymer* **48** (2007) 3237.

[52] (a) M. Wan, Synth. Met., 1989, 31, 51–59; (b) K. Kanamura, Y. Kawai, S. Yonezawa, Z.-I. Takeharhys, *Journal of Materials Chemistry* **98** (1994) 2174.

[53] C. P. L. Rubinger, C. R. Martins, M. A. de Paoli, R. M. Rubinger, *Sensors Actuators B* **123** (2007) 42.

[54] K. G. Neoh, M. Y. Pun, E.T. Kang, K.L. Tan, *Synthetic Metals* **73** (1995) 209.

[55] M. R. Karim, K. T. Lim, C. J. Lee, M. T. I. Bhuiyan, H. J. Kim, L. -S. Park, M. S. Lee, *Journal of Polymer Science Polymer Chemistry* **45** (2007) 5741.

[56] A. B. Afzal, M. J. Akhtar, M. Nadeem, M. Ahmad, M. M. Hassan, T. Yasin, M. Mehmood, *Journal of Physics D: Applied Physics* **42** (2009) 015411.

[57] A. Akelah, N. El-Deen, A. Hiltner, E. Baer, A. Moet, *Materials Letters* **22** (1995) 97.

[58] G. Niaura, R. Mažeikiene, A. Malinauskas, *Synthetic Metals* **145** (2004) 105.

[59] C. Barbero, M. C. Miras, R. Kotz, O. Haas, unpublished work.

[60] J. Huang, S. Virji, B. H. Weiller, R. B. Kaner, *Journal American Chemical Society* **125** (2003) 314.

## References


[61] D. E. Stilwell, S-M. Park, *Journal of Electrochemical Society,* **135** (1988) 2491.

[62] R. Mazeikiene, V. Tomkute, Z. Kuodis, G. Niaura, A. Malinauskas, *Vibrational Spectroscopy* **44** (2007) 201.

[63] C. Barbero, M. C. Miras, B. Schnyder, O. Haas, R. Kotz, *Journal of Materials Chemistry* **4** (1994) 1775.

[64] M. Yi, J. Huang, D. Ma, I. A. Hümmelgen, *Applied Physics Letters* **92** (2008) 243312.

[65] (a) A. R. B. M. Yusoff, I. A. Hümmelgen, *Journal of Applied Physics* **106** (2009) 074505, (b) M. S. Meruvia, A. R.V. Benvenho, I. A. Hümmelgen, R. W.C. Li, L. H. J.M.C. Aguiar, J. Gruber, *Solid State Communications* 139 (2006) 27

[66] W. J. Da Silva, I. A. Hümmelgen, R. M. Q. Mello, *Journal of Material Science:Material Electronics* **20** (2009) 123.

[67] M. S. Meruvia, I. A. Hümmelgen, *Advanced Functional Materials* **16** (2006) 459.

[68] W. J. Da. Silva, I. A. Hümmelgen, R. M. Q. Mello, *Applied Physics Letters* **93** (2008) 053301.

[69] C. O. Bozler, G. D. Alley, *IEEE Transactions on Electron Devices* **27** (1980) 1129.

[70] R. T. Tung, A. F. J. Levi, J. M. Gibson, *Applied Physics Letters* **48** (1986) 635.

[71] S. Zorba, Y. Gao, *Applied Physics Letters* **86** (2005) 193508.

[72] J. P. M. Serbena, I. A. Hümmelgen, T. Hadizad, Z. Y. Wang, *Small* **2** (2006) 372.

[73] M. S. Meruvia, I. A. Hümmelgen, M. L. Sartorelli, A. A. Pasa, W. Schwarzacher, *Applied Physics Letters* **84** (2004) 3978.

[74] X. L. Zhu, J. X. Sun, H. J. Peng, Z. G. Meng, M. Wong, H. S. Kwok, *Applied Physics Letters* **87** (2005) 153508.

[75] C. W. Chu, S. H. Li, C. W. Chen, S. Shrotriya, Y. Yang, *Applied Physics Letters* **87** (2005) 193508.

## References

[76] T. -H. Chen, Y. Liou, T. J. Wu, J. Y. Chen, *Applied Physics Letters* **87** (2005) 243510.

[77] V. Shrotriya, G. Li, Y. Yao, C. -W. Chu, Y. Yang, *Applied Physics Letters* **88** (2006) 073508.

[78] N. N. Greenwood, A. Earnshaw, *Chemistry of the Elements, Pergamon,* (1990)

[79] M. Dongge, I. A. Hümmelgen, B. Hu, F. E. Karasz, *Journal of Applied Physics* **86**, (1991) 3181.

[80] K. C. Kao, W. Hwang, *Electrical Transport in Solids, Pergamon*, (1981).

[81] M. S. Meruvia, J. A. Freire, I. A. Hümmelgen, J. Gruber, C. F. O. Graeff, *Organic Electronics* **8**, (2007) 695.

# CHAPTER 7
# Appendix

## Unipolar Devices

The main objective of unipolar devices is to investigate if electrons and holes are needed for MFE. We divided this work into 2 different structures, namely:

i) Electron-only device

ii) Hole-only device

For unipolar devices (Figure A1), we eliminate the SPAN base terminal and In-Ga eutectic alloy of the hybrid vertical architecture transistor. The Al and Au thin film are deposited at the back of the n-Si and p-Si, respectively using high vacuum deposition with the system base pressure $10^{-6}$ Torr. The $Alq_3$ layer is unpatterned, covering the entire substrate. The top electrodes are defined by shadow masks having single or multiple parallel slits. Various slit widths are used, resulting in device areas ranging from 1 to 3 $mm^2$. On each substrate, a set of up to five nominally identical devices are made. In both cases all electrodes have a thickness of 60 nm.

## Device Structures

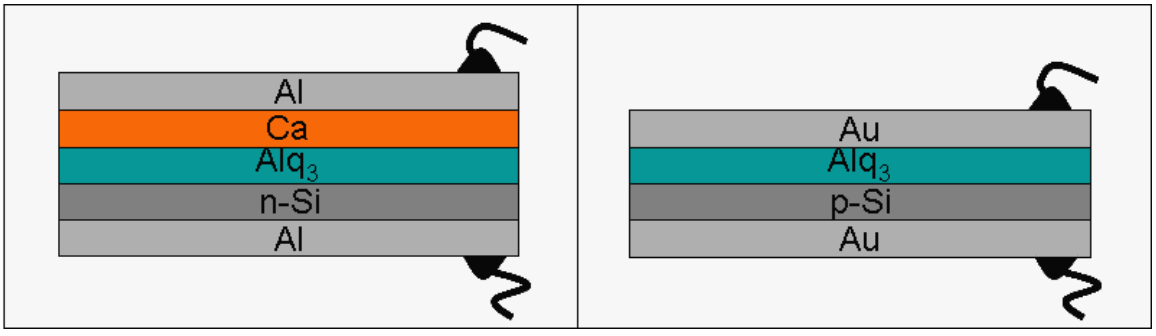


Figure A1 Schematic structures for unipolar devices (left panel) electron-only structure (right panel) hole-only structure

**Energy Diagrams**

Energy levels for both electron and hole-only devices are presented in Figure A2. The electron energy values in the top are measured with respect to vacuum level. These are in case of metals, Fermi levels, in case of $Alq_3$, HOMO and LUMO levels and n-Si valence and conduction band, with the dashed line indicating the position of the Fermi level in Si. We used completely different structure to study hole and electron in $Alq_3$ domains employing n-Si and p-Si. For hole only device, where Au is biased positively with respect to Au/$Alq_3$, the device permits only hole transport via the highest occupied molecular orbital; (HOMO) of $Alq_3$ because hole injection from Au to $Alq_3$ occurs nominally to small energy barrier. In our device with Al bottom contacts (electron only), electron can be injected from Ca into the $Alq_3$ LUMO.

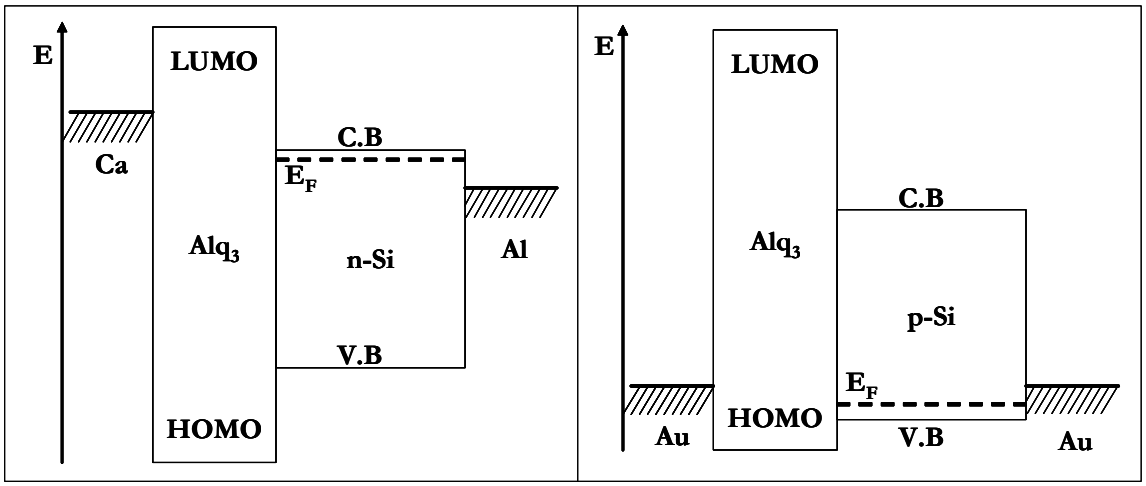


Figure A2 Energy diagram of (left panel) electron-only device (right panel) hole-only device [12]

### Two Terminal Measurements

For I-V characteristics, 3 measurements were sequentially made; (i) without external magnetic field; (ii) with external magnetic field and (iii) without external magnetic field. Figure A3 displays the I–V characteristics of the electron-only and hole-only devices. In these devices, the I–V characteristics consist of contributions from electron or hole since materials are selected to allow only majority charge carrier injection when the metal electrode, Al/Ca or Au, deposited onto the $Alq_3$ is negatively biased with respect to n-Si/Al or positively biased with respect to p-Si/Au, respectively. There is no MFE in these devices and it can be seen that these three curves overlap each other, without any clear distinction of the curve measured at the $B$ = 100 mT condition. It is worth to mention that in rare cases of single-carrier devices, a small variation in current has occurred.

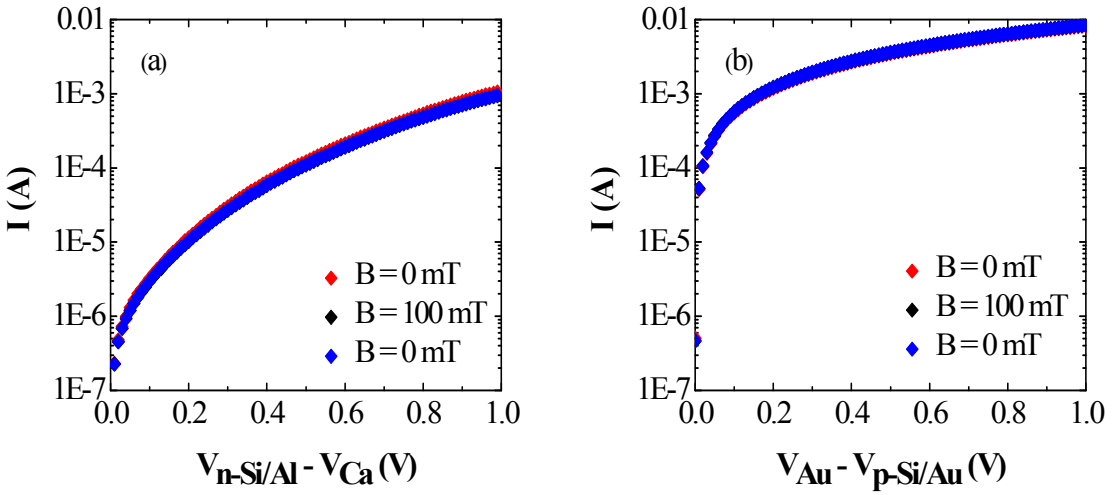


Figure A3 Current-voltage characteristics of (a) electron-only device (b) hole-only device [12]

In our opinion, this is very strong evidence that the degradation process starts or it could be the electric stress effects. We also made experiments measuring current at constant

voltage, alternating absence and presence of $B$ = 100 mT using the permanent magnet and could not find clear evidence of MFE.

These observations lead to the conclusion that magnetic field has a strong influence on electrons. This can be evidenced by the current increment in common-emitter characteristics (Figure 4.14). These two main observations namely i) no MFE in single carrier devices (true-hole only and true-electron only devices) and ii) high increment in current may be seen as contradictory, but yet the high increment in the electron current with the presence of magnetic field can be seen as sign that the external magnetic field induces a rapid enhance in charge mobility of electron. The finding in high increment in electron current does not allow us to assign to a specific fundamental mechanism, but these results are essentially clear evidence that the magnetic field has a strong influence on electrons resulting the increment in the electron current. The current increment by some orders of magnitude in organic devices imposed by changes in the effective charge carrier mobility due to variations in trap occupation fraction, which is equivalent to an effective change in the concentration of actively transport affecting traps, is not uncommon [79,80]. And indications that the magnetic field affects trap occupation were already found in conjugated polymer based devices [81].

By simply following this argumentation, we attributed the observation of MFE in bipolar injection device may be due to the necessary formation of electron-hole pairs, as explained by several proposed models [47] and the location of the quasi-Fermi level inside the $Alq_3$ (during device operation) in which it will essentially influence the occupation fraction of defects and it depends on the work function of both electrodes.

On the other hand, in the true-hole only and true-electron only devices, the Poole-Frenkel enhancement of charge carrier emission from traps are relevant [81]. This is because the electric field strength tends to zero near the majority carriers injection electrode and achieves very high values near the minority carriers injecting electrode [80]. This mechanism may act also assisting pair dissociation.

## Appendix – Schottky Barrier Height Determination

There are basically four different techniques to determine the Schottky Barrier height; namely current-voltage, capacitance-voltage, activation energy, and photoelectric. In this thesis, we have used current-voltage technique. For current-voltage technique, we used

$$J_{S\to M} = A^{*}T^{2}\exp\left[\frac{(qV - q\phi_B)}{kT}\right]$$

where $A^{*} = \frac{4\pi q m^{*} k^{2}}{h^{3}}$, $A = 120\ A/cm^{2}/K^{2}$

$$\ln J = \ln\left(A^{*}T^{2}\right) - \frac{q\phi_B}{kT} + \frac{qV}{kT}$$

$$\phi_B = kT\left[\ln\left(A^{*}T^{2}\right) - \ln J_O\right]$$